UASLP
Universidad Autónoma de San Luis Potosí

FACULTAD DE INGENIERÍA

CENTRO DE INVESTIGACIÓN Y ESTUDIOS DE POSGRADO

UNIVERSIDAD AUTÓNOMA DE SAN LUIS POTOSÍ

CENTRO DE INVESTIGACIÓN Y ESTUDIOS DE POSGRADO (CIEP)

COMPUTATIONAL MODEL FOR FATIGUE CRACK GROWTH IN MECHANICAL COMPONENTS

MODELO COMPUTACIONAL PARA EL CRECIMIENTO DE GRIETAS POR FATIGA EN COMPONENTES MECÁNICOS

Que para obtener el grado de Maestría en Ingeniería Mecánica con Orientación Terminal en Mecatrónica y Sistemas Mecánicos

Presenta:
Ing. Adrián Hernández Zapata

Asesor:
Dr. Christian Jesús García López

San Luis Potosí, S.L.P., enero 2019

UASLP
Universidad Autónoma de San Luis Potosí

FACULTAD DE INGENIERÍA

18 de julio de 2019

ING. ADRIÁN HERNÁNDEZ ZAPATA
P R E S E N T E.

En atención a su solicitud de Temario, presentada por el **Dr. Christian Jesús García López**, Asesor de la Tesis que desarrollará Usted, con el objeto de obtener el Grado de **Maestro en Ingeniería Mecánica con Orientación Terminal en Mecatrónica y Sistemas Mecánicos**, me es grato comunicarle que en la Sesión del H. Consejo Técnico Consultivo celebrada el día 18 de julio del presente, fue aprobado el Temario propuesto:

TEMARIO:

"Modelo computacional para el crecimiento de grietas por fatiga en componentes mecánicos"

Introducción
1. Antecedentes y estudio de la literatura.
2. Modelos computacionales de crecimiento de grieta por fatiga.
3. Simulación de elemento finito para expansión de orificio en frío.
4. Resultados y discusión.

Conclusiones.
Referencias.

"MODOS ET CUNCTARUM RERUM MENSURAS AUDEBO"

A T E N T A M E N T E

M. I. JORGE ALBERTO PÉREZ GONZÁLEZ
DIRECTOR.

Copia. Archivo.
*etn.

www.uaslp.mx

Av Manuel Nava 8
Zona Universitaria • CP 78290
San Luis Potosí, SLP
tel (444) 826 2330 al39
fax (444) 826 2336

AKNOWLEDGMENTS

I acknowledge to the institutions, to the UASLP, and specially to the CIEP and all its people that works hard every day to provide high quality education. I acknowledge to the UASLP for giving me the opportunity to study a master's degree and for the support during my postgraduate studies. Also, I acknowledge to the Consejo Nacional de Ciencia y Tecnología (CONCYT) for the economic support during my studies.

To my thesis advisor, Dr. Christian Jesús García López, for being very supportive during my postgraduate studies, always accurately guiding and motivating me plus demonstrating high compromise with my research work.

To my evaluation committee, Dr. Dirk Frederik de Lange, Dr. Gilberto Mejía Rodríguez, Dr. Francisco Oviedo Tolentino, as well as the rest of the members of the academic committee of the CIEP for always providing guidance and constructive feedback during my research work. Also, I acknowledge to Dr. Ricardo Rafael Ambriz Rojas from the Instituto Politécnico Nacional (IPN), for the provided support.

I acknowledge to all my family, without them this success would not have been possible. I specially acknowledge to my parents who have always supported me in every way I have taken. Also, I thank to my friends and colleagues who were present during my postgraduate studies and provided a lot of support in such a way that the academic experience was complemented with an amazing personal experience.

ABSTRACT

The aim of the present work is to develop a fracture mechanics computational model for the prediction and evaluation of the fatigue crack growth in mechanical drilled components. The fracture mechanics approach is a damage tolerance design philosophy and is focused on the growing cracks on the components by quantifying the critical combination of the flaw size, fracture toughness, geometry and the applied stress by either an energy or a stress intensity tactic.

The studied component, defined from here on as the center-hole-plate model, was an aluminum alloy 6061-T6 plate with a drilled circular hole of a 3.175 mm radius at its midpoint. A cold hole expansion simulation was performed on the drilled hole to induce compressive residual stress near the hole. The cold hole expansion simulated the direct mandrel expansion process, passing an oversized rigid expander with a 3.305 mm radius through the center-hole-plate model. The numerical simulation has been performed through the finite element analysis. The crack propagation has been generated by the opening mode I condition. Through thickness symmetric cracks are assumed to be radially emanating from the hole.

Several finite element models were necessary to implement the following research conditions: the linear-elastic material behavior, cyclic loading, elastic-plastic material behavior and residual stress condition within the base center-hole-plate computational model. Systematically, the first model developed were a base model for which the cold hole expansion was not applied, and it was analyzed only the with linear elastic material behavior, and a static load case. The central-hole-plate base model were validated by two closed-form solutions reported on the literature. Besides the central-hole-plate model, also a linear-elastic model for a compact tension specimen (CT-Specimen-model) were developed and validated against experimental results reported on the literature.

Once the linear-elastic base model for the center-hole-plate specimen was validated, the following computational models were developed as follows: First, a center-hole-plate computational mode for the elastic-plastic material behavior implementation and static load case. Second, the cyclic loading case was simulated within the elastic-plastic center-hole-plate model and finally, the cold hole expansion process (Residual stress condition) was implemented to the elastic-plastic center-hole-plate model. The center-hole-plate model with elastic-plastic material behavior and the residual stress condition was defined as the parametrized center-hole-plate model.

The simulation of the cold hole expansion process generated a non-uniform 3D residual stress field near the hole of the center-hole-plate model. The non-uniform 3D residual stress field was captured through a three-level sub modelling technique. The sub modelling technique is the simplification of a problem by dividing such problem into simple localized models, while optimizing the implementation and solution time. The predicted 3D residual stress field was considered as an initial

condition for fatigue crack growth finite element simulations. In general, tensile residual stress harm the mechanical components accelerating the fatigue crack growth while compressive residual stress delays the crack initiation and propagation.

A comparative of the estimated residual stress field on the three-level sub modelling technique is reported, moreover, the impact of the residual stress predicted by the three-level sub modelling technique within fatigue simulations has been studied.

A study between different methodologies, such as the contour integral, displacement and stress correlation methods, were conducted to define the optimal method to compute the stress intensity factor K within the fatigue simulations, besides, the Paris-Erdogan empirical relation were used to compute the fatigue crack growth rates da/dN. Finally, the da/dN-values estimated by the computational model for fatigue crack growth in mechanical components were validated against an experimental study reported on the literature.

The fatigue da/dN-values predicted by the computational model for fatigue crack growth in mechanical components exhibited the same general trend than the experimental data, however, slight differences were found. The differences between the numerical and experimental results are mainly attributed to the complex, non-uniform 3D nature of the residual stress field generated by the cold hole expansion plus the local variations on the material near the hole.

All the simulations were performed on the finite element software ABAQUS® 2018 in the Center of Investigation and Postgraduate Studies (CIEP) of the Autonomous University of San Luis Potosi.

RESUMEN

La intención del presente trabajo es desarrollar un modelo computacional de mecánica de la fractura para la predicción y evaluación del crecimiento de grieta por fatiga en componentes mecánicos barrenados. El enfoque de la mecánica de la fractura es una filosofía de diseño en base a la tolerancia al daño y está enfocado en la propagación de grietas en componentes mediante la cuantificación de la combinación crítica del tamaño de la grieta, la tenacidad a la fractura, la geometría y el esfuerzo aplicado, ya sea mediante una táctica de energía o bien mediante una táctica de intensidad de esfuerzos.

El componente estudiado, definido de aquí en adelante como el modelo de placa con orificio al centro, fue una placa de aleación de aluminio 6061-T6 con un orificio circular de radio igual a 3.175 mm hecho en el centro. Una simulación de expansión en frío fue hecha en el orificio central para inducir esfuerzos residuales compresivos en las cercanías del orificio. El proceso de expansión en frío simuló el proceso de expansión directa, mediante el paso de un herramental sobredimensionado con un radio de 3.305 mm a través de del modelo de placa con orificio al centro. La simulación numérica fue hecha mediante el análisis de elemento finito. La propagación de la grieta fue hecha mediante el modo de carga, o modo de apertura I. Grietas simétricas a través de todo el espesor que emanan del orificio central de la placa fueron asumidas.

Múltiples modelos de elemento finito fueron necesarios para implementar las siguientes variables de investigación: comportamiento lineal-elástico del material, carga cíclica, comportamiento elasto-plástico del material y esfuerzos residuales en el modelo computacional de placa con orificio al centro. Sistemáticamente, el primero modelo desarrollado fue un modelo base para el cual la expansión en frío no fue considerada y solamente fue estudiado el comportamiento lineal-elástico del material y carga estática. El modelo computacional base de placa con orificio al centro fue validado mediante dos soluciones analíticas reportadas en la literatura. Además del modelo base de placa con orificio al centro, un modelo lineal-elástico para un espécimen de tensión compacto (CT-espécimen) fue desarrollado y validado con resultados experimentales reportados en la literatura.

Una vez que el modelo base lineal-elástico de la placa con orificio al centro fue validado, los siguientes modelos computacionales fueron desarrollados: primero, un modelo de placa con orificio al centro para comportamiento elasto-plástico del material y carga estática. Segundo, el caso de carga cíclica fue simulado en el modelo elasto-plástico de placa con orificio al centro, y finalmente, el proceso de expansión en frío (condición de esfuerzos residuales) fue implementado al modelo elasto-plástico de placa con orificio al centro. El modelo de placa con orificio al centro considerando

comportamiento elasto-plástico del material y condición de esfuerzo residual fue definido como el modelo parametrizado de placa con orificio al centro.

La simulación del proceso de expansión en frío generó un campo de esfuerzos residuales no uniforme en las cercanías del orificio. El campo no uniforme de esfuerzos residuales fue capturado mediante la técnica de tres niveles de sub modelado de elemento finito. La técnica de sub modelado de elemento finito está basada en la simplificación de un problema mediante la división de dicho problema en modelos simples y con una localización específica, esto mientras se optimiza el tiempo de implementación y solución. El campo 3D de esfuerzo residual estimado por las simulaciones fue considerado como una condición inicial para las simulaciones de crecimiento de grieta por fatiga. En general, esfuerzos residuales a tensión dañan los componentes mecánicos acelerando el crecimiento de grieta por fatiga, mientras que los esfuerzos residuales compresivos retardan la iniciación y propagación de grietas por fatiga.

La comparación entre los campos de esfuerzo residual estimados mediante la técnica de sub modelado de tres niveles es reportada en el presente trabajo, además, la influencia del campo de esfuerzo residual estimado por los tres niveles de sub modelado en las simulaciones de fatiga fue estudiado.

Un estudio entre las diferentes metodologías, tal como la integral de contorno, las correlaciones de desplazamientos y esfuerzos, fue hecho para definir el método óptimo para estimar el factor de intensidad de esfuerzos K en las simulaciones de fatiga, además, la relación empírica de Paris-Erdogan se utilizó para estimar las velocidades de crecimiento de grieta da/dN. Finalmente, los valores de da/dN estimados por el modelo computacional para crecimiento de grieta por fatiga en componentes mecánicos fueron validados contra un estudio experimental reportado en la literatura.

Los valores de da/dN estimados por el modelo computacional para crecimiento de grieta por fatiga en componentes mecánicos mostraron la misma tendencia general que los datos experimentales, sin embargo, ligeras diferencias fueron encontradas. Las diferencias entre los resultados numéricos y experimentales son atribuidas principalmente a la compleja naturaleza no uniforme del campo 3D de esfuerzos residuales que fue generado por el proceso de expansión en frío además de las variaciones locales en el material cercano al orificio.

Todas las simulaciones fueron hechas en el programa de elemento finito ABAQUS® 2018, en el Centro de Investigación y Estudios de Posgrado (CIEP) de la Universidad Autónoma de San Luis Potosí.

CONTENTS

ÍNDICE

LIST OF FIGURES

LIST OF TABLES

INTRODUCTION

INTRODUCTION

Typically, when a mechanical system and therefore their components are subjected to loads that are below the material´s yield strength, it is not expected the system to fail, though, when the applied loads are not static but cyclic, a gradual damage in the components occurs, weakening the whole system[1]. The characteristic flaw caused by the fatigue are the cracks, which represent a potential risk on the normal operation of the system, especially if they remain undetected, the cracks can derive on the component fracture and therefore on a catastrophic failure.

The potential catastrophic consequences that can be produced by cracked components, have been reduced due to the scientific and technological advances in materials and fabrication processes. However, the stress raisers, peak stresses, environment, and the inherent defects of the material and processing, plus the service loads have led the fatigue phenomena to remain as the main cause of mechanical failures in several systems such as aircraft [2]. High-tech components are required by the transportation industry; aerospace, automotive and railway systems. These components must be engineered designed to be reliable and safe over the long-term, so the manufacturers require new or revised methods and procedures to enhance the component´s useful life. Besides of a better understanding and prediction of the fatigue life in cracked components.

An effective method to enhance the fatigue life in mechanical components is the residual stresses induction. An efficient technique used to induce residual stress within a mechanical component, is cold worked hole expansion. The cold hole expansion consists on passing an oversized rigid expander through a drilled component with a smaller radius. Due to the expansion, a residual stress field is left behind on the vicinity of the hole. It has been demonstrated that the residual stresses have a direct repercussion in the fatigue life, since the tensile residual stress accelerate the damage while the compressive residual stress is beneficial and delay the fatigue crack growth[3][4]. By the cold hole expansion, a non-uniform 3D residual stress is generated through the thickness of the expanded component . That is precisely one of the main constraints of the cold hole expansion technique, the nature of the residual stress field, lead to complex repeatability on serial processes and complicated measurement of them.

Despite the new trends on composite materials, the aluminum alloys are among the top chosen materials for the transportation industry due to the aluminum mechanical characteristics such as the strength-density relation, thermal conductivity, corrosion resistance, recyclability and ductility. A weight reduction up to 50% can be achieved by the substitution of steel by aluminum within body-in-white on the automotive industry, this can result on 20-30% total vehicle weight reduction when other weight optimizations are added. Moreover, the zinc coats are not necessary for aluminum to

achieve acceptable paint durability, such as with the steel [5], besides the aluminum is a suitable material for fatigue life improvement treatments [6]. In the present work the aluminum alloy 6061-T6 has been selected to be the analyzed material due to its common use in fabrication and consumption on the industry such as in the wing tip skin and frame in aircraft [7].

In recent years, the numerical simulations have become a relevant tool within the mechanical engineering development. The traditional development process at which several resources had to be invested on design, prototyping and try-failure tests is undergoing through several changes due to the new technological society demands, which have led to the research community to optimize resources. By the usage of design software in conjunction with the finite element analysis, the behavior of the mechanical components and systems can be predicted and studied without any physically test.

The present work presents the development of finite element computational models based on the damage tolerance design. The computational models have been proposed for the prediction of fatigue crack growth rates and evaluation of fatigue life in aluminum alloy 6061-T6 laboratory specimens (rectangular plate drilled at the mid-point and compact tension specimen). Moreover, the present work shows the influence of the cold hole expansion, i.e. residual stress, in the fatigue crack growth rates. All the numerical results have been compared with closed-form solutions and experimental results reported on the literature.

OBJECTIVES

General Objective:

Development of a fracture mechanics computational model for the prediction and evaluation of the fatigue crack growth and fatigue life in mechanical drilled components made of the aluminum alloy 6061-T6.

Specific objectives:

1. To develop a computational base model for the analysis of a radial crack emanating from a drilled plain hole within a plate subjected to static loading and linear-elastic material behavior.
2. To apply closed-form solutions for a radial crack emanating from a plain hole for the validation of the computational base model
3. Application of a parametric analysis to the computational base model for the following research variables:

- Elastic-plastic material behavior
- Cyclic loading
- Cold worked hole (initial residual stress)

4. To validate the parametrized computational models based on experimental results existing on the literature.

HYPOTHESIS

The traditional perspective is that residual the stresses (RS) are an undesired consequence from the manufacturing processes, though, a favorable RS distribution can be set into mechanical components, thus the fatigue performance of such components can be improved. Some of the techniques that induce favorable RS are the peening and the cold hole expansion. A non-uniform RS field is generated by the cold hole expansion technique, such RS field has a direct repercussion on the fatigue life of mechanical drilled components whether the RS is tensile or compressive. The experimental measurement of the RS generated by the cold hole expansion is a challenging task, from a technical and economical point of view but is essential within the fatigue life estimations. A reliable alternative for the prediction of RS is the numerical simulation based on the finite element (FE) analysis. A fracture mechanics computational model based on the FE analysis is proposed to predict the RS field generated by the cold hole expansion and therefore evaluate the fatigue life modification within a cracked mechanical component. The correlation between the computational model and the fatigue life estimations will be performed based on the capability of the computational model to determine the stress intensity factor K and use it as a single parameter for the prediction of fatigue crack growth (FCG) rates in components with RS.

JUSTIFICATION

Some of the principal failure modes within the mechanical components are the corrosion, the brittle fracture, overloads and creep, among others. However, despite the technological advances in science and technology, the fatigue mechanism remains as one of the principal failure modes within the engineering components. According to the study reported by Findlay *et al.*[2], the fatigue failure mechanism is the first failure mode in aircraft components and range second for all the engineering components, just below the corrosion mechanism. The characteristic flaw generated by the fatigue are the cracks, which, are actually the most common cause of structural failure in aircraft [2]. Moreover, the most common fatigue crack initiation sites within the aircraft are the fastened joints, in fact, fatigue fracture in fasten holes stands for more than 50% of in-service failures of aircraft components [2], [8], [9]. Fastened joints are very common within the aircraft, especially in the

fuselage skin and frame [7], [9]. According to the study reported by Latger *et al.* [10], the manufacturing process of Airbus wings, requires approximately 40 million holes annually. Besides, aircraft fuselage is commonly made of aluminum alloys [9],[10]. The aluminum alloys mechanical properties, the continuous innovation on metallurgy, plus the years of experience in aluminum manufacturing have settle the aluminum alloys as one of the top materials for aircraft in the coming years [6].

BACKGROUND AND LITERATURE REVIEW

1.1 MATERIAL

On the early stages of aircraft, the primary material used were the wood, but nevertheless since approximately the 30's the aluminum has dominated the market of production and consumption of the aviation industry[6], Some other markets where the aluminum is one of the leading materials are the food containers and packaging, construction, marine and automotive industries[11][5].

The pure aluminum is a non-ferrous malleable material, usually used on the wire and sheet production, however the pure aluminum is not an adequate material for structural application. To improve the aluminum properties needed for structural applications, other materials are used as alloy metals[12]. Several aluminum alloys have been developed through the years to accomplish the necessities of the industry, in general, looking forward to accomplishing the drivers that lead the different markets, such as weight-strength relation, corrosion resistance, fracture toughness, manufacturability and the acquisition and maintenance costs.

The aluminum alloys are classified by series and each series consists of four digits. The first digit is the group of the alloy, the second digit is the change of the original alloy or the impurity limit, the zero value is the original alloy and numbers from one to nine are the modifications. From the 2xxx series up to the 8xxx series the last two digits are the different aluminum alloys of each group [12]. Table 1 shows the aluminum alloy classification[11].

Table 1. Aluminum alloys denomination [11]

Denomination	Alloy material
1xxx	Commercially pure aluminum
2xxx	Copper (Cu)
3xxx	Manganese (Mn)
4xxx	Silicon (Si)
5xxx	Magnesium (Mg)
6xxx	Magnesium (Mg) and silicon (Si)
7xxx	Zinc (Zn) and Magnesium (Mg)
8xxx	Others

Regarding the hardening of the aluminum alloys, it can be classified by solid solution hardening and precipitation hardening. The solid solution hardening mode is the addition of the alloying material

atoms by substitution or insertion within the aluminum matrix. On the other hand, the precipitation hardening mode is obtained by thermal treatments. The series 1xxx, 3xxx and 5xxx are mainly hardened by solid solution, while the series 2xxx, 4xxx, 6xxx, 7xxx and 8xxx are mainly hardened by precipitation, i.e. By thermal treatments [12]. Table 2 shows the designation of the thermal treatments for aluminum alloys.

Table 2. Quenching denomination for aluminum alloys [11]

Denomination	Definition
F	As fabricated
O	Annealed
H	Cold work hardened
T	Thermally treated
W	Treated with solutions

According to the aluminum alloy classification above-mentioned, the aluminum alloy 6061-T6, which was the alloy selected for the present work, is an Al-Mg-Si alloy thermally treated and aged artificially. The thermal treatment and the artificial aging basically consist on three steps: 1 Solubilization, which is the dissolution of the alloying components. 2 Cooling, which consist on obtaining an oversaturated solid solution and 3 artificial aging, which is the precipitation from the oversaturated solution at a temperature above the room temperature [12]. Typical mechanical properties of the aluminum alloy 6061-T6 are shown on Table 3 [11].

Table 3. Mechanical properties of aluminum alloy 6061-T6 [11]

Property	Value
Young's Modulus	68.9 - 71 GPa
Poisson's ratio	0.33
Yield strength	275 - 276 MPa
Max. Strength	310 MPa
Vickers Hardness	107
Fatigue limit strength	97 MPa
Fracture toughness	29.1 MPa$\sqrt{m}$

Aluminum alloy 6061-T6 presents excellent corrosion resistance due to the formation of a thin alumina film on the surface, low density (2.7 g/cc) compared against the typical steel density (8 g/cc), high strength-weight ratio and good machinability (50% of a 0-100 scale for aluminum alloys) [13].

1.2 FATIGUE

The reduction in the ability of a mechanical component to resist stresses below the yield strength generated by cyclic loading is called *fatigue*. The cyclic loading is defined as fluctuant loads that can be originated mechanically or thermally. Each loading cycle has a maximum and minimum value. The maximum and minimum loads at each cycle generates also a maximum and minimum stress value and the corresponding amplitude between them, moreover a mean stress and a ratio can be defined. The ratio is the minimum stress split by the maximum stress but also the minimum load and split by the maximum load. Eqs. 1-3 show the stress amplitude, mean stress and load ratio.

Stress amplitude

$$\sigma_a = \frac{\sigma_{max} - \sigma_{min}}{2} \qquad (1)$$

Mean stress

$$\sigma_m = \frac{\sigma_{max} + \sigma_{min}}{2} \qquad (2)$$

Stress ratio

$$R = \frac{\sigma_{min}}{\sigma_{max}} = \frac{P_{min}}{P_{max}} \qquad (3)$$

Figure 1 shows the schematic of three cyclic loading cases plus the schematic of the variables presented on Eqs. 1-3.

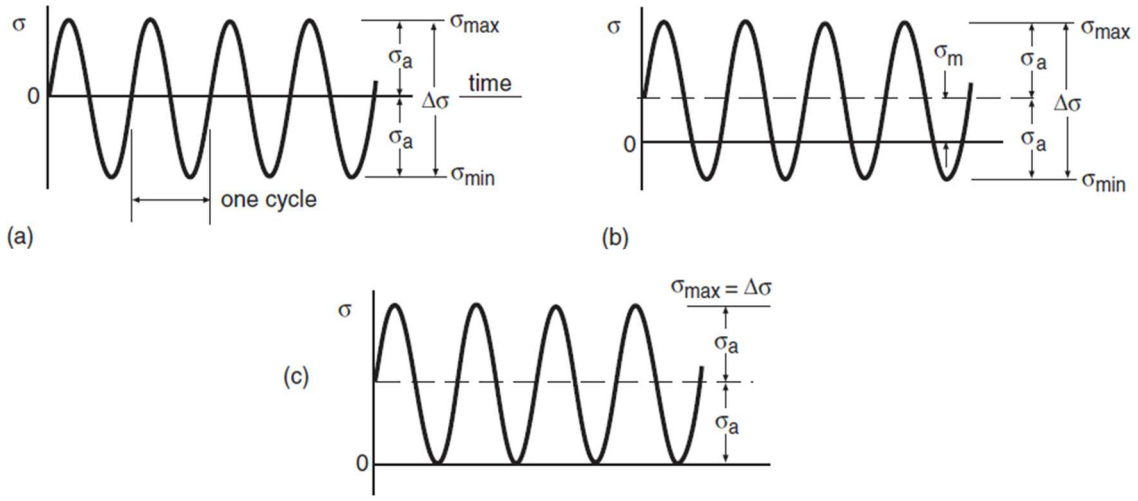

Figure 1 Schematic of cyclic loading a) Completely reversed stressing, zero mean stress b) Non-zero mean stress and c) Zero-to-tension stressing [1]

Nowadays, there are three major approaches for the study of fatigue and its failure. First, the *stress-based* approach, generally used on the high cycle fatigue where the deformations are primarily elastic due to low stresses. The characteristic diagram for the stress-based approach are the so called Wöhler curves (*S-N* curves) which describe the behavior of a given material and typically are affected by several factors such as the fatigue mean stress, the specimen's geometry, the chemical environment, the temperature and the cyclic frequency, among others. This approach is generally known as design based on infinite life.

The second approach is the *strain-based,* generally used for the low cycle fatigue regimen where the amount of plastic deformation is significant in response to high stress levels. The characteristic diagram for the strain-based approach is the strain as a function of the number of cycles (ϵ-N) diagram. However, neither the stress-based nor the strain-based approaches incorporate the possibility of evaluating cracks in components.

Finally, the *fracture mechanics* is the third approach, which is used by the damage tolerance design philosophy and focuses on the growing cracks in the components by quantifying the critical combination of the crack size, fracture toughness, geometry and the applied stresses by either an energy ($\mathcal{G}$) or a stress intensity tactic (K). The energy tactic is known as strain energy release rate and refers to the energy per unit crack area required to extend the crack. On the other hand the stress intensity tactic involves a characteristic factor known as stress intensity factor K. K characterizes the severity of stresses surrounding the crack tip by associating the geometry, crack size and applied

stress [1]. The characteristic diagram for the fracture mechanics approach is the fatigue crack growth rate as a function of the stress intensity factor range diagram ($\frac{da}{dN} - \Delta K$) [1][14].

The analysis of the cracked specimen will be focused on the loading mode I shown on Figure 2, since most cracking problems within engineering applications are related to such mode or crack surface displacement. Mode I is caused mainly by tensile loads while the other two are caused mainly by shear loading in different directions, as shown on Figure 2.

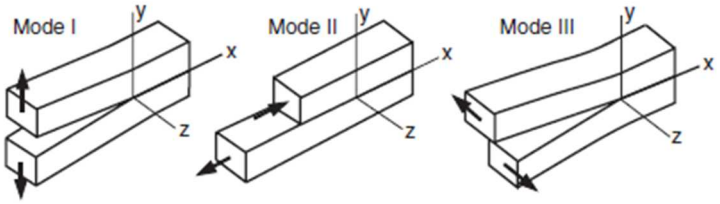

Figure 2. Basic models of crack surface displacement or loading modes [1]

1.3 FRACTURE MECHANICS

The present work will be based on the fracture mechanics approach. Despite an elastic-plastic material model was considered, the present work is based on the linear elastic fracture mechanics (LEFM), which basically implies that the material follows the Hooke´s law. It is possible to use the LEFM since the plasticity region generated at the crack tip is very small regarding the crack length and component dimensions, as shown on Figure 3, thus the stress intensity factor *K*, which characterizes the severity of the crack situation, remains valid. Further information for the stress intensity factor will be given in the following paragraphs.

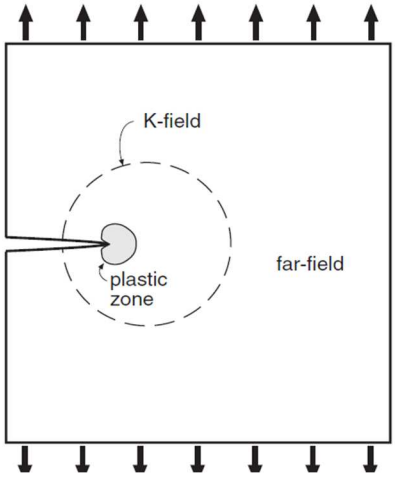

Figure 3. Crack schematic and the plastic zone at the crack tip. K-field or K-dominance zone [1]

The measurement of the plastic zone near the crack tip can be computed by two methods: The Irwin approach and the and the strip-yield model. Eq. 4(a)-(b) shows the Irwin approach and the strip-yield model respectively, both used to estimate the plastic zone at the crack tip.

$$2r = \frac{1}{\pi}\left(\frac{K}{\sigma}\right)^2 \qquad (4a)$$

Where r is the plasticity radius, K the stress intensity factor corresponding to the crack length and σ the applied stress.

$$\rho = \frac{\pi}{8}\left(\frac{K_I}{2\sigma_{YS}}\right)^2 \qquad (4b)$$

Where K_I is the corresponding mode I stress intensity factor, σ_{YS} the yield strength and ρ represents the length of the plastic zone.

For the present work the Irwin approach was used, such approach is based on the use of the elastic stress analysis to estimate the elastic-plastic boundary. The boundary between the elastic and plastic behavior occurs when the normal stress (σ_{yy}) in a linear elastic material satisfy a yield criterion. For plane stress conditions, yielding occurs when $\sigma_{yy} = \sigma_{YS}$ [14].

Within the literature [14], the plastic zone shape is assumed to be a circular area while the stress field distribution exhibits an elliptical-kind shape. Figure 4 shows the elliptical-kind shape for plane stress and plain stress generated by the loading mode I.

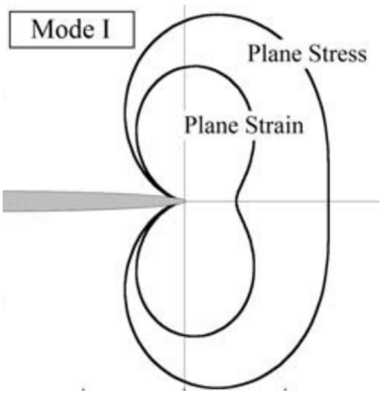

Figure 4. Crack tip plastic zones approximate shape for loading mode I [14]

The damage tolerance design (fracture mechanics approach) is an approach based on the combination of the geometry, crack size, applied stress to a body and the fracture toughness, which is the capacity of a material to resist failure due to a crack. Such combination is evaluated by a single factor *K*, known as stress intensity factor. If *K* is known the entire stress distribution at a crack tip can be computed via Eq. 5(a)-(c), i.e. the *K* factor completely characterizes the severity of a crack within a component [14].

$$\sigma_{xx} = \frac{K}{\sqrt{2\pi r}} cos\left(\frac{\theta}{2}\right)\left[1 - sin\left(\frac{\theta}{2}\right) sin\left(\frac{3\theta}{2}\right)\right] \quad (5\text{-a})$$

$$\sigma_{yy} = \frac{K}{\sqrt{2\pi r}} cos\left(\frac{\theta}{2}\right)\left[1 + sin\left(\frac{\theta}{2}\right) sin\left(\frac{3\theta}{2}\right)\right] \quad (5\text{-b})$$

$$\tau_{xy} = \frac{K}{\sqrt{2\pi r}} cos\left(\frac{\theta}{2}\right) sin\left(\frac{\theta}{2}\right) cos\left(\frac{3\theta}{2}\right) \quad (5\text{-c})$$

Figure 5 shows the stress state for an element near the crack tip.

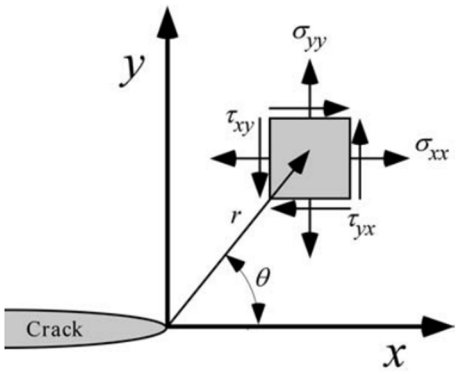

Figure 5. Stress state for an element near the crack tip [14]

Within the fracture mechanics approach, there are different methodologies to estimate the stress intensity factor *K* and the fatigue life, such as closed-form solutions, contour integral method, stress ahead the crack tip correlations and displacements behind the crack tip correlations. However, there are some cases where there the most adequate methodology to determine the *K*-factor is not established such as for the case of variable amplitude cyclic loading, overloading loading cycles and the presence of residual stress near the crack tip.

Eq. 6 shows the general structure for the closed-form solutions reported on the literature for an ideal sharp crack in a linear-elastic and isotropic material. The differences between an ideal sharp crack

and a real crack are shown on Figure 6. The real crack tip shape is generated due to the severe plastic deformations occurring at the crack tip, such severe deformation generates the ideal sharp crack tip to become blunted.

$$K = F_d S\sqrt{\pi a} \qquad (6)$$

Where S is the stress applied on the remote field, a is the crack length and F_d is the characteristic shape factor which depend of the geometry of the specimen.

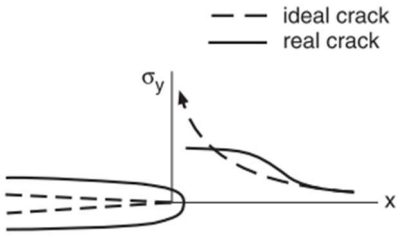

Figure 6. Schematic of an ideal and a real crack tip behavior [1]

The aim of the fracture mechanics (damage tolerance design) is the prediction of the remaining life of cracked components. Thus, the fatigue crack growth rates (*da/dN*) within a mechanical cracked component can be associated with the stress intensity factor *K* and the size for failure can be computed if the fracture toughness is known, such crack failure size is commonly known as crack critical length [14]. The correlation between *da/dN*-values, *K*-values and fracture toughness is generally given by fatigue crack growth (FCG) modes. Within the literature there are numerous FCG models, however, the models varies from one another in the fitting parameter required. Some of the FCG used within the damage tolerance design are the Foreman model the Walker equation, the Paris-Erdogan model, among others. The Foreman model take into account the material fracture toughness K_c.The Foreman model can predict accelerated growth near the final toughness, and it can be used to fit data in regions II and III. In the Walker equation the effects of the stress ratio R is considered. An increase in the R-ratio of the cyclic loading causes growth rates for a given ΔK to increase, the effect is usually more pronounced for brittle materials. The Paris-Erdogan model was the first FCG model proposed on the early 60's, moreover, is the simplest model to predict fatigue life. The Paris-Erdogan model and the Walker equation are only capable to predict fatigue life during the stable crack propagation, or region II of the curve shown on Figure 7.

Figure 7 shows the *da/dN*-values as function of the ΔK-values which is the characteristic diagram of the damage tolerance design philosophy. The first region of the curve shown on Figure 7 is defined as the threshold region. At the threshold region it is common to define the cracks as "short cracks" and such short cracks are mostly influenced by the microstructure. The fracture mechanics concept of the stress intensity factor K is not applicable for short cracks [15]. The first region also shows the transition between the short and long cracks. Within region two of Figure 7 intermediate values of ΔK can be appreciated. At intermediate values of ΔK there exists a linear behavior given by the Paris-Erdogan empirical relation (Eq. 7). The predictions about the residual life as well as the actual residual fatigue life for damaged cracked mechanical components are mostly given by Eq. 7, because it is the region of stable fatigue crack growth (FCG) and the cracks are large enough to be detected by non-destructive tests. Finally, it is defined that the unstable fatigue crack growth (Region 3 of Figure 7) and sudden failure occurs when the stress intensity factor K approaches to the fracture toughness of the material K_{IC}.

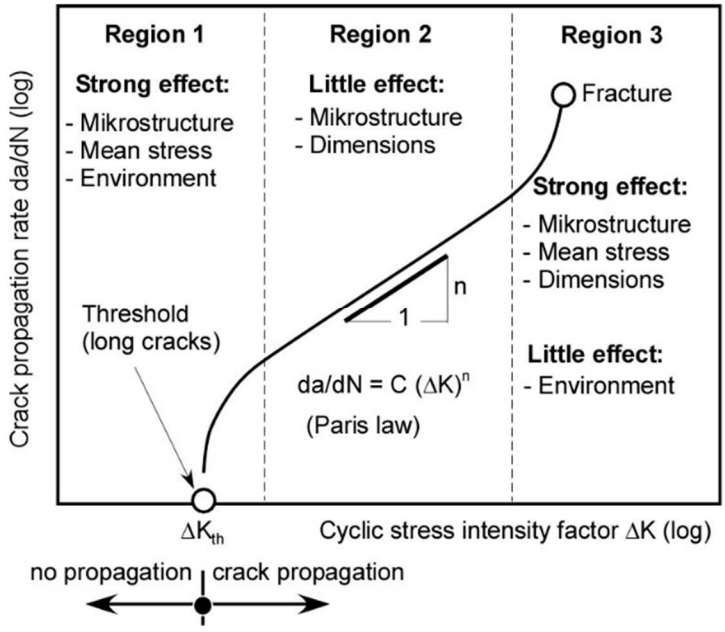

Figure 7. The three regions of the characteristic diagram of the fracture mechanics approach [15]

As previously mention, regardless of the method used, once the *K*-factor has been computed it is possible to associate *K*-values with the crack growth per cycle, or fatigue crack growth rate (*da/dN*). In the present work the Paris-Erdogan empirical relation shown on Eq. 7 has been used.

$$\frac{da}{dN} = C\Delta K^m \qquad (7)$$

Where the *C* and *m* are the fitting material coefficients determined experimentally. The *C* coefficient represent the intercept of the linear region extension with the vertical axis (*da/dN* axis) and the *m* coefficient is the slope of the graph. The least square estimation is considered as the main method to evaluate the material coefficients [16]. Moreover, the computation of the fitting material coefficients is fundamental to estimate accurate fatigue crack growth rates and therefore, accurate fatigue life. Despite the material coefficients are experimentally determined for a certain material, such coefficients can vary due to localized material flaws and environmental conditions such as Tanaka *et al.* demonstrated on their study where a considerable variability were found on 25 identical specimens under similar loading conditions. A method used to improve the estimation of the fitting material coefficients is the table look-up scheme. Through the table look-up scheme, it is possible to describe the *da/dN*-values as function of the ΔK-values or vice versa. A clear example of the table look-up scheme application is the use of Damage Tolerance Design Handbooks information along with table look-up algorithms in crack growth life predictions.

1.3.1 Stress intensity factor evaluation (*K*-values evaluation)

As previously mentioned, the stress intensity factor *K* can be calculated from a diversity of methods within the fracture mechanics approach. The methods used in the present work for the *K* calculus were the closed-form solutions, the stress correlation, the displacements correlation and the contour integral method (*J*-integral method).

The closed form solutions, generally, are analytical solutions proposed for the ideal sharp crack case and linear-elastic isotropic material. The general structure of the closed-form solutions was presented on the Eq. 6. The general structure of the closed-form solutions has been based on the theory of linear elasticity, such as in Eq. 5(a)-(c). The stresses in Eq. 5(a)-(c) seem to approach an infinite value as *r* approaches the zero-value, that is to say, as *r* approaches the crack tip. Thus, the stresses are proportional to $1/\sqrt{r}$ and a mathematical singularity exists at the crack tip and no value of stress at the crack tip can be given. Note that all the stresses on Eq. 5(a)-(c) are proportional to the stress intensity factor *K*, thus, *K* characterizes the crack. The mathematical definition of *K* is shown on Eq.

8; however it is generally expressed as previously shown on Eq. 6 where the dimensionless shape factor *F* is needed to account the differences between geometries [1].

$$K = \lim_{r,\theta \to 0} \left(\sigma\sqrt{2\pi r}\right) \qquad (8)$$

For the present work the closed-form solutions reported in the literature for Matos *et al.* [17] as well the one reported by Dowling [1] were considered. The closed-form solution reported by Matos *et al.* [17] uses a strip-yield approach for two radial symmetric cracks of length *a* within an infinite plate with a central hole of radius r_h under plane stress conditions. Moreover, the closed-form solution proposed for Matos *et al.* [17] is an extension of the Nowell´s plane stress model[18]. The plane stress Nowell's model uses three sets of boundary elements that represents the crack, the strip-yield and the growing crack, Matos *et al.* [17] adapted such model (Nowell's) for the center hole geometry. However, the closed-form solution proposed by Matos *et al.* [17] as well as the presented by Dowling [1] exhibits the same basic structure of the previously presented Eq. 6 or rather the same structure than Eq. 8. Besides the closed-form solutions presented differ from one another by the shape factor. Eqs. 9(a)-(b) show the closed-form solutions proposed for Matos *et al.* [17] and by Dowling [1] respectively.

$$K = S\sqrt{\pi a}\,\sqrt{1-\gamma}(1 + 0.358\gamma + 1.425\gamma^2 - 1.578\gamma^3 + 2.156\gamma^4) \text{ where } \gamma = \frac{r_h}{a} \qquad (9a)$$

r_h represents the hole radius, *a* the crack length from the center of the hole to the crack tip and S is the remotely applied stress to the specimen.

$$K = S\sqrt{\pi a}\,0.5\,(3-d)[1 + 1.243(1-d)^3] \qquad \text{where } d = \frac{l}{a} \qquad (9b)$$

Where *a* is the crack length from the center of the hole to the crack tip, *l* is the crack length from the hole edge to the crack tip and *S* is the remotely applied stress to the specimen.

Other techniques used to estimate the *K*-values are the stress and displacement correlation methods. The stress correlation method is based on the stresses ahead the crack tip to estimate the corresponding *K*-values. Within the stress correlation method, the *K*-values ahead the crack tip are estimated through the previously presented Eqs. 5(a)-(b), all variables of such equations are known but the *K*-value. Eqs. 5(a)-(b) are valid only near the crack tip, where the singularity $1/\sqrt{r}$ dominates the stress field and contrary to the closed-form solutions, Eqs. 5(a)-(b) does not consider neither the geometry of the specimen nor the influence of the specimen edge (finite plate) [14]. Once the *K*-values ahead the crack tip have been determined, the graph of the *K*-values as function of the radial distance *r* from the crack tip to the uncracked section can be obtained. By discarding the results from nodal points close to the

crack tip the most approximate solution for *K* can be extrapolated to *r*=0 (crack tip) [19]. Figure 8 shows the stress correlation method schematically.

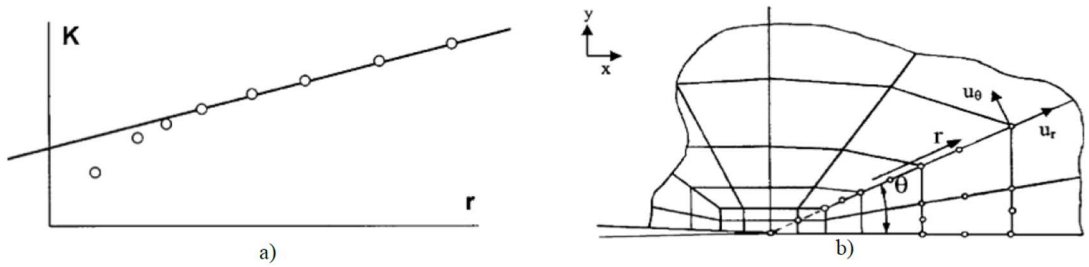

Figure 8. Stress correlation method a) K-values as function of the radial distance and extrapolation r=0 b) Schematic crack tip radial distance and loading angle [45]

The displacements correlation method is based on the displacements behind the crack tip *u* to calculate the corresponding *K*-values. The *K*-values within the displacement correlation method can be computed through Eqs. 10(a)-(b) presented below. Like with the stress correlation method, Eqs. 10(a)-(b) does not consider neither the geometry of the specimen nor the influence of the specimen edge (finite plate) such as the closed-form solutions previously discussed. Once the *K*-values behind the crack tip have been determined, the graph of the *K*-values as function of the radial distance *r* from the crack tip to the cracked surfaces can be obtained. As in the stress correlation method, by discarding the results from nodal points close to the crack tip the most approximate solution for *K* can be extrapolated to *r*=0 (crack tip).

$$u_x = \frac{K}{2\mu}\sqrt{\frac{r}{2\pi}}\, cos\left(\frac{\theta}{2}\right)\left[\kappa - 1 + 2sin^2\left(\frac{\theta}{2}\right)\right] \qquad (10a)$$

$$u_x = \frac{K}{2\mu}\sqrt{\frac{r}{2\pi}}\, sin\left(\frac{\theta}{2}\right)\left[\kappa + 1 - 2cos^2\left(\frac{\theta}{2}\right)\right] \qquad (10b)$$

Where μ is the shear modulus and $\kappa = 3 - 4\upsilon$ for plain strain and $\kappa = (3-\upsilon)/(1+\upsilon)$ for plane stress. υ represents the Poisson's ratio. Eqs. 10(a)-(b) are valid for the loading mode I, which is the studied mode within the present work.

A study reported on the literature by Qian *et al.* [20] performed a comparison between different methods for loading mode I *K*-values calculation. Moreover, Qian *et al.* [20] used both, 2D and 3D Compact Tension (CT-specimen) models for the *K*-values calculation. Within the study reported by Qian *et al.* [20] the stress and displacement correlation methods, among others, were compared. The

material model used within the simulations was defined as a linear elastic material with Young's modulus E of 200 GPa and a Poisson's ratio υ of 0.3. The models used 8-node brick elements and 20-node hexahedral elements for the 2D and 3D respectively. Besides, a total of 2500 and 64000 finite elements were used within the 2D and 3D models. The approximate element size for the finite elements near the crack was 0.02 mm for both, 2D and 3D models. Qian *et al.* [20] also performed a loading simulation for which a 0.3 mm displacement were prescribed to the up side of the models while the bottom remained fixed. The results that Qian *et al.* [20] obtained through the displacement and stress correlations were consistent for the 2D and 3D CT-specimen models such as can be appreciated on Figure 9(a)-(d). Moreover, the results provided reasonable accuracy regarding the K calculation according to the ASTM closed-form solution for the CT-specimen (3620 $MPa\sqrt{m}$).

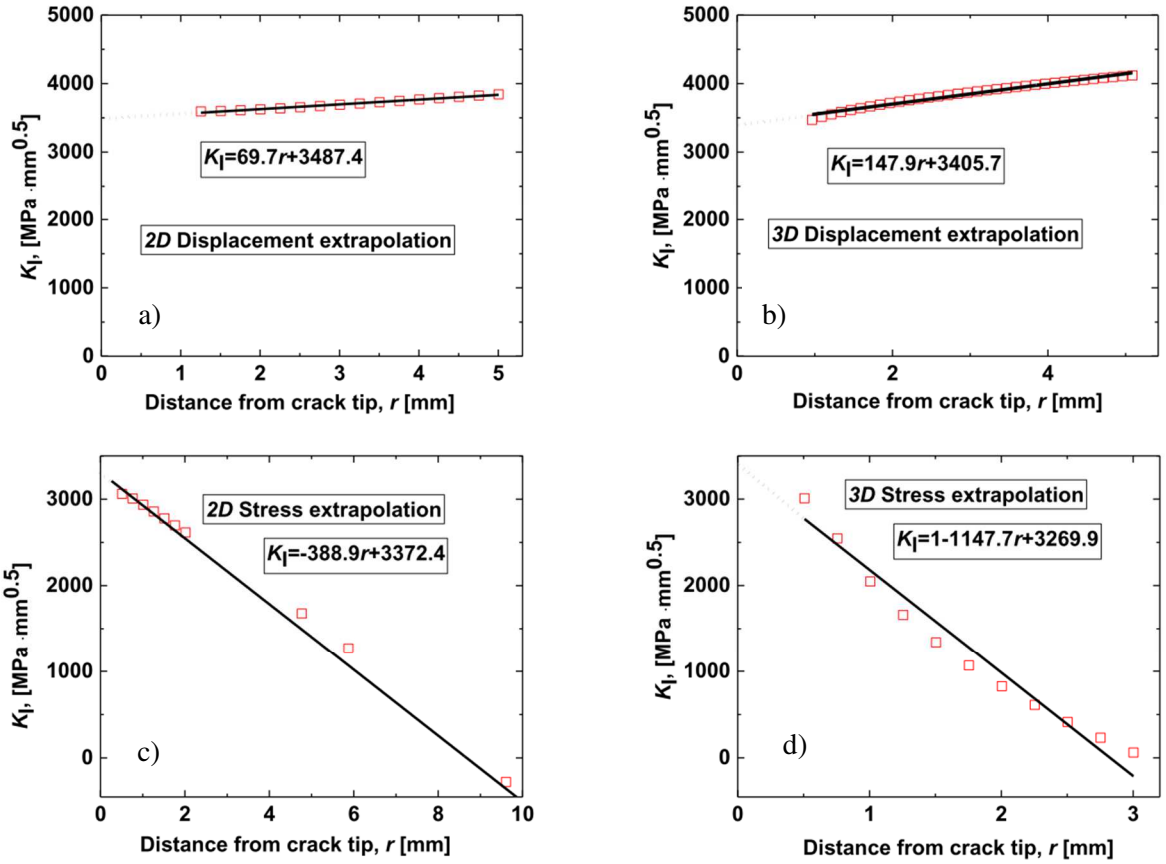

Figure 9. Stress intensity factors calculated through the displacement and stress correlation methods for 2D and 3D models

Another method to estimate the K-values within a cracked component is the contour integral method or J-integral method. By the contour integral method, an anti-clockwise integral path encloses the

crack tip from an initial to a final point which lie on the two crack faces [19]. The path that encloses the crack tip, for linear elastic materials is path-independent. Path independent integrals are generally used in physics to estimate the intensity of a singularity of a field quantity without knowing the exact shape of the field near the singularity. The contour integrals are derived from the conservation laws [21]. A schematic of the contour integral path can be appreciated on Figure 10 along with Eq. 11 which shows the contour integral.

The contour integral is basically an energetic method. The contour integral method is equivalent with the energy release rate in a nonlinear elastic cracked component. That is to say, there are an idealization from the elastic-plastic material behavior to a nonlinear elastic material. The behavior for the two materials is the same when the loading occurs but differ on the unloading. The elastic-plastic material follows a linear unloading path with slope equal to the Young's modulus while the nonlinear elastic material unloads along the same path as it was loaded [14].

$$J = \int_{\Gamma} \left(w dy - T_i \frac{\partial u_i}{\partial x} ds \right) \tag{11}$$

Where w is the strain energy density, T_i the components of the traction vector u_i the displacement vector component and ds the length increment along the contour Γ.

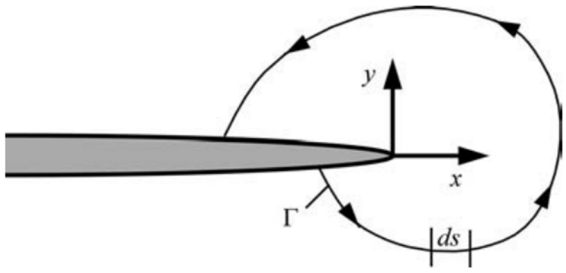

Figure 10. Arbitrary contour around the crack tip of a crack[14]

The energy release rate, and therefore the contour integral method present that the fracture on a cracked component occurs when the energy available for crack growth is sufficient to overcome the resistance of the material [14]. The energy release rate, i.e. the contour integral, can be related to the stress intensity factor K if the material response is linear and for a through crack in an infinite plate subjected to a uniform tensile stress [14]. Eq. 12 shows the relation between the contour integral (J-integral) and the stress intensity factor K for the loading mode I.

$$J = \frac{K^2}{E} \quad (12)$$

Despite the contour integral method is widely used within the rate-independent quasi-static fracture analysis, is mostly used for linear material response analysis since the integral's values within linear-elastic analysis are path-independent, that is to say that can be calculated on the remote field and yet characterizes the conditions within the crack tip. However, it is possible to extend its use to the elastic-plastic analysis, yet the integral's values become path-dependent. The path-dependence is due to the contour integral is based on the strain energy density *w*, from which stresses can be derived, such assumption exclude the local re-arranging of stresses due to the yield condition, hence, the contour integral results depends on whether the contour passes through the plastic zone or not.

The use of the contour integral and elastic-plastic material behavior can be done by generating a path-independent contour integral. To generate a path-independent contour integral along with elastic-plastic material behavior, the contour integral domain must be large enough to surround the plasticity zone and capture only the elastic zone, though when large plastic deformations occurs this is not possible [21].

The computation of the *K*-values for a growing crack turns out to be a complex problem since the evolution of such *K*-values as the crack propagates varies, i.e. the path that the crack tip will follow within the mechanical component cannot be known in advance [22]. As general rule, the crack will propagate along the path which release the maximum energy (energy release rate). In real materials the crack tip path can be deviated due to a number of factors such as the presence of material flaws, a residual stress field and microscopic anisotropy [23]. Due to the irregular path through which the cracks grows various studies for irregular cracks have been reported in the literature (e.g. [24]–[26]), However, for the present work, the zone of the studied specimen which is most probable to generate and propagate cracks is the surface of the specimen, therefore the most critical crack growth is assumed to be along the line of symmetry. Moreover, on the present work the *K*-values for linear-elastic, elastic-plastic, and elastic-plastic with residual stress models were computed through the closed form solutions, stress and displacements correlations and by the contour integral method.

1.4 COLD HOLE EXPANSION EFFECTS IN FATIGUE DESIGN

The primary mechanical components, identified as those which threaten the whole system if fail, are designed to avoid failure due to the service conditions, among which is the fatigue failure. To fulfill this purpose, several techniques have been applied to them such as post processing of the final

manufactured component i.e. quenching, coatings and shot peening, among others, and changes in geometrics details, like in fillets and holes, to reduce the stress concentration, but nevertheless there are limits imposed by the functionality of the components. Hence, alternative methods to improve the fatigue performance must be used.

An effective method to enhance fatigue life without compromising functionality of mechanical components is the introduction of residual stress. The residual stress within mechanical components have the same beneficial effect than applying compressive pre-loads to the component rather than tensile. The resultant stress at the component's stress raiser is reduced due to the compressive residual stress effect.

A common technique used within the aerospace industry, specifically for drilled components, is the cold hole expansion technique. The phenomenon occurring during the cold hole expansion is that while the mandrel is pulled through the specimen, the material on the vicinity of the hole is deformed plastically and then, when the mandrel leaves the specimen the material far from the hole, which only were deformed elastically, generates a compressive residual stress field around the hole. The compressive residual stress around the hole is generated by the elastic strain that is not recovered after the expansion. The compressive residual stress generated by a cold hole expansion can be appreciated on Figure 11.

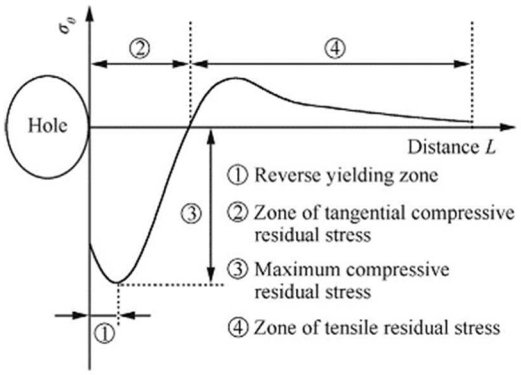

Figure 11. Typical residual stress distribution around an expanded hole [8]

The base of this technique is that by passing an oversized rigid expander through a drilled component a residual stress field is generated along the hole. There are different versions of this technique, basically the variation among hole expansion techniques lies on the type of expander used. Among the common versions of expansion processes are the, split-sleeve, cold hole ball expansion, hole edge expansion and direct mandrel expansion.

In the split-sleeve a mandrel and a split sleeve are used to do the cold hole expansion, the split sleeve is used to avoid the surface damage generated by the interference between the mandrel and the specimen. In the cold hole ball expansion, the cold hole expansion is done by passing an oversized hard steel ball through the specimen's hole to be expanded. The hole edge expansion process is carried out by an indenter through which an axial force *F* is applied to the hole's edge and therefore such zone is strengthened. The hole edge expansion process is limited to surface residual stress generation. The direct mandrel expansion is done by passing an oversized mandrel through the hole of the specimen and removing the mandrel from the other side of the specimen, however the geometry of the mandrel can vary. Moreover, within the split-sleeve hole expansion it is possible to use a mandrel, whether it is tapered or not, and also a ball, such as the cold hole ball expansion technique [8]. Figure 12 shows the direct mandrel expansion process.

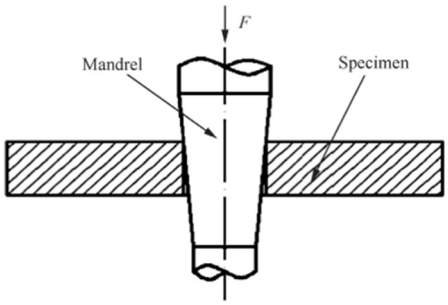

Figure 12. Direct mandrel hole expansion technique [8]

Some of the parameters that influences the hole expansion are the material properties, geometry, lubrication and radial interference. However, one of the parameters that most influences the residual stress generated by the cold hole expansion is the radial interference between the mandrel and the specimen's material. The radial interference is a percentage that represents the degree of expansion, i.e. Accounts the differences between the dimensions of the mandrel and the specimen's hole. The radial interference *e* is calculated according to Eq. 13, where R_1 is the mandrel radius and R_2 the plain hole radius. Common interference values used in the aerospace industry varies from 2 to 6% [8], since it has been demonstrated that that the residual stress increase as the percentage of radial interference increases until 5% and then decrease for values beyond 6% [27]. The residual stress drop after the 5% of radial interference can be appreciated on Figure 13, which shows the results reported by Gopalakrishna *et al.* [27].

$$e = \frac{R_1 - R_2}{R_1}\ x\ 100\% \qquad (13)$$

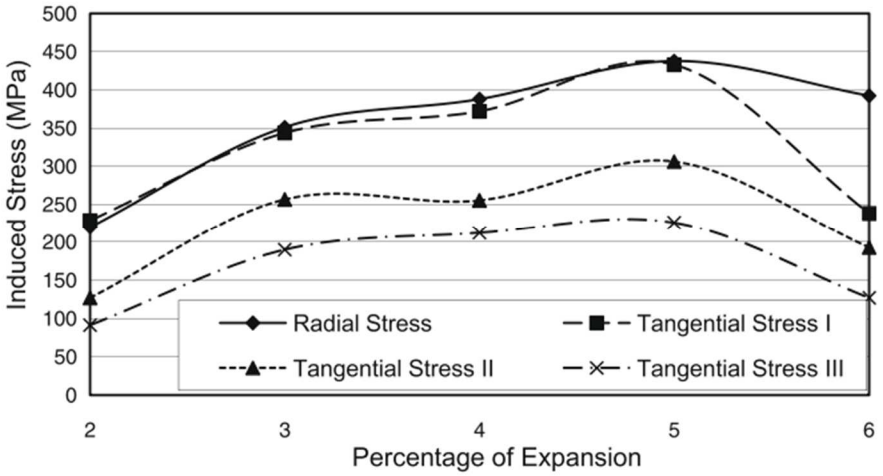

Figure 13. Stresses induced by the cold hole expansion and a tapered mandrel [27]

Despite the improvement on the fatigue life due to the cold hole expansion, one of the main concerns on this technology is the accurate measurement of the residual stress field. It is challenging to measure the residual stress distribution since it is not uniform along the thickness of the specimen. Moreover, the non-uniform residual stress field effect affects the effective stress intensity factor *K*. The effective stress intensity factor considers the residual stress plus the stress intensity factor caused by the external applied load [8].

According to the Fatigue Technology Inc. (FTI), which is the main supplier of cold expansion instruments and technical support, the complete process of cold hole expansion includes the finish reaming of the hole to the nominal dimension. Johnson *et al.* [28] proposed 2D and 3D finite element models which, among other variables, simulated the final reaming of the process. The simulations were performed for a 4% of expansion in aluminum alloys 7050-T7451 and 2024-T351 using isotropic and kinematic hardening material models on ABAQUS® finite element package and the results were compared against experimental results. The study revealed that the finish reaming of the hole wall has a negligible effect on the maximum value and distribution of residual stress field predicted by the finite element models. Figure 14 shows the comparison between the model including the final reaming and the model where the reaming was not included.

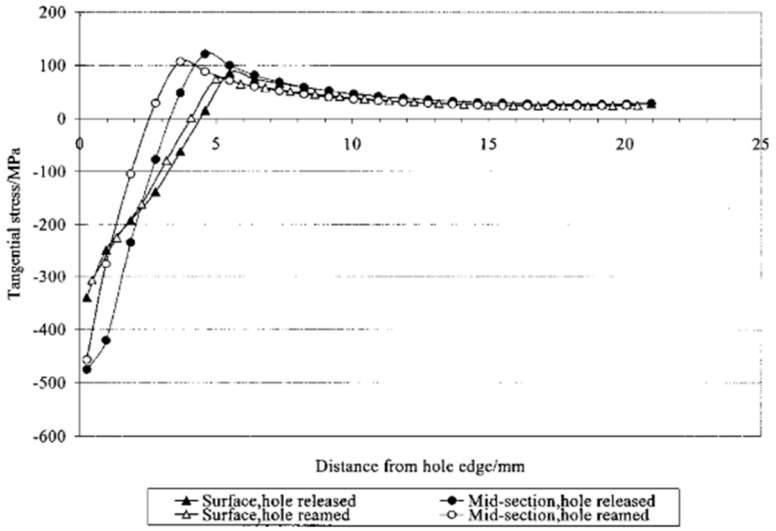

Figure 14. Residual stress predicted by a finite element model with and without the final reaming simulation [28]

Several measurement methods for residual stress have been developed through the years such as the hole drilling and Sachs methods which are destructive tests, X-ray diffraction and moiré interferometry, which are non-destructive methods, but relatively limited to measurement of surface residual stresses and some others that are limited to localized residual stress measurements like the strain gage method. However, it is still a challenging task, from a technical and economical point of view, to measure and predict the distribution of the residual stress, especially for the internal material around the hole.

Due to the limitations of the experimental methods for residual stress measurements such as accuracy constraints, equipment availability and costs, on the recent years the numerical simulations have become an important tool to predict and study the three-dimensional residual stress distributions and its repercussion on the fatigue life.

1.6 STATE OF THE ART FOR COMPUTATIONAL MODELS: COLD HOLE EXPANSION AND FATIGUE LIFE

Finite element simulation has been widely utilized to study the residual stress fields generated by the cold hole expansion on its different variations and therefore its repercussion on the fatigue life of mechanical components. Analytical solutions for the residual stress and stress intensity factors are primarily for plane stress.

Some of the initial attempts to model the cold hole expansion process and its effect on the fatigue life were limited to 2D finite element models. Priest *et al.* [29] presented a 2D finite element model of a drilled rectangular plate. The model considered the Al 2024-T351 mechanical properties for the simulations, moreover the material response was characterized using data reported in the literature from uniaxial tensile tests. The 2D finite element model were proposed to simulate the thickness of the AL 2024-T351 plate by using 600 second-order elements and considering isotropic and kinematic hardening behavior. The cold hole expansion process simulation did not include the mandrel finite element model, besides the process was simulated fixing the nodes on the base of the 2D model and prescribing uniform displacements to the nodes situated at the hole wall. The nodal displacements at the hole wall were such that simulated a 4% of radial interference, i.e. A degree of expansion of 4%. Figure 15 shows the simplified 2D model presented by Priest *et al.*[29] .

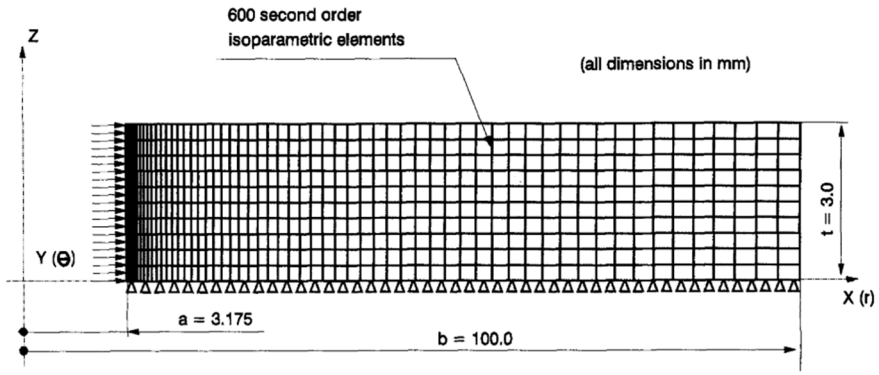

Figure 15. Axysymmetric 2D finite-element model for a cold hole expansion process within an Al 2024-T351 plate [29]

Also, an experimental cold hole expansion with a radial interference of 4% were performed to 6 mm thick aluminum alloy 2024-T351 specimens, then an experimental residual stress measurement was performed by the X-ray diffraction technique. Finally, the results from the 2D finite element model

were compared against analytical solutions as well as against the experimental results. The analytical models used were the Rich and Impellizzeri plane strain model and the Hsu and Forman model for plane stress. The numerical results compare favorably with the analytical solutions. Though, regarding the experimental results, the study shows that the residual stress field vary significantly through the thickness of the plate and therefore neither analytical solutions nor the finite element model were able to represent the complex through thickness residual stress state.

Papanikos and Meguid [30] also proposed a simplified 2D model of a drilled plate shown on Figure 16 The model presented by Papanikos and Meguid [30] considered the Al 7075-T652 material properties for the simulations. Due to symmetry, only one quarter of a rectangular plate was modelled by using six-node triangular elements. A higher element density were used on the region near the hole regarding the model's region far from the hole, such as shown in Figure 16. Moreover, several convergence analyses were conducted. Application of a uniform radial displacement at the hole boundaries were imposed to the model to simulate the hole expansion, so the cold hole expansion simulation did not include the mandrel's computational model. Papanikos and Meguid [30] reported that the simplified 2D axisymmetrical model has some limitations such as it was unable to predict the residual stress variation at the entrance and exit faces, moreover the 2D axisymmetrical model did not account for the contact conditions. Due to the 2D axisymmetrical model limitations a new 3D model were done by Papanikos and Meguid [30]. The 3D finite element model presented the cold hole expansion for adjacent holes and was compared against experimental results. The 3D model simulated the cold nhole expansion of adjacent holes since many aerospace applications involve the cold hole expansion at several holes that are close one to each other. The material model considered for the 3D model remained as that considered for the 2D model. Twenty-node hexahedral elements were used in the region close to the holes so the high gradients could be captured. For the regions of the 3D model far from the holes the 3D model used ten-node tetrahedral elements. The contact interaction between the mandrel and the specimen to be expanded were considered by using contact elements. The 3D model was compared against experimental results reported on the literature. A discrepancy of 8% between the numerical and experimental results is reported.

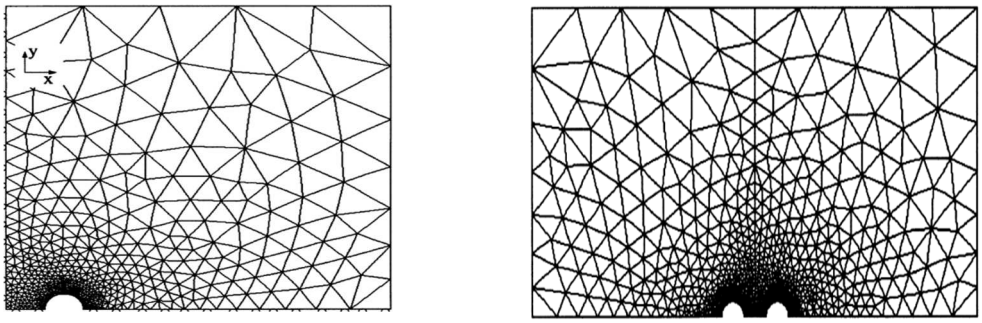

a) b)

Figure 16 Two-dimensional finite element models proposed for a) Single hole and b) adjacent holes [30]

On a later study reported by Matos *et al.* [31] the effects of the common simplifications, normally used for the split sleeve cold worked holes modeling process, and the performance of 2D, 2D axisymmetrical and 3D computational models were evaluated. Some of the common simplifications used for the split sleeve cold worked holes modeling process are the consideration of an infinite domain, i.e. The boundaries of the specimen has no influence on the cold hole expansion process, the usage of symmetry boundary conditions and the uniform hole expansion. The material used for the study reported by Matos *et al.* [31] was aluminum alloy 2024-T3 with elastic perfectly plastic and hardening material behavior. For the 2D and 3D models reported by Matos *et al.* [31] a rigid mandrel was modelled. However, the split sleeve cold worked holes modeled used both, the uniform radial displacement and a contact interaction, to simulate the interference between the mandrel, the split sleeve and the specimen. The 2D model used 5000 bi-quadratic 8-node elements for the aluminum plate, the 2D axisymmetrical model used 15000 4-node linear elements and the 3D model consisted on 41600 3D 8-node linear elements. ABAQUS® 6.2 was used to carry out the analyses. According to the study, it is not recommended the utilization of 2D models to simulate the cold hole expansion process since they do not capture the through thickness variation of the residual stress field. On the other hand, the 2D axisymmetrical and the 3D models provides the possibility to predict the residual stress field variation through the thickness. The 2D axisymmetrical model predicted greater amount of hole enlargement than the 3D since the 2D axisymmetrical model used 50 finite elements through the thickness of the aluminum plate, while the 3D model used only 16 finite elements for the same

region. However, despite the difference between the finite element's density of the 2D axisymmetrical and 3D model similar residual stress were predicted by both models.

An alternative to the 2D axisymmetrical and 3D models for the split sleeve cold worked process also was proposed by Babu *et al.* [32] under the argument that the typical simulations involve many assumptions, such as uniform displacements along the hole edge to simulate the cold hole expansion and the lack of contact interactions between mandrel, sleeve and specimen. The method proposed is based on the nature of the process i.e. In the experimental cold hole expansion process, as the mandrel go through the specimen, the radial interference is achieved gradually, resulting in gradual expansion of the hole layer by layer from the entrance face to the exit face of the specimen. The computational model proposed by Babu *et al.* [32] replicated the above mentioned phenomenon by creating layers within the thickness of the model. The thickness of the proposed model was divided in 16 layers of 4 finite elements each layer, and the cold hole expansion was simulated by gradually prescribing displacement layer by layer. For the model presented by Babu *et al.* [32] the material properties of the aluminum alloys 2024-T3 and 7075-T6 were considered. Moreover, the material model considered the isotropic hardening model. Regarding the mandrel, any computational model was used within the simulations since, as previously mention, the expansion was simulated by prescribing displacement to the layers of the aluminum plate model. The model consisted on a quarter of a rectangular plate due to the symmetry conditions. The quarter plate used 8000 8-node elements for the Al 2024-T3 and 12800 8-node elements for the Al 7075-T6 plate. The variation in the quantity of finite elements used was due to a slight difference in the dimensions of the aluminum plate models.

Good agreement was found between the model proposed by Babu *et al.* [32] and previous 3D contact simulations reported by Johnson *et al.*[28]. Besides, the simulations performed by Johnson *et al.*[28] were compared against experimental results showing a good agreement. The new method proposed by Babu *et al.* [32] is simpler and computationally less complicated than the 3D models, but neglect the axial force flow of the material due to the mandrel interference with the plate. This assumption can lead to considerable differences between residual stresses predicted and experimentally obtained as was remarked by other study reported on the literature by Maximov *et al.* [33]. Figure 17 shows the results of the study reported by Maximov *et al.* [33] where the curves number 1 and 2 are 2D axisymmetrical models proposed by Maximov, curve number 3 is a 2D model for which uniform radial displacements were prescribed to the hole edge, curve number 4 is the "layer by layer" model proposed by Babu *et al.* [32], and the curve number 5 is the experimental measurement of the residual stress through the X-Ray diffraction method.

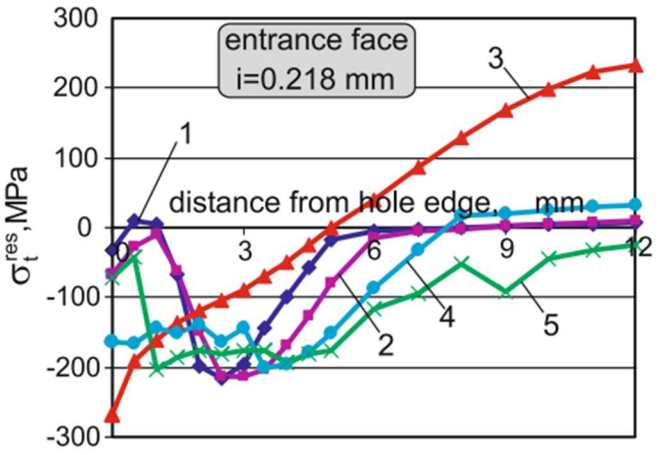

Figure 17. Residual stress obtained by various finite element models and from the experimental X-ray diffraction [33]

As it can be appreciated on Figure 17, the finite element models that prescribed displacements at the hole edge, whether the displacements are prescribed uniformly or layer by layer, overestimate the compressive residual stress at the hole edge and then underestimate the residual stress for the rest of the affected zone.

Regarding the effect of the cold hole expansion in the fatigue life of mechanical components, Chakherlou and Vogwell [4] reported a 3D finite element model for a cold hole expansion of 4.6% of radial interference within a rectangular plate. After the simulation of the cold hole expansion, longitudinal loads were prescribed to the far end of the finite element model, so the residual stress initial condition was considered, moreover, Chakherlou and Vogwell also conducted an experimental study with of the cold hole expansion and the longitudinal loads. The material model used within the plate model proposed by Chakherlou and Vogwell [4] considered the mechanical properties of the aluminum alloy 7075-T6. Moreover Chakherlou and Vogwell [4] considered the kinematic hardening behavior for the material model. The simulation considered the finite element model of the aluminum plate as well as the finite element model of the mandrel. For both finite element model 8-node linear isoparametric elements along with symmetry conditions were used. The aluminum plate finite element model was constrained on the Z direction at the exit face nodes. The cold hole expansion finite element simulations predicted a non-uniform residual stress field throughout the plate thickness with compressive residual stresses near the hole and tensile further from the hole edge. The study reported by Chakherlou and Vogwell [4] can be divided in two, first the cold hole expansion simulation so the initial residual stress condition was considered and then the simulation of incremental longitudinal loads prescribed on the far end of the aluminum plate. The longitudinal loads were such that induced stresses from 0 to 200 MPa. The longitudinal loads were prescribed such that

the loading mode I was simulated. It is reported that for loads that induced normal stresses up to 100 MPa, the longitudinal stress at the hole edge remains compressive for the entrance, middle and exit face planes, i.e. Due to the initial residual stress condition, the effective residual stress at the hole edge (residual stress due to cold hole expansion plus the stress due to the prescribed external load) remains compressive. For applied loads that induced stresses from 100 to 200 MPa, the effective stress at the hole edge increased and became tensile for the three studied planes (Entrance, middle and exit face). As the applied load increased the entrance face became the zone with the most tensile stress values.

As previously mentioned, later on the same study reported by Chakherlou and Vogwell [4], the experimental cold hole expansion and zero-to-tension, constant amplitude fatigue tests were performed. The cold hole expansion was performed on an aluminum alloy 7075-T6 specimen. The specimens had a 5 mm hole at the midpoint which was drilled and reamed before the expansion. The cold hole expansion was performed by inserting a pre-lubricated tapered mandrel. Regarding the fatigue tests, they were performed with sinusoidal cyclic loads (R=0) such that induced stresses between 100 and 200 MPa to the specimen. The results show that the fatigue life for cold hole expanded specimens were almost 10 times higher compared against the plain hole condition such as can be appreciated on Figure 18, where the stress-cycles (S-N) curve of the cold hole expanded specimen is compared against the curve for the specimen without cold hole expansion.

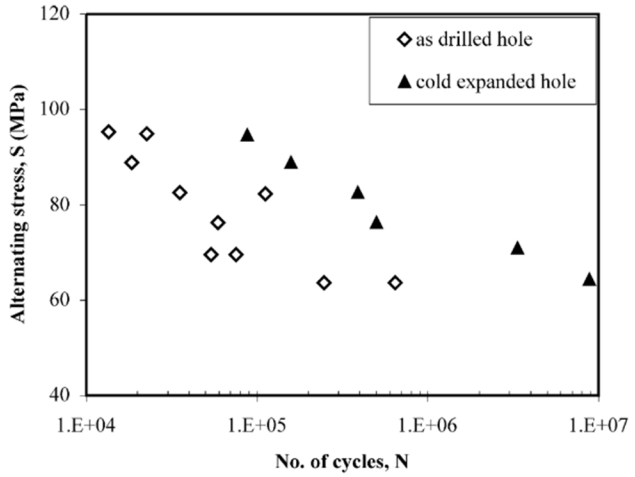

Figure 18. S-N curve for the fatigue life results from a cold hole expanded and a “as-drilled” Al 7075-T6 specimen

The usual enhancement in the fatigue life for cold worked components is 3 to 6 times regarding the plain hole condition as experimentally shown by Gopalakirshna *et al.* [27]. They [27] also concluded that the split-sleeve tapered pin technique produces a greater fatigue life improvement than the split-

sleeve ball expansion technique and that beyond 6 mm from the hole edge the effect of the cold hole expansion is minimal. The maximum value of the compressive residual stress reached by the split-sleeve ball expansion technique was about 350 MPa and 400 MPa for the split-sleeve tapered pin technique. The maximum compressive residual stresses reached by both expansion methods are similar in magnitude to the material yield stress (375 MPa) but the split-sleeve tapered pin technique used more effectively the material strain hardening behavior. Similar results were reported by Yan-li *et al.* [7] where the extension of the affected zone by the expansion embraces an approximate distance of 4.5 mm from the hole edge. The study reported by Yan-li *et al.* [7] was conducted in a 3 mm thick aluminum alloy 6061-T6 specimen. The specimen was drilled at the midpoint and the hole's diameter was 8 mm. The specimen was expanded by a steel tapered mandrel with a maximum radius such that generated a 4% of radial interference. Besides, within the study reported by Yan-li *et al.* [7], 10 specimens were tested under cyclic loads with a load ratio R of 0.1. The residual stress field generated by the cold hole expansion was measured by the X-Ray diffraction method.

Other studies that report a remarkable fatigue life enhancement by the cold hole expansion process in aluminum alloy specimens were divulged by Yongshou *et al.* [34] and Shizen *et al.* [35]. As it can be appreciated on Figure 19, according to the study reported by Yongshou *et al.* [34], the fatigue life was improved by about 6 times regarding the non-expanded specimens. It is also reported that the best fatigue life enhancement was obtained by generating a radial interference within 4 and 6%.

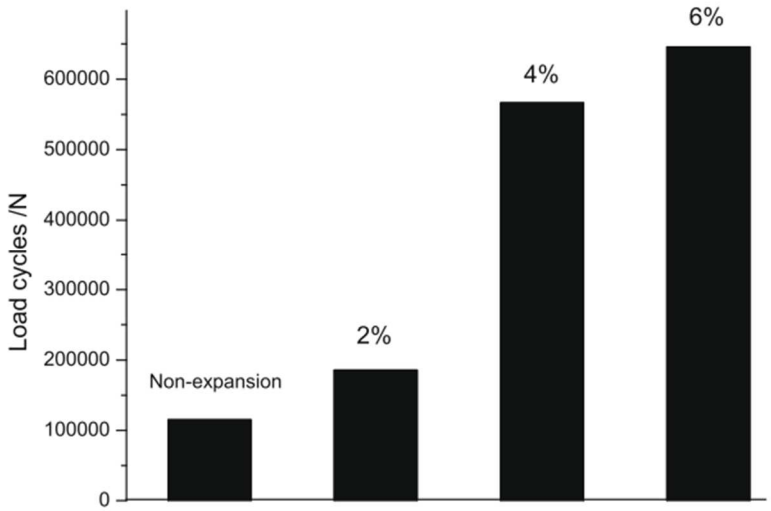

Figure 19. Comparison of fatigue life of specimens with a hole expansion of 2, 4 and 6% of radial interference, and without any hole expansion [34]

On the study reported by Yonshou *et al.* [34], a cylindrical and rectangular 2D finite element models were performed, plus a 3D rectangular finite element model. Moreover, Yonshou *et al.* [34] also performed an experimental study with validation purposes. The study reported by Yonshou *et al.* [34] was performed using the material properties of the aluminum alloy LY12-CZ in the finite element models and the same material for the validation experiment. Regarding the 2D cylindrical model, a plate of 100 mm of radius was modelled with a hole at the midpoint of 2.5 mm radius. The rectangular 2D and 3D models were a plate of 200 by 40 mm (thick of 4 mm for the 3D), with a hole at the midpoint of a radius equal to 5 mm. The numerical study was performed on ABAQUS® finite element package using 4-node bilinear plane stress and 8-node linear brick reduced integration elements for the 2D and 3D models respectively along with symmetry conditions for the three finite element models. The experimental validation of the three finite element models, regarding the residual stress field generated by the cold hole expansion was done by experimentally expanding a rectangular plate and measuring the experimental residual stress through the X-ray diffraction method. Regarding the validation for the fatigue life, the experiment, as well as the simulations, were conducted with constant load amplitude and stress ratio R of 0.1, the maximum applied longitudinal load was such that induced a 100 MPa stress to the specimen.

For the residual stress field, good agreement was found between the finite element models and the experimental results at approximately 3 mm and up from the hole edge. On the other hand, the comparison was not good for the zone near to the hole´s edge. The results of numerical and experimental residual stress field can be appreciated on Figure 20.

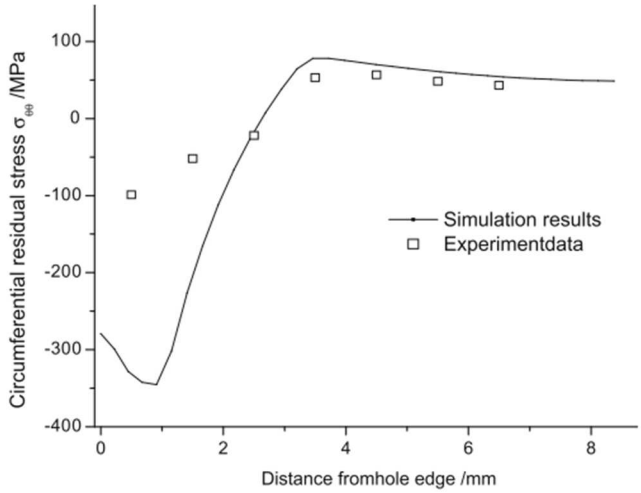

Figure 20. Comparison between numerical and experimental residual stress field due to a cold hole expansion [34]

According to the results reported on the literature by Yonshou *et al.* [34], the predicted residual stress at the hole edge was much more compressive compared against the experimental data, such as shown on Figure 20. Yonshou *et al.* [34] attribute the disagreement between the numerical and the experimental data to the fact that the gradient of the residual stress is very steep near the hole edge and therefore, neither the finite element method nor the X-Ray diffraction measurement were trustworthy. However, the overestimation of the compressive residual stress within the first 3 mm from the hole edge can severely affect the fatigue crack growth estimations end therefore fatigue life estimations.

On the other hand the study reported by Semari *et al.* [3] compares FEM simulations and experimental data regarding the fatigue life of cold hole ball expansion process for aluminum alloy 6082-T6. For the study reported by Semari *et al.* [3] the Single edge notch tension (SENT) specimens with 1.7, 3.4 and 4.3% of expansion were modelled. The SENT specimens are not a drilled component but a dog-bone like specimen which is notched to generate the stress raiser, however for the study reported by Semari *et al.* [3] a hole was drilled at the midpoint of the SENT specimen. The central part of the specimen configuration used by Semari *et al.* [3] can be appreciated on Figure 21.

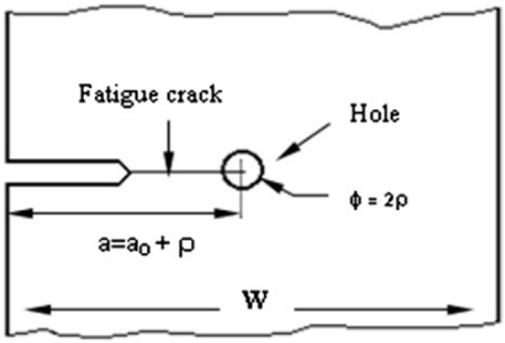

Figure 21. Single edge notch tension specimen configuration reported by Semari et al. [3]

Semari *et al.* [3] proposed a 3D finite element model for which the mechanical properties of the aluminum alloy 6082-T6 were used for the material model, moreover, the kinematic hardening material behavior was also considered within the numerical simulations reported. Semari *et al.* [3] used 8-node solid elements along with symmetry conditions for the proposed 3D model. Besides the 3D model of the aluminum plate, Semari *et al.* [3] also modelled the expander as a rigid ball. The simulation of the cold hole ball expansion was conducted by prescribing displacements to the top of the ball, so it passed through the hole shown on Figure 21. Semari *et al.* [3] also simulated a fatigue test for which a constant amplitude loading with a load ratio of 0.57 was simulated. The estimation

of the stress intensity factors corresponding to the cyclic loading was done by the superposition stresses technique. In the superposition technique first the stress σ_{res} associated to the residual stress field, generated by the cold hole expansion, is calculated, then the σ_{res} is superposed to the stress generated by the external loading σ_{app} to give an effective, or total, stress σ_T. The total stress σ_T is calculated for the corresponding maximum and minimum loads applied to the specimen. The σ_T generates the opening of the crack face and through such displacement a total stress intensity factor K can be estimated and therefore, the total stress intensity factor range ΔK.

Semari *et al.* [3] estimated the fatigue life by the Paris-Erdogan empirical relation for which the C and m coefficients used were determined experimentally for the aluminum alloy 6082-T6 (C=2.7E^{-07} m=3.1) and the ΔK used were those estimated by the superposition method above mentioned.

Additional to the proposed 3D finite element model, Semari *et al.* [3] also conducted an experimental cold hole ball expansion and a fatigue test. The experiment was conducted for the same SENT specimen configuration as the 3D finite element model and with an 8 mm thick plate of Al 6082-T6. A fatigue life enhancement of the specimen due to the cold hole ball expansion was found despite tensile residual stresses were predicted on the entrance and mid planes of the specimen by the 3D finite element model. Regarding the fatigue crack growth rate da/dN as function of the crack length a and the fatigue life (Number of cycles N versus crack length a), good correspondence between numerical simulations and experimental data is reported such as shown on Figure 22(a)-(c). The experimental fatigue crack growth was measured by using a video camera with scale of 0.1 mm.

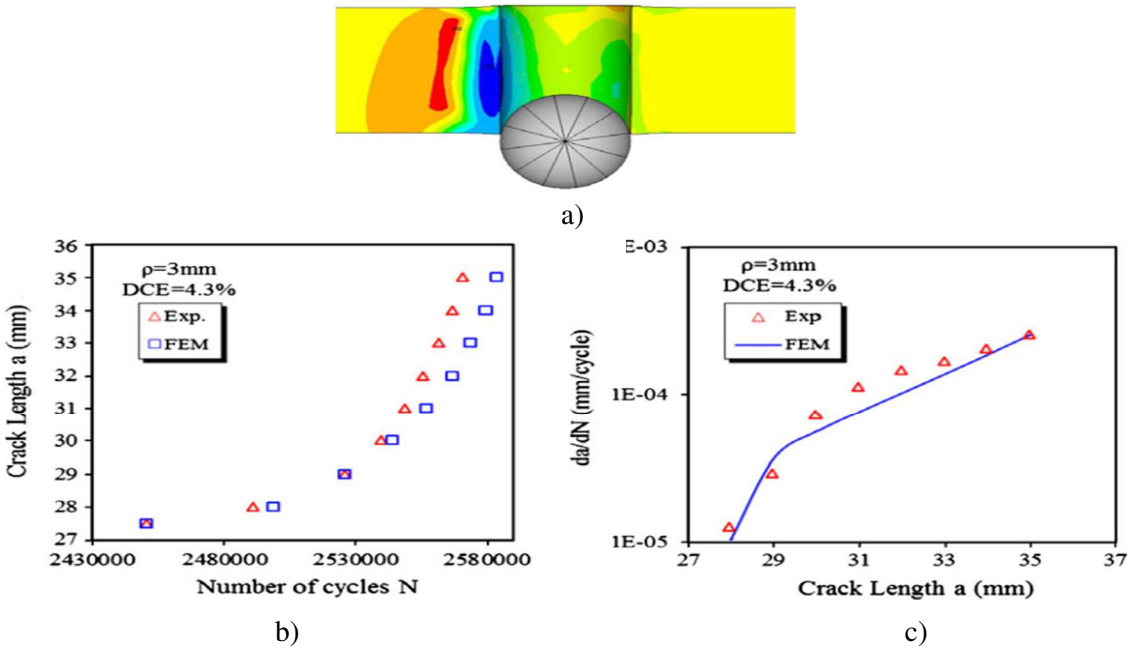

Figure 22. a) Cold hole ball expansion numerical simulation. Comparison for a SENT specimen with 4.3% of expansion b) Fatigue life and c) crack length vs fatigue crack growth rate da/dN [3]

Besides the results shown above [3], there are some other studies reported on the literature that compare numerical results against experimental data in regards to the fatigue life modification in cold hole expanded specimens, such as those divulged by Lacarac *et al.* [36] and Yan-li *et al.* [7].

The former[36] proposed a 2D axisymmetric finite element model through which simulated a cold hole expansion with a 4% of radial interference plus a fatigue test simulation for the cold hole and plain hole conditions.

The 2D finite element model proposed by Lacarac *et al.* [36] simulated the cold hole expansion prescribing displacement to a mandrel such that the mandrel passed through the specimen. The mandrel was modelled as a rigid surface. Lacarac *et al.* [36] considered the mechanical properties of the aluminum alloy 2650 along with the combined hardening behavior for the material model. The study reported by Lacarac *et al.* [37] was performed in the commercial finite element package ABAQUS®. Additionally to the 2D finite element model Lacarac *et al.* [37] also performed an experimental split-sleeve cold hole expansion study to validate the numerical simulations. The experiment were conducted on a 6 mm thick rectangular plate made of aluminum alloy 2560. A hole with a diameter of 6.35 mm was drilled at the midpoint of the specimens. Moreover, an experimental fatigue test were performed considering constant amplitude cyclic loading with load ratios R of -0.5, 0.1 and 0.7 for the expanded specimen as well as for a non-expanded specimen.

Through the cold hole expansion process numerical simulations performed by Lacarac *et al.* [37], a through-thickness variation of residual stress field were predicted. However, such through-thickness variation was not considered for the fatigue simulations, but rather an average residual stress field was considered. The 2D axisymmetrical model did not considered the split-sleeve used in the experimental simulation since such consideration would have required a three-dimensional model, and therefore the computational cost would have increased. The averaged residual stress field generated by the cold hole expansion simulation were considered as an initial condition in a corner-cracked 3D finite element model. For the fatigue simulations, the previously mentioned fatigue conditions used in the experiment were considered. Regarding the crack length *a* as function of the crack growth rate *da/dN* good agreement is reported for the results from the plain hole condition model and the results from the experimental fatigue test of the plain hole condition specimen. On the other hand, the agreement between the results from the fatigue test performed to the cold hole expanded model and the experimental expanded specimen is not as good as for the plain hole condition. Figure 23(a)-(b) shows the results reported by Lacarac *et al.* [36] for the plain and expanded hole condition.

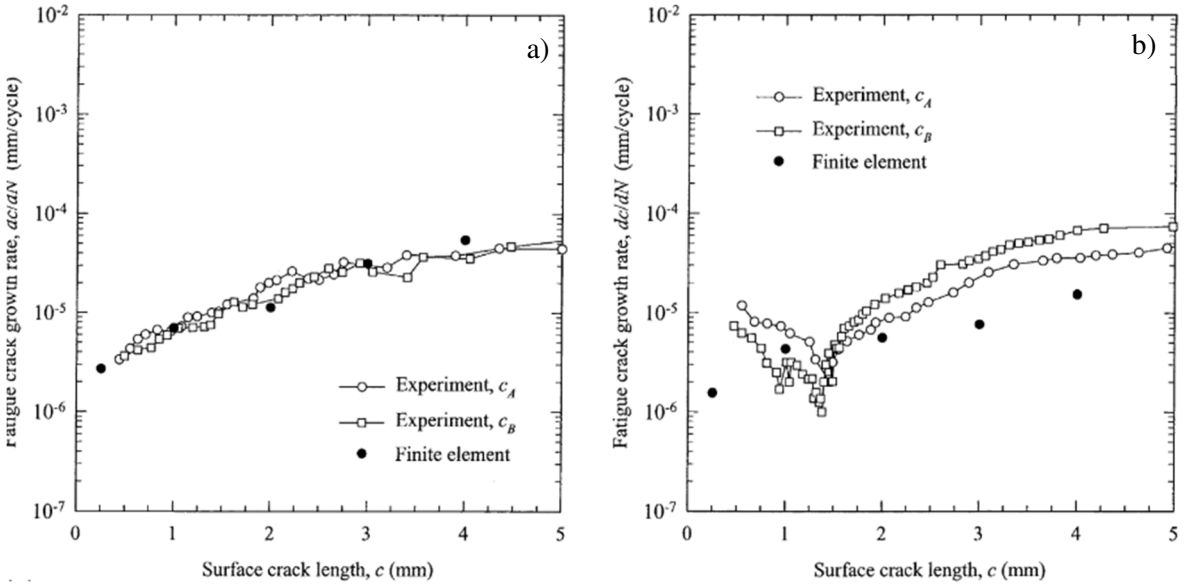

Figure 23. Comparison between numerical and experimental results for crack length a versus fatigue crack growth rate da/dN for a) Plain hole condition b) Cold hole expanded condition.

In the study reported by Yan-li *et al.* [7], a finite element model of a rectangular plate with a hole at the midpoint was proposed. Only one quarter of the plate was modelled due to the symmetry conditions. Yan-li *et al.* [7] used the mechanical properties of the aluminum alloy 6061-T6 for the

material model used on the simulations, besides the kinematic hardening model was utilized. Yan-li *et al.* [7] simulated the split-sleeve cold hole expansion process by modeling a tapered mandrel which was passed through the plate model. The tapered mandrel was modelled such that generated a 4% of radial interference with the plate model. Besides the split-sleeve cold hole expansion simulations, an external loading to the plate model was also simulated. The external loading simulated a maximum load such that induced a 210 MPa stress.

Additional to the numerical simulations performed by Yan-li *et al.* [7], an experimental split-sleeve cold hole expansion and fatigue test was conducted for an identical specimen, regarding the geometry and material. The experimental residual stress was measured by the X-Ray diffraction method and the cracked surfaces were also studied to observe the effect of the split-sleeve cold hole expansion on the specimen's fatigue life. The results from the numerical simulations were compared against the morphology of the fracture surface. Yan-li *et al.* [7] reports that the compressive stress predicted by the numerical simulations coincides with the striation features experimentally found. The fatigue striations are small ridges produced by propagating fatigue cracks, the ridges are perpendicular to the direction of crack propagation [14]. The average striation spacing is often used to represent the fatigue crack growth rate. Much longer striation spacing intervals were found in expanded specimens regarding those with the non-expanded condition. The longer striation spacing intervals represents a higher cycles of fatigue life regarding the non-expanded hole condition.

Although several FEM works have been performed to study the through-thickness residual stress field and fatigue life of cold hole expanded specimens most of them are focused on the split-sleeve methodology while the studies for direct mandrel hole expansion are scarce, moreover the present work has been carried out with the sub modelling technique for which very limited information has been found on the literature [38].

COMPUTATIONAL FATIGUE CRACK GROWTH MODELS

In the present chapter the methodology followed for the computational fatigue crack growth models is presented, such general methodology can be appreciated on Figure 24.

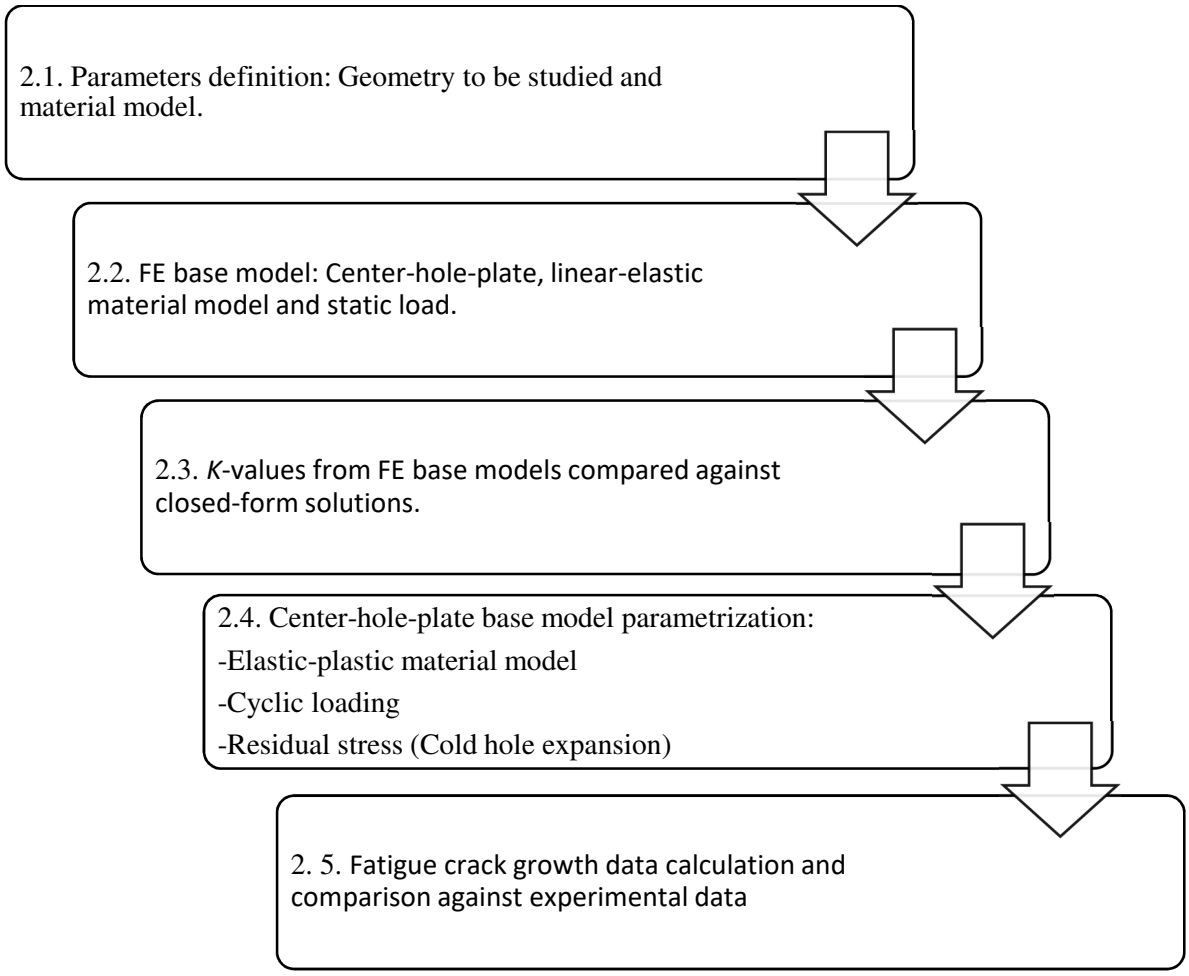

Figure 24. Schematic of the methodology for the fatigue crack growth (FCG) computational model creation.

2.1 PARAMETERS DEFINITION: GEOMETRY TO BE STUDIED AND MATERIAL MODEL

The geometry of the central-hole-plate is schematically shown in Figure 25. The geometry consists of a rectangular plate with the following dimensions:

- Length: 200 mm
- Width: 100 mm
- Thickness: 6.35 mm

Moreover, the plate has a through thickness hole at the midpoint with a radius of 3.175 mm

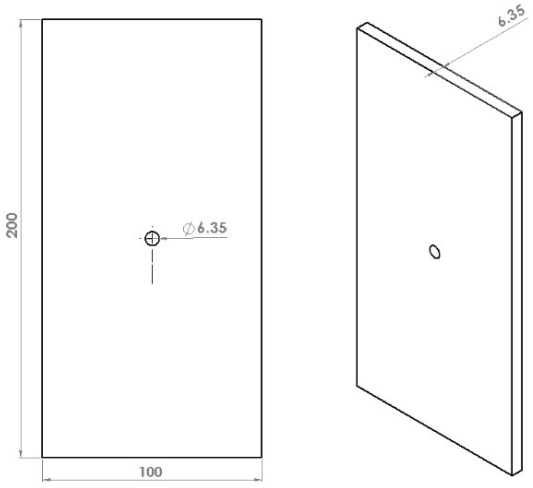

Figure 25. Central-hole-plate specimen

The material considered for the central-hole-plate model show on Figure 25 is aluminum alloy 6061-T6 whose nominal mechanical properties were previously presented on Table 3. Moreover, the elastic-plastic parameters for the aluminum alloy 6061-T6 used were those reported on the literature by Torabi et al. [39]. The elastic-plastic values used for the material model can be consulted on Table 4 and Table 5 presented below on section 2.4 in Table 1. From here on the specimen shown on Figure 25 will be named as the central-hole-plate specimen.

Additional to the center-hole-plate specimen, also a CT-specimen has been studied. The CT-specimen is a parametric standard specimen for fatigue tests which is notched at the half to concentrate the stresses from the cyclic loading. Figure 26 schematically shows a CT-specimen.

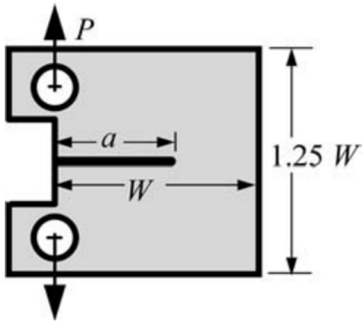

Figure 26. Compact-tension specimen (CT-specimen)

The material considered for the specimen of Figure 26 is, as for the central-hole-plate, aluminum alloy 6061-T6.

2.2 LINEAR-ELASTIC COMPUTATIONAL BASE MODEL

2.2.1 Central-hole-plate model

ABAQUS® finite element package was used to perform the computational model. The loading conditions and the geometry defined in Figure 25, corresponding to the central-hole-plate specimen, are symmetrical, therefore only a quarter of the plate was modelled, and symmetry boundary conditions were used at the XZ and YZ planes.

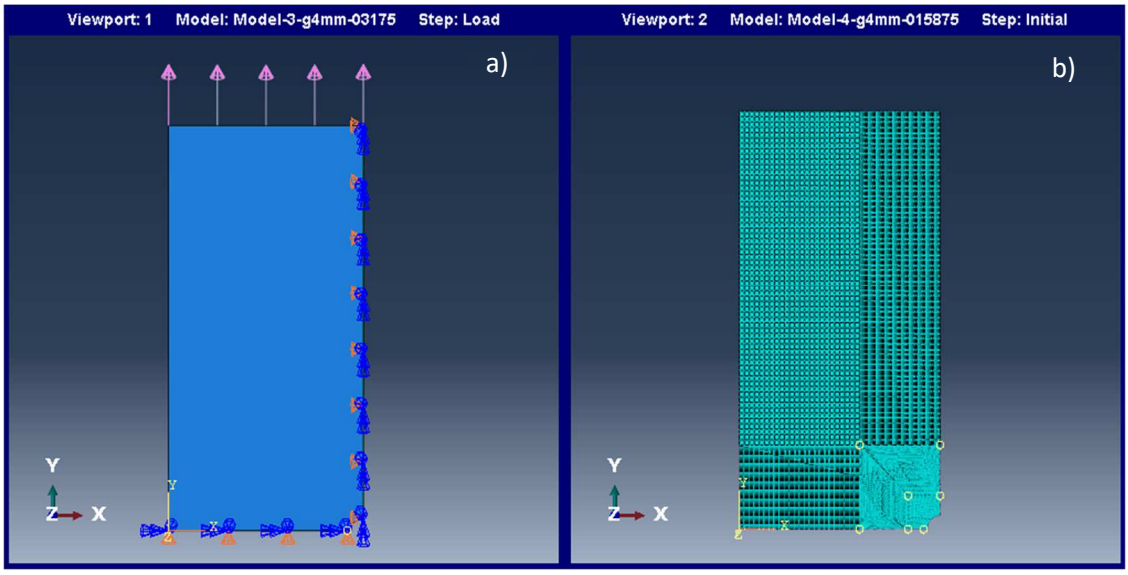

Figure 27. 2D quarter geometry FE model a) Symmetry boundary conditions and remote applied load b) FE mesh

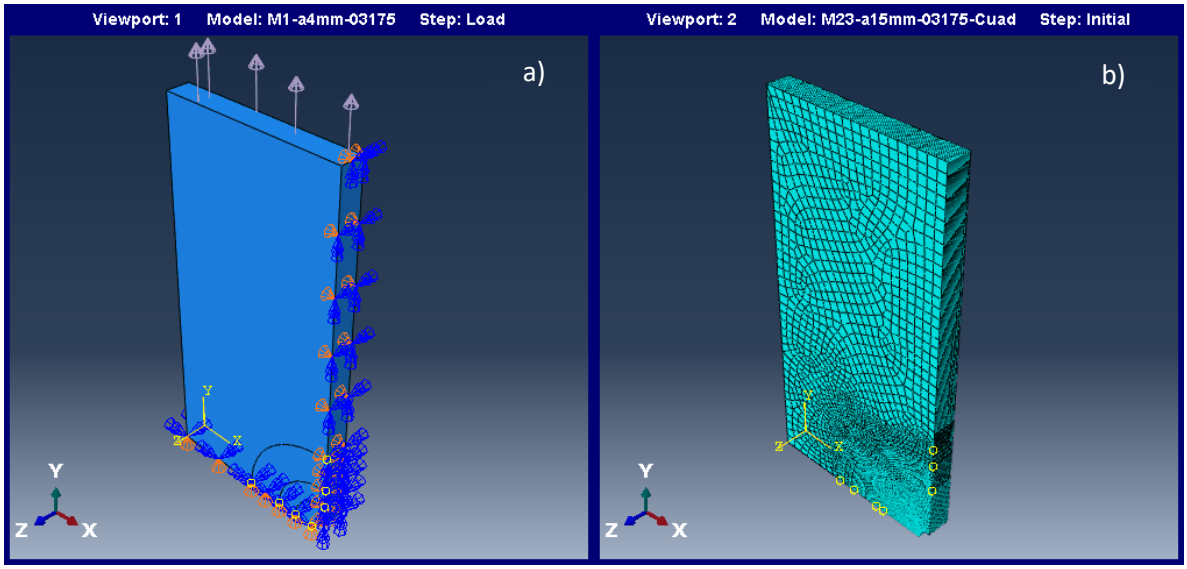

Figure 28. Quarter geometry FE model. a) Symmetry boundary conditions and remote applied load b) FE mesh

For the central-hole-plate FE base model only static loads were considered. The load applied was such that induced 30% of the yield strength for the Al 6061-T6 with a load ratio R of 0.1. The loads were applied to the far end of the plate as shown on Figure 28, such that the loading Mode I was simulated. The central-hole-plate model considered only linear-elastic material behavior. The parameters used in the material model were according to the aluminum alloy 6061-T6, Young's modulus E of 68.9 GPa and Poisson's ratio υ of 0.33. The E modulus and the υ of the model were used along with isotropic material behavior.

The analysis of the central-hole-plate FE base model were divided in two stages. The first stage was a 2D analysis and the second stage was a 3D analysis. For the 2D FE model previously presented on

Figure 27 the analysis were performed basically to establish the meshing strategy as well as the element type and size. The 3D FE model was used to calculate the ΔK-values and then such values were compared against results from closed-form solutions. The central-hole-plate was meshed with 4-node bilinear plane stress quadrilateral elements and 8-node linear brick elements for the 2D and 3D models respectively. The approximate element size for 2D FE model were determined through a convergence analysis using approximate element sizes of 1.058, 0.635, 0.317, 0.158 and 0.079 mm. The results became independent from the mesh at an approximate element size of 0.317 mm, therefore such size was used to perform the 2D simulations as well as the simulations with the 3D FE models. Both models, 2D and 3D simulated through thickness symmetrical radial cracks emanating from the center hole of the plate.

The K-values for the central-hole-plate model were numerically calculated by the displacement correlation method as well as by the contour integral method.

Multiple 3D cracked finite element models were done simulating an initial crack length of 4 mm to a final crack length of 19.5 mm, which based on the plain fracture toughness for the Al-6061-T6 corresponds to the critical crack length.

2.2.2 CT-specimen model

The standardized geometry, as well as the boundary conditions and loads defined on Figure 26, corresponding to the CT-specimen, are symmetrical, therefore only a half of the specimen was modelled, and symmetry boundary conditions were used at the XZ plane. Figure 29 shows the half geometry model, the applied load and its symmetry boundary conditions.

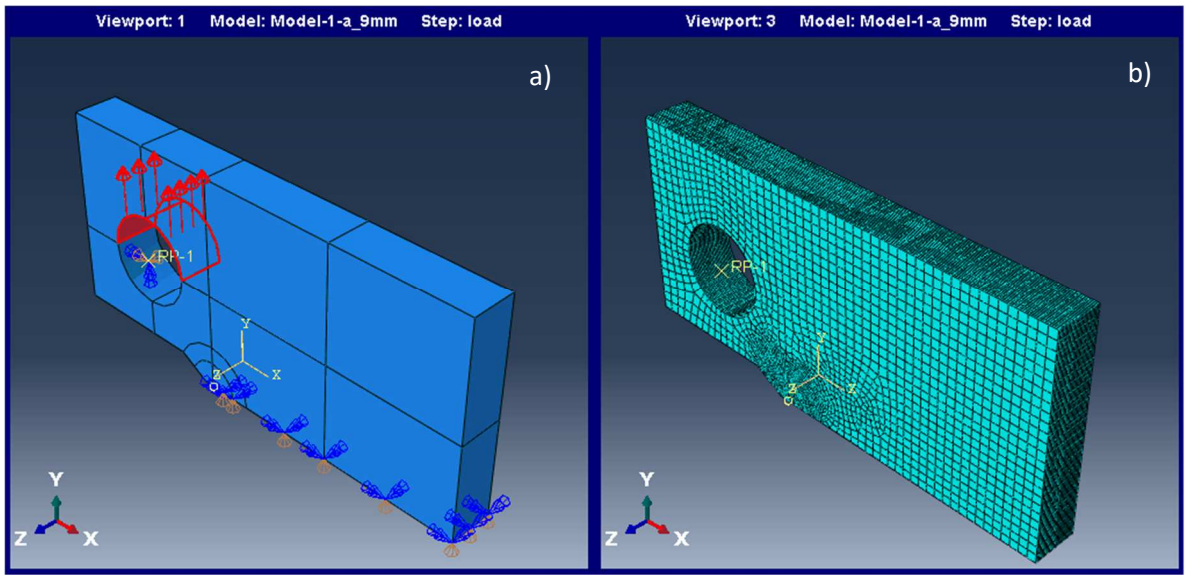

Figure 29. Half CT-specimen geometry FE model. a) Symmetry boundary conditions and applied load b) FE mesh

For the CT-specimen model only static loads were considered. A load ratio R of 0.1 and a maximum load of 2.78 kN and a load range ΔP of 2.5 kN were considered for the simulations. The loads were applied on the upper surface of the hole whose center is marked as RP (Reference Point) such as shown on Figure 29(a)-(b) . Regarding the material model, it remained the same as for the center-hole-plate model. The FE model was used to calculate the stress intensity factors at maximum and minimum applied loads.

The ΔK-values for the CT-specimen model were calculated numerically by the displacement correlation method as well as by the contour integral method.

Multiple 3D CT-specimen cracked models were done simulating an initial crack length of 9 mm to a final crack length of 20 mm, which based on the plain fracture toughness for the Al-6061-T6 corresponds to the critical length.

2.3 LINEAR-ELASTIC COMPUTATIONAL MODEL VALIDATION

2.3.1 Central-hole-plate model

The ΔK-values from the 3D center-hole-plate base model were compared against the results obtained by closed-form solutions reported in the literature. the closed-form solutions reported by Matos *et al.* [17] and Dowling [1], presented in Eq. 11(a)-(b) respectively and Figure 30, were compared among them and against the numerical results for ΔK-values.

$$K = S\sqrt{\pi a}\,\sqrt{1-\gamma}(1 + 0.358\gamma + 1.425\gamma^2 - 1.578\gamma^3 + 2.156\gamma^4) \text{ where } \gamma = \frac{r_h}{a} \quad (11\text{-a})$$

r_h represents the hole radius, *S* the uniform remote applied stress and *a* the crack length from the center of the hole to the crack tip.

$$K = S\sqrt{\pi a}\,0.5\,(3-d)[1 + 1.243(1-d)^3] \quad \text{where } d = \frac{l}{a} \quad (11\text{-b})$$

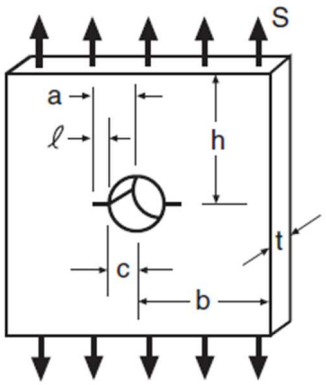

Figure 30. Schematic of characteristic variables used within the closed-form solutions [1]

2.3.1 CT-specimen model

The stress intensity factors *K* at maximum and minimum applied loads were calculated from the CT-specimen model. Such *K*-values were compared against a closed-form solution reported on the literature by Dowling [1]. Equation 12 shows the closed-form solution for the CT-specimen

$$K = \frac{P(2+\alpha)}{BW^{\frac{1}{2}}(1-\alpha)^{\frac{3}{2}}}(0.886 + 4.64\alpha - 13.32\alpha^2 + 14.72\alpha^3 - 5.6\alpha^4) \quad (12)$$

With $\alpha = a/W$

Where *P* is the applied load, *W* the width, *a* the crack length and *B* the specimen thickness (See Figure 26).

Once the *K*-values, and therefore the *ΔK*-values, were calculated and compared against the closed-form solution the corresponding fatigue crack growth rates *da/dN* were computed through the Paris-Erdogan empirical relation. The numerically estimated *da/dN*-values as function of the crack length *a* as well as the fatigue life estimation (number of cycles *N* as function of the crack length *a*) were compared against an experimental study reported on the literature by Ambriz [40].

2.4 CENTRAL-HOLE-PLATE MODEL PARAMETRIZATION

The model parametrization was focused on the following directions:

1. Implementation of the elastic-plastic material behavior and hardening material behavior
2. Constant amplitude cyclic loading
3. Implementation of the residual stress field (Cold hole expansion)

In the following sub sections the above-mentioned directions 1 and 2 are explained while direction 3 is explained in the following chapter 3.

2.4.1 Implementation of elastic-plastic material behavior

To introduce the elastic-plastic material behavior to the model, first an analytical calculus (Eq. 4) of the plasticity zone generated at the tip of a 5 mm crack was done. Then, several convergence analyses were performed to determine the element type and size to be used within the simulations. The analytical plastic zone previously estimated was used as a reference for the convergence analyses. The convergence analyses were performed with approximate element sizes of 0.079, 0.039, 0.019 and 0.01 mm. Moreover, linear and quadratic elements were used within the convergence analyses. The use of 4-node bilinear plane stress quadrilateral elements and 8-node linear brick elements for the 2D and 3D models respectively was defined for the plasticity implementation to the FE model. Besides, the approximate element size of 0.019 mm has been defined for the implementation of the plasticity behavior to the central-hole-plate model, since the results from the convergence analyses, regarding the plasticity zone, turned out to be independent from the mesh at such size (0.019 m).

Regarding the material hardening model, the isotropic, kinematic and combined hardening models were studied. Cyclic loading simulations were performed to understand the differences between the parameters used for the FE models. Though the use of the combined model along with the previously mentioned element type and size were defined for further simulations based on the convergence analyses and the analytical reference of the plasticity zone computed through Eq. 4.

The parameters used within the FE model for the material model were consulted from an experimental stress-strain curve reported on the literature [39]. Besides, various experimental curves reported on the literature were studied [39], [41], [42]. The different stress-strain curves studied that are reported on the literature can be appreciated on Figure 31(a)-(c). As it can be appreciated on Figure 31(a)-(c), the yield strength as well as the ultimate strength can vary from one experiment to another, despite the studied material is the same (Al 6061-T6).

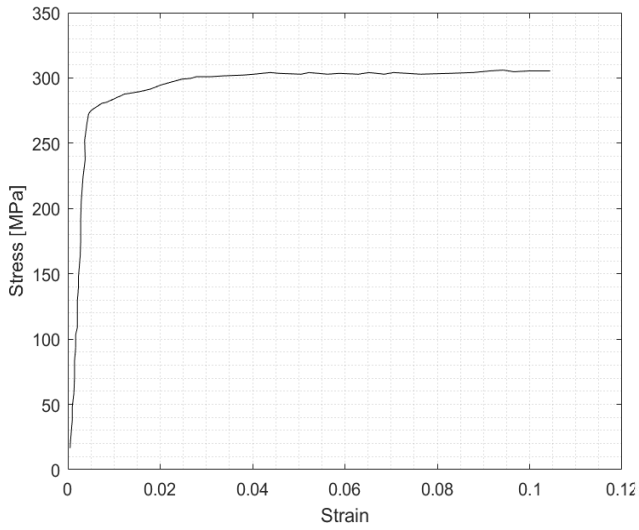

a)

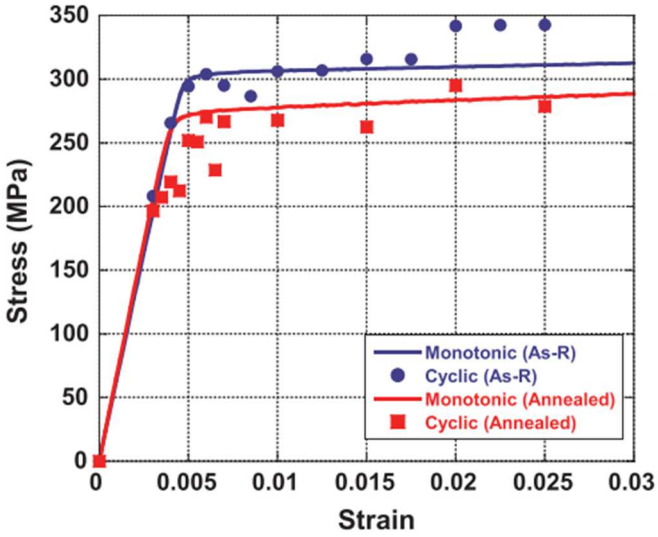

b)

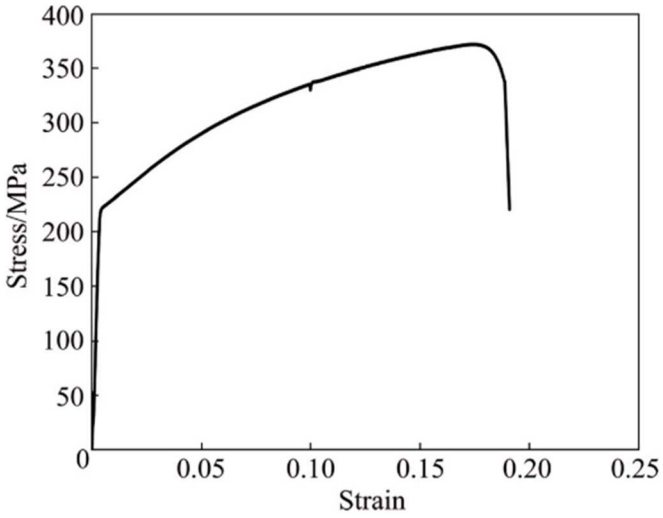

c)

Figure 31. Experimental stress-strain curve reported by a) Torabi et al. [39], b) McCullough et al. [41] and c) Safdarian [42]

Table 4 shows the stress-strain values used to define the material model for the isotropic and combined hardening models, besides Table 5 shows also the specific values used to define the material model when using the kinematic hardening model within the FE model.

Table 4. Material parameters for Al-6061-T6 used for the isotropic and combined FE models

Parameter	Value
σ_0	264.11 MPa
σ_1	269.42 MPa
σ_2	274.15 MPa
σ_3	278.88 MPa
σ_4	281.83 MPa
σ_5	287.74 MPa
σ_6	293.06 MPa
σ_7	296.6 MPa
ε_0^p	0
ε_1^p	0.0005658
ε_2^p	0.001358
ε_3^p	0.0036209
ε_4^p	0.005318
ε_5^p	0.009392
ε_6^p	0.01516
ε_7^p	0.02014

Table 5. Material parameters for Al-6061-T6 used for the kinematic FE model

Parameter	Value
σ_0	264.11 MPa
σ_1	296.6 MPa
ε_0^p	0
ε_1^p	0.02014

2.4.2 Constant amplitude cyclic loading

First, for the central-hole-plate FE model, the simulations of maximum and minimum load were performed independently, i.e. The maximum and minimum loads were prescribed on different simulations. Moreover, cyclic loading simulations were also performed with only linear-elastic material behavior. Then, to introduce the plasticity history within the central-hole-plate FE model, cyclic loading along with the material hardening behavior was implemented to the simulations.

For the present work constant amplitude cyclic loading has been considered. The constant amplitude cyclic loading is characterized by subjecting the component to the same maximum and minimum cyclic loading, as was graphically indicated in Figure 1 at the beginning of section 1. The constant amplitude cyclic loading prescribed to the central-hole-plate model had a maximum load such that induced a 30% of the theoretical yield strength for the Al 6061-T6 with a load ratio R of 0.1. The simulation process consisted on the simulation of a crack by releasing the nodes of the cracked surfaces and then a loading cycle, such process can be schematically appreciated in Figure 32. Besides, test simulations were performed reversing the loading cycle from minimum-maximum load to maximum-minimum load but no differences were found.

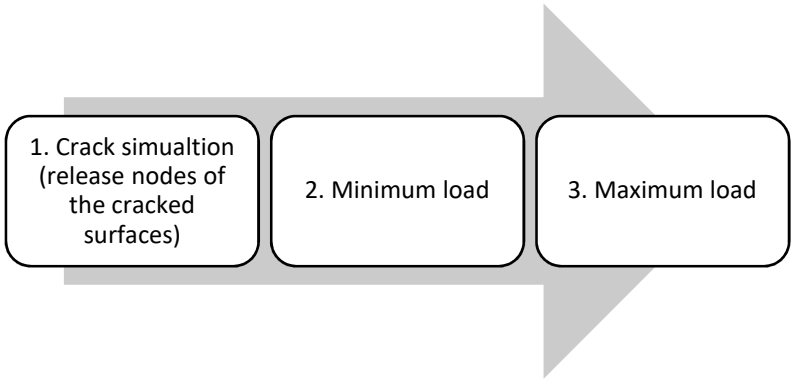

Figure 32. Cyclic loading simulation process

Through-thickness radial cracks were considered for the cyclic loading simulations. The step one shown in Figure 32, "Crack simulation" was done at the beginning of the simulation. The incorporation of the crack was simulated by releasing the nodes located in the cracked surfaces while maintaining the symmetry boundary conditions in the nodes of the rest of the model. The cracked surfaces, as well as the symmetry boundary conditions are shown in Figure 33. Once the incorporation of the crack was done (Step one in Figure 32) the cyclic loading was performed, i.e. The steps two and three shown in Figure 32 were repeated subsequently.

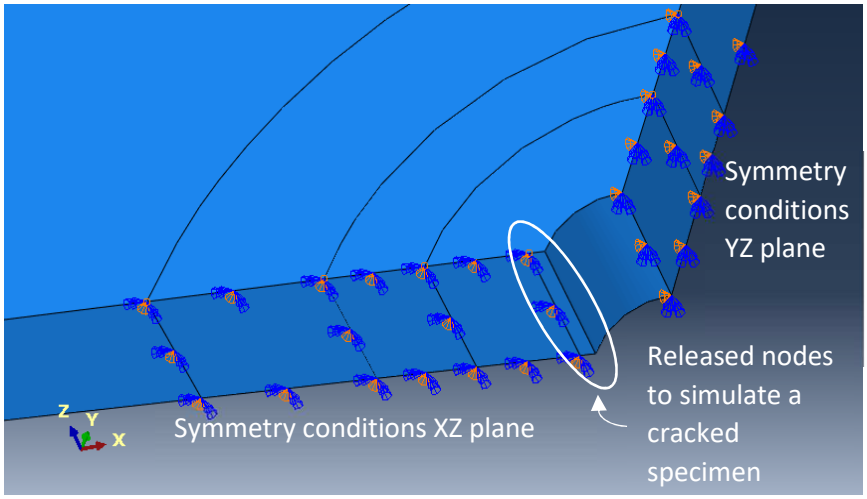

Figure 33. Step one of the cyclic loading simulation process

Simulations of one, five and ten loading cycles were performed for the cracked central-hole-plate FE model. The symmetry boundary conditions shown in Figure 33 Table 4 remained the same for the one, five and ten cyclic loading simulations. Moreover, the cyclic loading simulations were performed for the isotropic, kinematic and combined hardening models. Through the cyclic loading simulations using different hardening material models the corresponding hysteresis curves were generated, so the differences between the three hardening models could be studied.

Besides studying the differences between the three hardening models, *K*-values were calculated for the first, fifth and tenth loading cycle within every simulation. By computing the *K* values at different stages (cycles) of the simulations, a comparison between the *K* values were done regarding the lack of plasticity history (*K* computation at first cycle) or, on the other hand, the consideration of the plasticity history.

2.4.3 Implementation of residual stress

As mentioned on chapter one, the residual stress (RS) has a direct repercussion on accurate fatigue life estimations, therefore precise prediction of the RS field is crucial for the central-hole-plate FE model reported on the present work since it includes the cold hole expansion process simulation as a technique used to induce RS to the mechanical component.

On the present work the introduction of the RS has been implemented to the central-hole-plate FE model by simulating the cold hole expansion throughout direct mandrel expansion process (Figure 12). The sub modelling FE technique was employed to capture the through-thickness RS field on the

central-hole-plate model. The normal reaction force on the mandrel as function of its displacement through the plate thickness was compared against experimental results reported on the literature by Cuevas [43]. The predicted RS field on the central-hole-plate model generated by the cold hole expansion, was considered as the initial state during the following fatigue simulations.

Further details about the cold hole expansion process FE simulations will be given on chapter 3.

2.5 PARAMETRIZED COMPUTATIONAL MODEL: FATIGUE SIMUALTIONS

By the implementation of the elastic-plastic material behavior, the analysis of the constant amplitude cyclic loading and the induction of RS by the cold hole expansion simulations, the central-hole-plate model parametrization was completed, and the FE model was ready to the next stage which was the fatigue crack growth model (FCG model).

For the fatigue FCG model, only six through-thickness crack lengths were chosen to be analyzed. The crack lengths a of 4, 6, 8, 12, 16- and 19-mm were simulated to study their ΔK values and therefore their corresponding fatigue crack growth rates da/dN. The selection of such crack lengths was based on two main factors: first in the cold hole expansion most affected zone and second on the critical crack length according to the plain fracture toughness for the Al-6061-T6. Some studies found on the literature by Yan-Li *et al.* and Gopalakirshna *et al.* [7], [27] have reported that the cold hole expansion most affected zone embraces the material from the hole edge up to 6 mm radially, and beyond such length the effect of the cold hole expansion is minimal regarding the RS field. Moreover, the analysis of only six through-thickness crack lengths was a way to optimize the computational cost of the FE models. It is considered that a FE models optimization is done since the time required to simulate the cold hole expansion and a loading cycle for a crack length was approximately 54 hours plus an approximate memory usage of 6 Gb.

For the computation of the K-values within the parametrized FE model, an analysis between the displacement correlation method and the stress correlation method was performed to determine the optimal method to calculate K. Such analysis studied the equivalency of both correlation methods (displacement and stress) and the factors that may affect the correlation methods such as the boundary conditions of the central-hole-plate parametrized FE model. The stress correlation method was selected to compute K-values from the FE central-hole-plate parametrized model. The selection of the stress correlation method over the displacement correlation method was due to the sensibility of the displacement correlation method to the central-hole boundary condition while the stress correlation method was not sensible to such boundary condition. Moreover, the previous analysis of

constant amplitude cyclic loading showed that not significant differences between the *K*-values computed at the 1st, 5th or 10th cycle could be found, thus, one loading cycle was simulated to compute *K*-values at minimum and maximum load for each of the above through-thickness crack lengths. The *K*-values were determined at the surfaces of the central-hole-plate model and at the mid-plane of the model.

The minimum and maximum loads applied to parametrized FE model were prescribed to simulate the loading mode I to the central-hole-plate model, such as in the FE base model shown in Figure 28. The loading parameters (maximum load and load ratio *R*) were defined according to an experimental study reported on the literature by Cuevas [43].

In order to replicate the study performed by Cuevas [43], first the maximum load applied to the parametrized FE was 49 kN. Considering such load and the effective transverse area of the central-hole-plate, i.e. the area at the middle where the hole can be found, the 49 kN induced 30% of the theoretical yield strength of the Al-6061-T6. A load ratio *R* of 0.1 was considered.

Then, according to the experimental study [43], the 49 kN maximum load was decreased to a 36 kN maximum load, such load adjustment were done based on the experimental 49 kN maximum load results and to ensure that the stress to which the central-hole-plate model is much lower than the yield strength of the Al 6061-T6. The 36 kN maximum load was also simulated on the parametrized FE model as well with *R* of 0.1. Figure 34(a)-(b) shows the servo-hydraulic machine used for the fatigue test as well as the used system to measure the crack lengths.

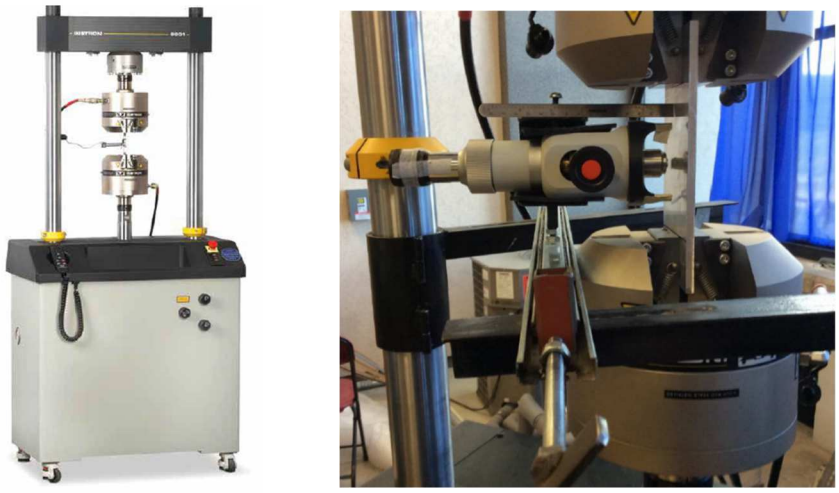

a) b)

Figure 34. a) Servo-hydraulic machine used for the fatigue test of the central-hole-plate specimens and b) Microscope and telescopically system used to measure the crack lengths [43]

Once the *K*-values at minimum and maximum load were calculated from the FE parametrized model, and therefore the ΔK-values, it was possible to determine the fatigue crack growth rates *da/dN* corresponding to the above mentioned through-thickness crack lengths (4, 6, 8, 12, 16- and 19-mm) such *da/dN* values were computed by the Paris-Erdogan empirical relation (Equation 6). Moreover, the *da/dN* calculated from the numerical ΔK-values were compared against an experimental study reported on the literature by Cuevas [43] to verify the effectiveness of the FE parametrized model.

FINITE ELEMENT SIMUALTION FOR COLD HOLE EXPANSION

In the present work the cold hole expansion process by the direct mandrel expansion technique was simulated. The aim of the cold hole expansion is to induce a residual stress (RS) field on the material near the hole of the central-hole-plate model. The RS has a direct repercussion on the fatigue life of mechanical components, it has been demonstrated that tensile RS propitiate the nucleation and propagation of cracks while the compressive RS delay the nucleation and propagation of cracks [3], [4]. The finite element (FE) commercial package ABAQUS® was used to perform all the simulations of the cold hole expansion process.

3.1 MANDREL FE MODEL

As previously mentioned, the process of cold hole expansion consists in passing an oversized mandrel through a hole, such process generate radial interference between the mandrel and the drilled specimen to be expanded. For the present work two mandrel geometries have been modeled, both as 3D analytical rigid bodies, which means that the stiffness of the mandrels is considered as infinite. The expansion tool, i.e. the mandrel, must be made of a much stiffer material than the material of the expanded component to avoid plastic deformations within the mandrel during the expansion. The analytical rigid bodies allows to consider the stiffer condition of the mandrel regarding the central-hole-plate material model, moreover, represents a relatively lower computational cost regarding the use of finite-element-based bodies.

The mandrel geometries studied within the present work were defined as a mandrel completely cylindrical and as a conical mandrel. Figure 35 shows the two mandrel geometries studied. Both mandrels were modelled with a maximum radius of 3.305 mm, so both generated a 4% of radial interference according to Equation 7.

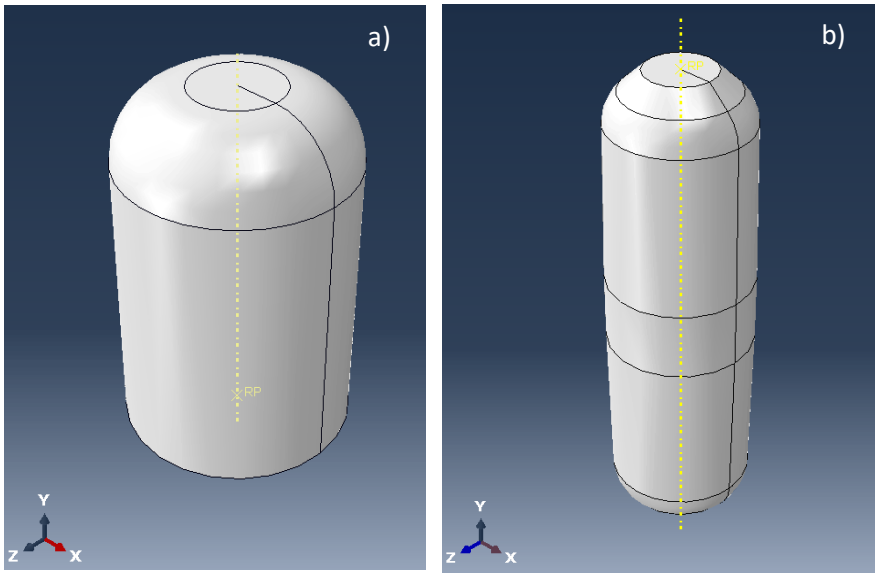

Figure 35. Mandrel geometries modelled a) Cylindrical b) Conical

The mandrel surfaces shown on Figure 35(a)-(b) were defined as the master surfaces while the surface of the central-hole-plate model at which the mandrels establish contact was defined as the slave surface. In a combination of a rigid and a deformable body, the deformable body should be the slave surface while the rigid body should be the master surface. Some penetration of the master surface into the slave surface can be observed. The radial interference between the mandrels and central-hole-plate model can be modelled as a contact pair, which means that two surfaces interact with each other. Besides, the contact pair can be whether node-to-surface contact discretization or surface-to-surface contact discretization. In the node-to surface contact discretization each node within the slave surface interacts with a point on the master surface while in the surface-to-surface contact discretization the interactions are averaged over a region rather than point to point as in the node-to-surface. In general, the surface-to-surface provides more accurate stress and pressure results since in the node-to-surface discretization the forces tend to concentrate in the slave nodes which generates an irregular stress distribution across the studied surface. On the other hand, the surface-to-surface discretization has smooth results due to the averaged penetration resistance among slave and master surface. Thus, for the present work the contact pair with surface-to-surface contact discretization have been defined for the simulations of the cold hole expansion process.

Figure 36 shows the FE model for the cold hole expansion process which consist of the mandrels and the previously shown central-hole-plate model, moreover the corresponding expansion direction (-Z) can be appreciated. The surface of the central-hole-plate model on the XY plane, where the mandrel first stablish contact, was defined as the entrance face while the opposite side was defined as the exit face. As mentioned on previous chapters the central-hole-plate model is symmetric only a quarter of

the specimen was modeled, and boundary symmetry conditions were imposed along the XZ and YZ planes in order to use less computational resources than with the full model. On the other hand, the mandrels were modelled as rigid bodies and no symmetry boundary conditions were considered.

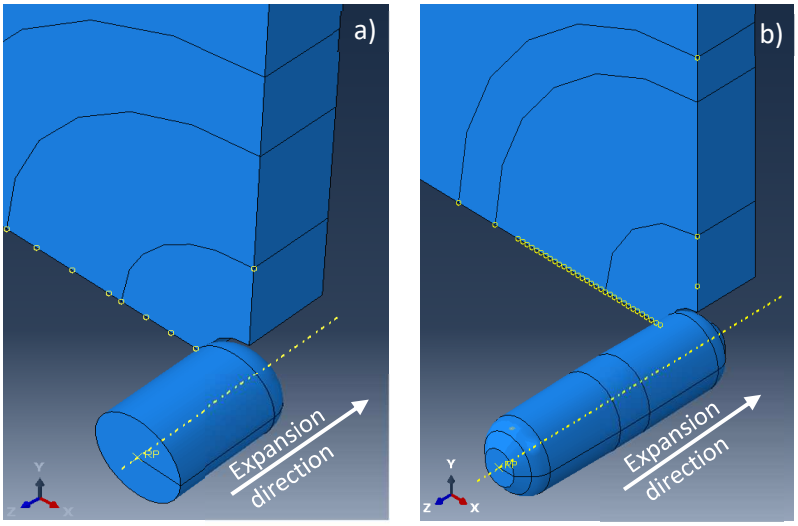

Figure 36. Assembly mandrel-plate a) Cylindrical mandrel b) Conical mandrel

Regarding the boundary conditions for the mandrels, a reference point (RP) was defined within the mandrel's models, as can be appreciated on Figure 36, such RP controls the movement of the whole mandrel. The mandrel's RP were constrained in all their degrees of freedom but on Z direction, which is the expansion direction. Finally, to simulate the cold hole expansion process regular increments of 0.144 mm were prescribed to the corresponding RP of each mandrel to simulate the displacement of the mandrel through the central-hole-plate model.

3.2 CENTRAL-HOLE-PLATE MODEL (SUB MODELLING)

For the prediction of the through-thickness RS field the FE sub modelling technique was used. By the FE sub modelling technique, it is possible to go from the general to the specific. The sub modelling technique consists on the creation of a FE global model (GM) with a relatively coarse mesh and the subsequent creation of sub models (SM) of a localized zone or zones with a refined mesh. The aim of the sub modelling technique is the division of a complex problem into simple localized FE models focused on a smaller part of the problem, moreover, the use of the sub modeling technique allows to optimize the implementation and solution time, especially for 3D models.

Figure *37* shows the scheme of a two-level sub modelling technique; however, since the sub model analysis run as separated model, the sub modelling technique is not restricted to only two-level

analyses and multiple, sequential sub models can be done. The general considerations for the sub modelling technique can be summarized on the following points:

- Run the GM and save the significant results to be transferred to the SM.
- Define a set or sets of driven nodes or surfaces within the SM. The driven nodes or surfaces are those regions within the SM and defined by the user at which the results from the GM are prescribed.
- ABAQUS® does not perform any check of the driven nodes or surfaces within the SM(s), so it is responsibility of the user to correctly define such regions according to the results (stress or displacements) that may be relevant.
- The SM(s) must be situated on the same spatial position where the zone of interest is located within the GM.
- For practicality, the SM(s) should keep the boundary conditions prescribed on the GM. However, such condition is not mandatory within the sub modeling technique and if it is not possible to prescribe the exact same boundary conditions in the SM(s) and GM, the analysis remains valid.

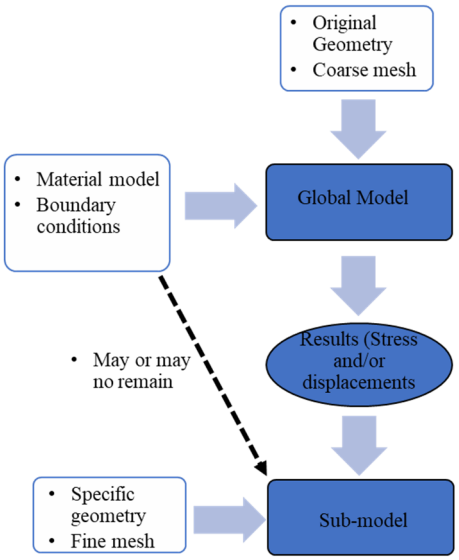

Figure 37. Sub modelling technique scheme

Once the GM and SM(s) have been created the solution of the GM is computed first. Then a region at which the results from the GM will be transferred is defined on the next level SM (driven nodes or surfaces). The results from the GM are transferred to the SM as a boundary condition that can be whether nodal displacements (nodal-based sub modelling) or stress on the finite elements (surface-

based sub modelling). Figure 38 shows an example of the SM surfaces at which the results from the GM have been prescribed as a nodal displacement boundary condition.

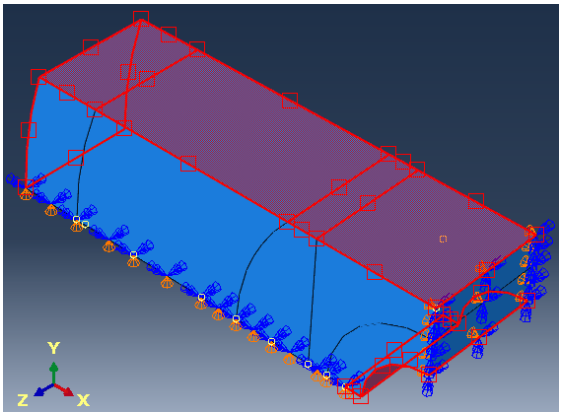

Figure 38. Sub model of a central-hole-plate model. Global model nodal displacements results prescribed at the red regions of the sub model

The nodal-based sub modelling is the more general technique and is recommended when there are not significant variations among the stiffness of the GM and SM as well as for big displacements and rotations. On the other hand, the surface-based sub modelling is recommended for models where the stiffness among GM and SM is considerably different as well as for simulations driven by loads or stresses. However, the combined used of both sub modelling techniques is not restricted.

For the present work a nodal-based three-level sub modelling technique was used, i.e. the analysis started with the creation of a FE global model (GM) then an intermediate FE sub model (I-SM) and finally a fine FE sub model (F-SM). The purpose of the utilization of a three-level sub modelling technique is to generate a smooth transition between the results from GM and the F-SM throughout the utilization of an I-SM. Figure 39 shows a general arrangement for the three-level sub modelling technique. In general, the accuracy of the sub modelling technique can be measured by comparing contour plots among the GM and the sub models. Continuity of the contour plot between the GM and the sub models represents an adequate transition of the results within the FE models.

On the present work, the three levels, GM, I-SM and F-SM represents the central-hole-plate specimen; nevertheless, the FE models differ from each other in certain characteristics. On the following sections the description of each sub modelling level will be detailed.

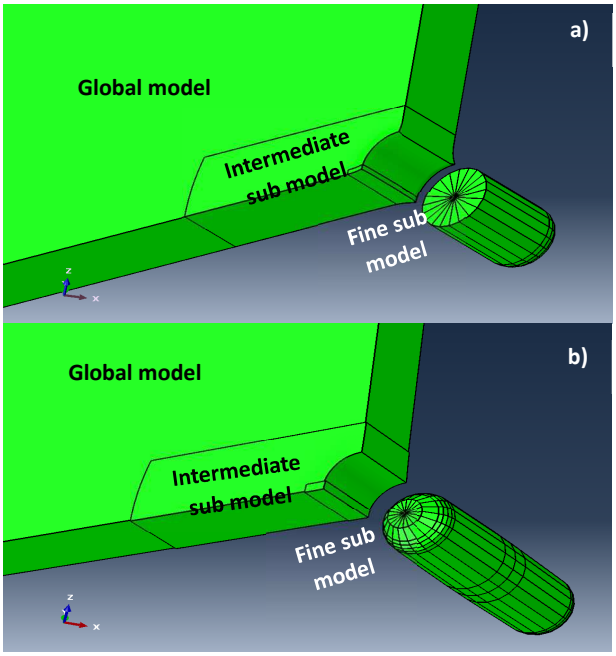

Figure 39. Intermediate and fine sub model's localization within the central-hole-plate global model a) Cylindrical mandrel b) Conical mandrel

3.2.1 Central-hole-plate global model

The finite element global model (FE GM) is the first level to be analyzed within the three-level sub modeling technique and embraces the central-hole-plate as well as the rigid mandrel. Figure 40 shows the FE GM for the cold hole expansion. The central-hole-plate specimen is symmetrical and therefore, for the GM, only a quarter of the plate was modelled. Symmetry conditions were imposed to the GM on the XZ and YZ planes.

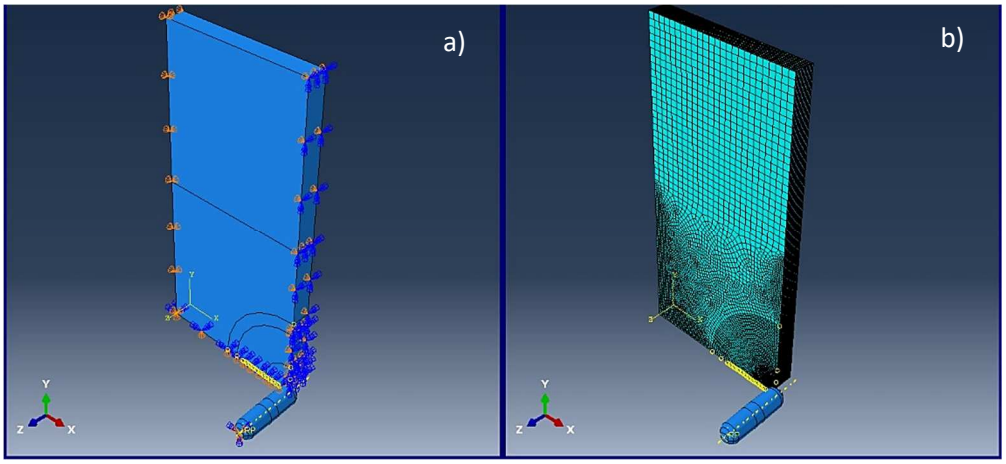

Figure 40. Central-hole-plate global model a) Boundary conditions b) FE mesh

Additional to the symmetry conditions on the central-hole-plate GM, the central-hole-plate GM was constrained in the X axis. The X axis constraint was prescribed to the model YZ face that is not in contact with the mandrel, such condition can be appreciated on Figure 40(a). Besides, the central-hole-plate GM Z axis displacement was also constrained. The Z constraint was imposed to the model entrance face edge corresponding to the border of the central-hole-plate model, this constraint can be also appreciated on Figure 40(a). The X and Z displacement constraints were imposed to replicate the experimental study reported on the literature by Cuevas [43] which is shown on Figure 41.

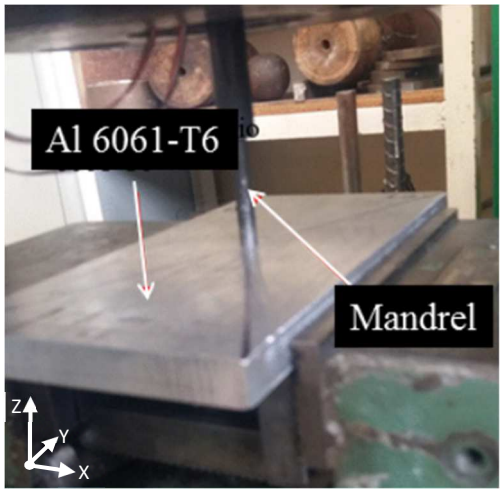

Figure 41. Experimental cold hole expansion [43]

The material model used in the GM was the elastic-plastic behavior with combined hardening model with material properties for the Al-6061-T6; Elastic modulus *E* of 68.9 GPa and Poisson's ratio of 0.33. Regarding the material plastic behavior, the parameters previously reported on Table 4 were used.

The mesh used within the GM was relatively coarse, however the meshing strategy included element size transitions, i.e. the element size near the hole was approximately 0.26 mm and such size were gradually increasing up to an element size of 2 mm for the material far from the hole. The 0.26 mm element size of the GM was determined based on the previous convergence analysis performed for the linear-elastic central-hole-plate FE base model. The convergence analysis probed that the *K*-values were correctly determined with the 0.26 mm element size. The element size transitions can be appreciated on Figure 40(b) and Figure 41 which is a zoom in to appreciate the transitions. The GM used 162000 8-node linear brick elements with reduced integration.

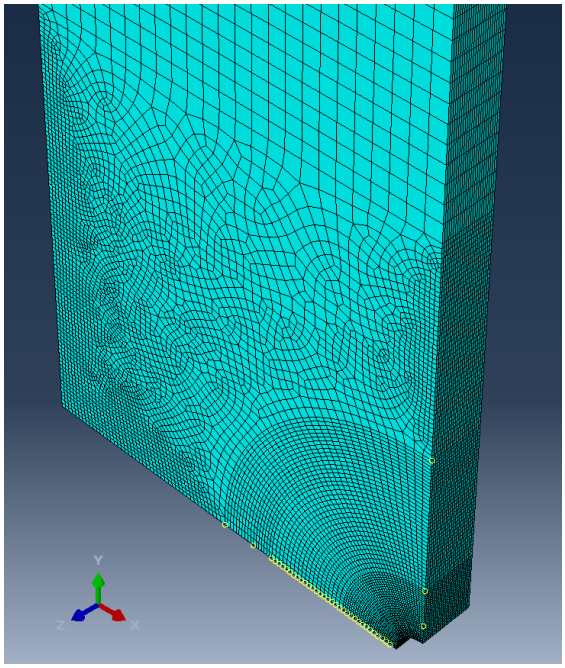

Figure 42. Zoom in to the central-hole-plate model mesh and transitions

The cold hole expansion was simulated by gradually displacing the mandrel model through the central-hole-plate GM. The simulation was performed by 196 steps. A 0.144 mm displacement of the mandrel on the -Z direction was prescribed on each step. The radial interference between mandrel and plate was simulated by a surface-to-surface contact interaction with finite sliding.

The main function of the GM was to capture the displacements generated by the radial interference of the mandrel by the relatively coarse mesh. Then, the nodal displacements were imposed as a boundary condition on the intermediate sub model (I-SM).

3.2.2 Central-hole-plate intermediate model

The central-hole-plate intermediate sub model (I-SM) is the second level of the sub modelling technique reported on the present work. Figure 43 shows the I-SM which only embraces a specific zone of the central-hole-plate model. The I-SM covers from the midpoint of the hole, x=0, up to x = -18.825 mm and the height of the model is from the symmetry plane, y=0, up to y=6.587 mm. The mandrel model is not required anymore since the nodal displacements that generated the radial interference were already captured by the GM. The specific location of the I-SM within the GM can be appreciated on Figure 39.

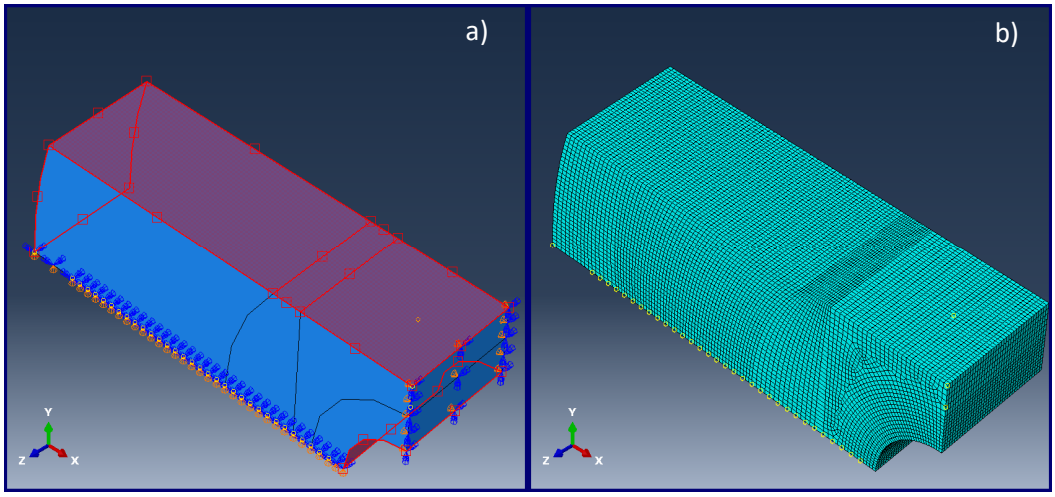

Figure 43. Central-hole-plate intermediate sub model a) Boundary conditions and sub modeled regions b) FE mesh

According to the general considerations for the sub modelling technique, the symmetry boundary conditions imposed on the GM remained on the I-SM. The symmetry boundary conditions that remained from the GM can be appreciated on Figure 43(a) along the lower XZ face and along the right YZ face. Nevertheless, the X and Z displacement constraints imposed on the GM did not remained since the I-SM only represents the material near the hole.

The surfaces highlighted in red on Figure 43(a) represents the surfaces where the sub model driven nodes lie (node-based technique). The nodal displacements generated by the mandrel that were captured by the GM were then imposed as a displacement boundary condition at the sub modelling driven nodes. Therefore, the sub modelling driven nodes acted as the linking zone among the GM and the I-SM.

Figure 43(b) shows the FE mesh used on the I-SM. The mesh used on the I-SM were finer regarding the mesh used on the GM. The approximate element size used within the I-SM was 0.15 mm. The 0.15 mm approximate finite element size used within the I-SM was selected based on the optimization of the computational resources, i.e. leveling the finite element density and the solution time, and considering that the stress gradients presented within the region that the I-SM embraces far from the hole edge were smaller than the critical gradients exhibited near cold hole expanded hole. The I-SM used 131440 8-node linear brick elements with reduced integration.

The amount of FE used on the I-SM, compared against the elements used on the GM, were reduced. Nevertheless, the I-SM volume is approximately 44 times smaller than the GM volume and therefore a much higher elements density can be found on the I-SM. The principal function of the I-SM is to

act as a bridge between the GM and the F-SM, so a smooth transition of the nodal displacement boundary condition can be achieved without loss of accuracy.

3.2.3 Central-hole-plate fine model

The central-hole-plate fine sub model (F-SM) was the third level of the sub modelling technique reported on the present work. The aim of the F-SM is to capture the high stress gradient near the hole due to the cold hole expansion, i.e. the induced residual stress (RS).

Figure 44 shows a F-SM which only embraces a small zone near the hole's edge. The mandrel model is not required in the F-SM since the nodal displacements that generated the radial interference were already captured by the GM, subsequently by the I-SM and now by the F-SM. The localization of the F-SM shown on Figure 44(a)-(b) within the GM and the I-SM can be appreciated on Figure 39.

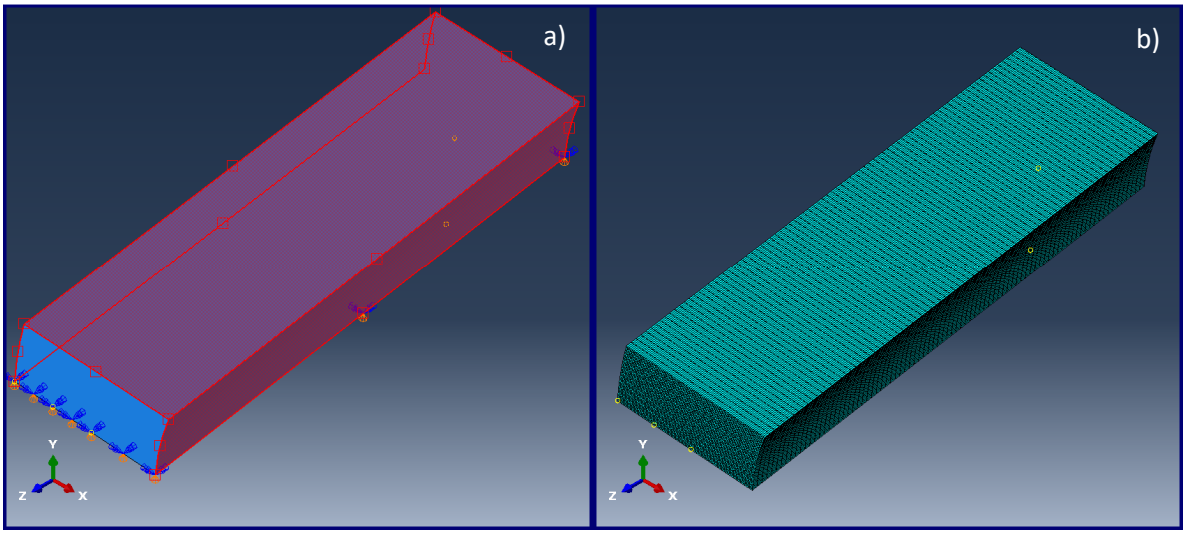

Figure 44. Central-hole-plate fine sub model a) Boundary conditions and sub modeled regions b) FE mesh

According to the general considerations for the sub modelling technique, the symmetry boundary conditions imposed to the GM on the XZ plane were transmitted to the I-SM and subsequently to the F-SM such as shown on Figure 44(a) along the lower XZ face of the model. Nevertheless, neither the YZ symmetry boundary condition nor the X and Z displacement boundary conditions were imposed to the F-SM. Once again, the surfaces highlighted in red on Figure 44(a) represents the linking region among the I-SM and the F-SM, i.e. The driven nodes at which the nodal displacements from the I-SM were transmitted.

The elevated residual stress gradient near the hole were captured by the highly refined mesh of the F-SM shown on Figure 44(b). According to the convergence analyses performed for the implementation of the elastic-plastic material behavior, the approximate finite element size defined for the F-SM was 0.019 mm. The F-SM used 160000 (average) 8-node linear brick elements with reduced integration elements. The amount of FE used within the F-SM was similar to the FE used on the GM, nevertheless the volume of the F-SM is approximately 5520 times smaller than the GM, so a very high FE density can be achieved by the F-SM. Table 6 shows the summary of the FE used on the GM, I-SM and F-SM.

Table 6. Finite element density of the three-level FE sub modelling technique.

Model	**Amount of used FE**	**FE density** $[\frac{FE}{mm^3}]$
Global model (GM)	162000	5
Intermediate sub model (I-SM)	131440	183
Fine sub model (F-SM)	160000 (Average)	27996

Table 6 shows the quantity of FE used within the F-SM as an average. The reason of such condition (averaged) is that not only one F-SM was proposed on the present work since the aim of the sub modeling technique is to study localized or specific zones and according to the information previously reported on section 2.2, *Parametrized Computational Model – Fatigue Simulations*, six through-thickness crack lengths were chosen to be analyzed. The crack lengths *a* of 4, 6, 8, 12, 16- and 19-mm were studied. Therefore, only the fragments of central-hole-plate model that matches with the studied crack lengths regions (4, 6, 8, 12, 16 and 19 mm) worth to have the highest FE density. Moreover, by applying the third level of sub modelling only to the zones of the above-mentioned crack lengths regions (6 different F-SMs) significant savings of computation time and memory have been achieved rather than extending the one single F-SM from the 4 to the 19 mm crack lengths.

To sum up, a F-SM for each crack length region studied in the fatigue simulations was proposed to analyze the residual stress gradient generated by the mandrel's radial interference. Figure 45(a) shows the GM, the I-SM and the distribution of the various F-SM along the symmetry X axis. Figure 45(b) is a zoom to the zone of the three-level sub modelling zone at which multiple F-SM were proposed. Due to the F-SM are related to certain crack lengths regions that were studied in the fatigue

simulations, the name of the F-SM is based on such crack lengths regions. The F-SM-a4 is related to the 4 mm crack region, the F-SM-a6 is related to the 6 mm crack region and so on.

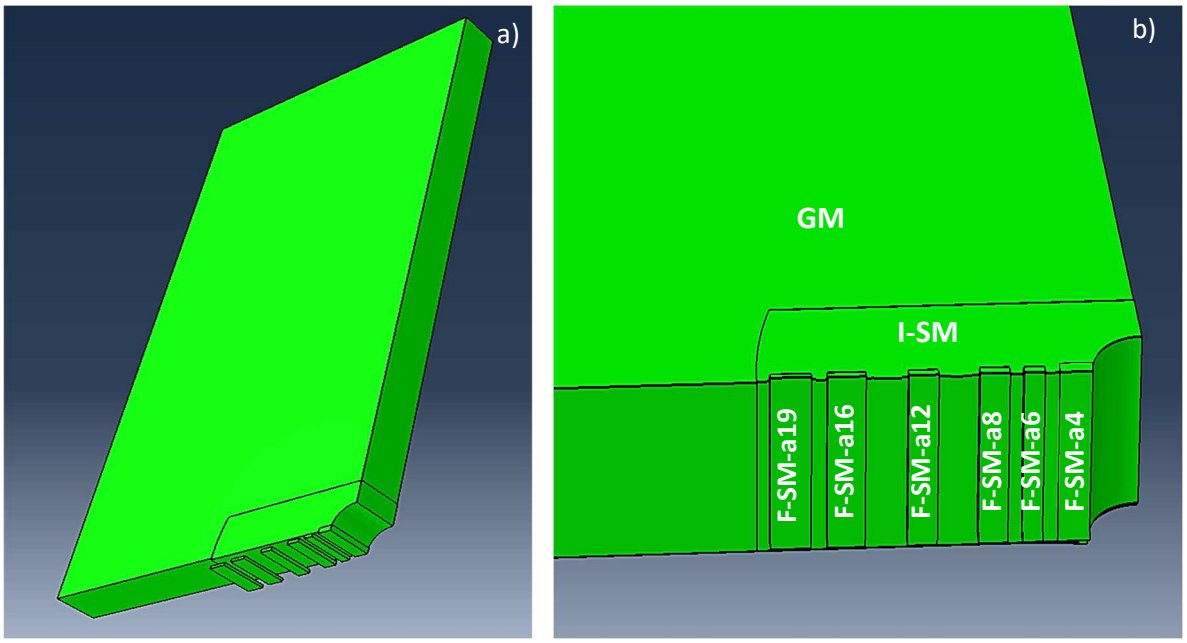

Figure 45. Overlay plot of the three-level sub modelling technique for the central-hole-plate model

3.3 THREE-LEVEL SUB MODELLING RESOLUTION

3.3.1 Residual stress prediction

The residual stress RS component generated during the cold hole expansion, that turned out to be relevant for the present work is the vertical RS component (Y). The vertical RS is the most significant component since such stress component is aligned with the loading mode I. Such loading mode was previously defined for the present work since most of engineering applications are within such loading mode (see Figure 2).

A comparison of the mandrel's reaction force as function of its displacement through the thickness of the central-hole-plate model were done between the two mandrel geometries modelled. Also, the vertical RS component induced on the central-hole-plate model by the two mandrel geometries were compared between them and against an experimental study reported on the literature by Cuevas [43].

Regarding the three-level sub models, a comparison between the RS field captured by the different FE densities presented on the GM, the I-SM and the various F-SM were done. The numerically estimated RS field were measured radially (along the X axis) from the hole edge as well as through the thickness (along the Z axis) of the central-hole-plate model. Specifically, on the entrance face, the mid-plane and the exit face of the central-hole-plate model regarding the expansion direction (See Figure 36).

The results from the central-hole-plate examined planes (entrance face, mid-plane and exit face) were studied to determine the radial extension of the most affected zone by the cold hole expansion. Moreover, the vertical component of the induced RS computed at the three examined planes were compared to define the zone most likely to initiate and propagate cracks.

3.3.2 Fatigue simulations

The RS fields estimated by the three-level sub models were considered as an initial condition for the fatigue simulations. A reliable RS field estimation is vital for an accurate fatigue life estimation, therefore the impact of the three-level sub models' resolution on a cracked and loaded component was studied.

The fatigue cycle simulation process was defined on the previous chapter (See *Figure 32*). The presence of a crack was simulated by defining a crack length, and therefore, a cracked surface within the GM. Such cracked surface can be appreciated on Figure 33. Despite the cracked surface was lying on the symmetry plane XZ it was defined as a surface or region where the displacement was allowed in all its degrees of freedom. On the other hand, the boundary symmetry conditions previously defined on the same symmetry plane XZ remained for the rest of the surfaces. The boundary generated in between the cracked surface region and the symmetry plane was defines as the through thickness crack front.

Once the presence of a crack was simulated on the GM the RS field is redistributed on the released nodes and the ligament. The RS redistribution and the nodal displacements on the cracked surface (released nodes) were captured by the GM and the results of such model were imposed to the I-SM and subsequently to the F-SM as boundary conditions.

The same sub modelling sequence were used for the maximum and minimum loads simulations. The remotely applied loads to the central-hole-plate model were prescribed to the far end of the GM as can be appreciated on Figure 46(a)-(b) simulating the loading mode I.

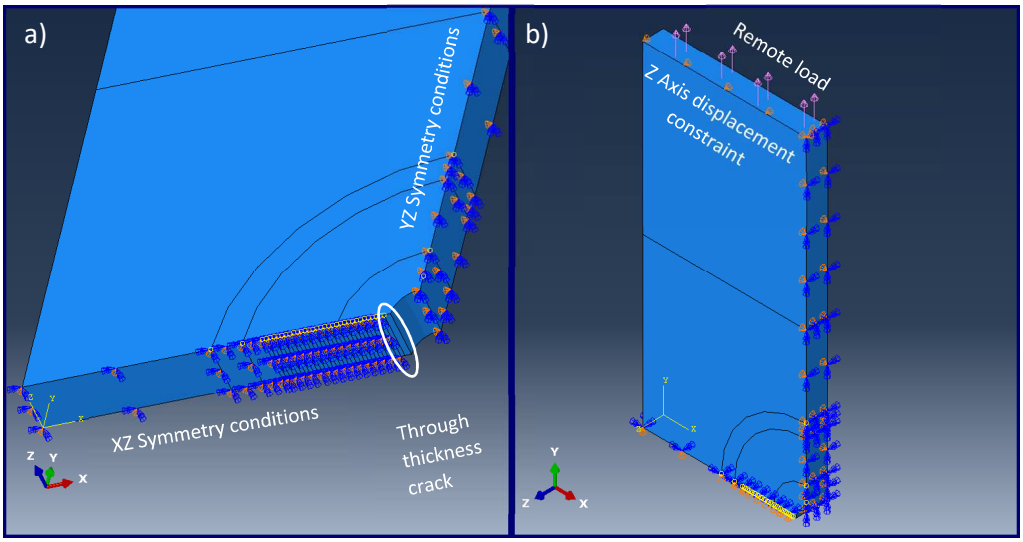

Figure 46. Central-hole-plate global model a) Cracked b) Remotely loaded

The remotely applied loads redistributed the RS field within the component and generated nodal displacements on the cracked surfaces. The RS redistribution as well as the nodal displacements were captured by the three-level sub models by transferring the nodal displacements as boundary conditions among them, such as in the cold hole expansion FE simulations. The combined sequence followed for the cold hole expansion process and the fatigue simulations within the sub modeling technique was done as follows: First simulating the cold hole expansion process on all the three-levels FE models as previously explained (see Figure 37). Then, from the expanded GM, the simulation was restarted with the RS field as initial condition. The presence of a crack as well as a loading cycle were simulated during the GM restarted simulation. The crack as well as the loading cycle simulated during the GM restart simulation generated new nodal displacements, such nodal displacements were then transferred to the expanded I-SM (intermediate sub model) as a boundary condition. The nodal displacement were then captured by the I-SM higher finite element density. Sequentially, the nodal displacements generated within the expanded, cracked and loaded I-SM were prescribed as a new boundary condition to the expanded F-SM. Finally, the results of the expanded, cracked and loaded central-hole-plate model were captured by the highest finite element density within the three-level

sub modeling. Figure 47 shows the hierarchical order in which the fatigue simulations were performed by considering the initial RS condition and the three-level sub modelling technique.

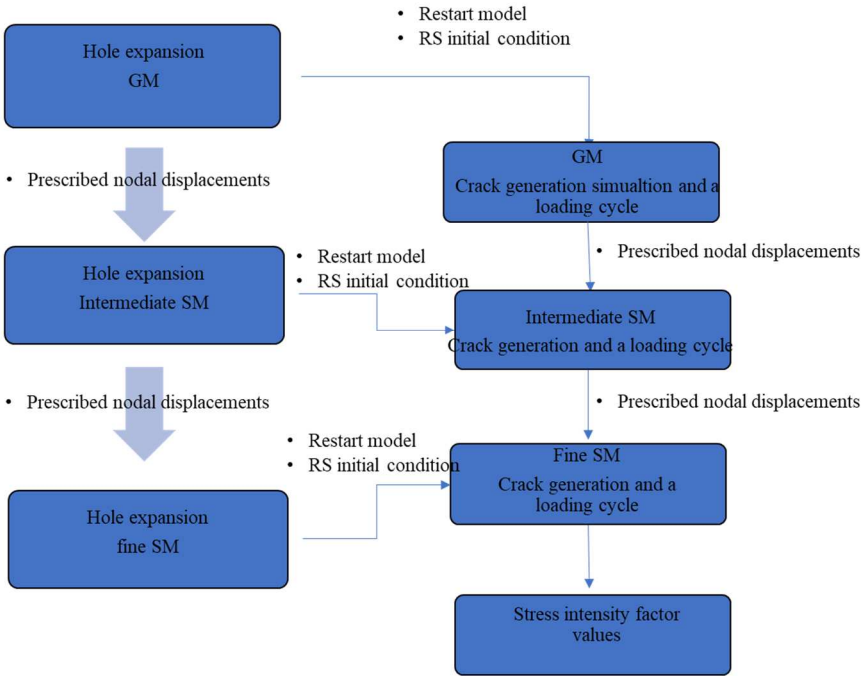

Figure 47. Hierarchical order for the three-level sub modeling within the fatigue crack FE simulations

The stress intensity values (*K*-values) at minimum and maximum loads were numerically computed and used within the Paris-Erdogan empirical relation to predict the corresponding fatigue crack growth rates *da/dN*. A comparison between the *da/dN*-values calculated by the three-level sub models were done to study the impact of the finite element density on the *da/dN* predictions as well as the sub modelling technique effectiveness. The *da/dN* predicted by the model proposed on the present work were compared against experimental data reported on the literature by Cuevas [43].

RESULTS AND DISCUSSION

Within chapter 4 the results of the research will be presented according to the order previously shown in chapter 2. First, the results from the closed-form solutions for the stress intensity factor, second, the linear elastic computational base model results. Third, the results from the displacement correlation method applied to both specimens and finally the results from the central-hole-plate model parametrization.

4.1 CLOSED-FORM SOLUTIONS FOR THE STRESS INTENSITY FACTOR *K* CALCULATION

As previously mentioned on section 2.3.1 on Eq. 11(a)-(b), the closed-form solutions used in the present work were reported on the literature by Dowling [1] and by Matos *et al.* [17].

4.1.1 Central-hole plate specimen

The analytical *K*-values at the maximum and minimum load were estimated for crack lengths from 4 to 19.5 mm by both closed-form solutions and a comparison between the results of both closed-form solutions were done, Figure 48 shows such comparison plus the comparative o the corresponding the ΔK-values. The crack lengths from 4 to 19.5 mm were chosen based on the critical length according to the plane stress closed-form solution. The critical crack length is that at which the *K*-value reach the plain strain fracture toughness K_{IC} for the Al 6061-T6. The maximum load considered for the closed-form solutions was such that induced a 60% of the yield strength for the Al 6061-T6 while for the minimum load it was considered a loading ratio *R* of 0.1.

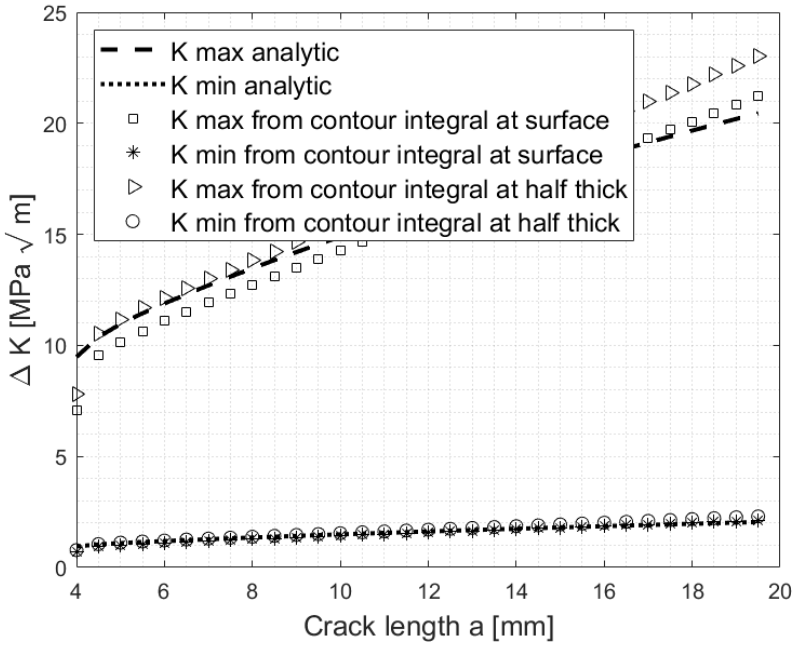

Figure 48. Closed-form solutions comparison for the ΔK values for the maximum and minimum applied loads.

According to the results shown on Figure 48 the differences between the closed-form solutions at the maximum and minimum load were less than 1.2%. Therefore, the differences between the ΔK-values calculated by both closed-form solutions were also negligible. The results calculated by both closed-form solutions were practically the same, thus, it was decided to only use the closed-form solution proposed by Matos *et al.*[17].

4.1.2 Compact tension specimen (CT-specimen)

As previously mentioned on section 2.3.2 on Eq. 12, the closed-form solution to be used in the present work was reported on the literature by [1]. Contrary to the closed-form solutions for the center-hole-plate, in the CT-specimen only one closed form solution was considered. A load range ΔP of 2.5 kN with a load ratio R of 0.1 was considered for the closed-form solution calculus. Contrary to the central-hole-plate specimen, where the K-values were estimated for crack lengths from 4 to 19.5 mm, for the CT-specimen, the analytical K-values at maximum and minimum load were estimated for a minimal crack length of 9 mm to a maximal crack length of 21 mm. The difference between crack lengths calculations among the central-hole-plate specimen and the CT-specimen was because the crack critical length for both geometries is different. For the CT-specimen 21 mm was estimated to be the critical length according to the plane stress closed-form solution, turns out to be the critical crack length. The K-values for the maximum and minimum loads were calculated by the closed-form solution and therefore, the corresponding ΔK-values. Figure 64 shows the results for the ΔK-values as function of the crack length a.

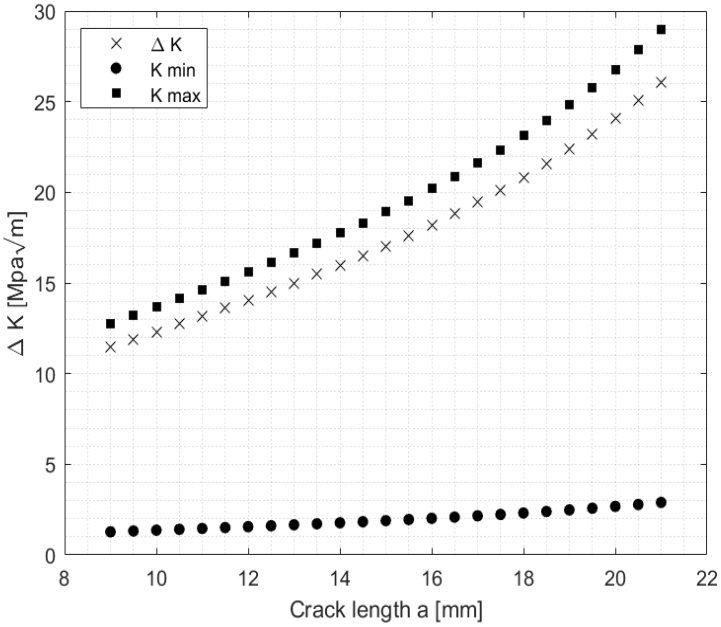

Figure 49.Δ*K*-values as function of the crack length a for a CT-specimen. Δ*K*-values calculated from the closed-form solution reported on the literature.

Once the Δ*K*-values for both, the central-hole-plate specimen as well as the CT-specimen were computed through the corresponding closed-form solutions, a comparative between the behavior of such Δ*K*-values were done. The comparative can be appreciated on Figure 50.

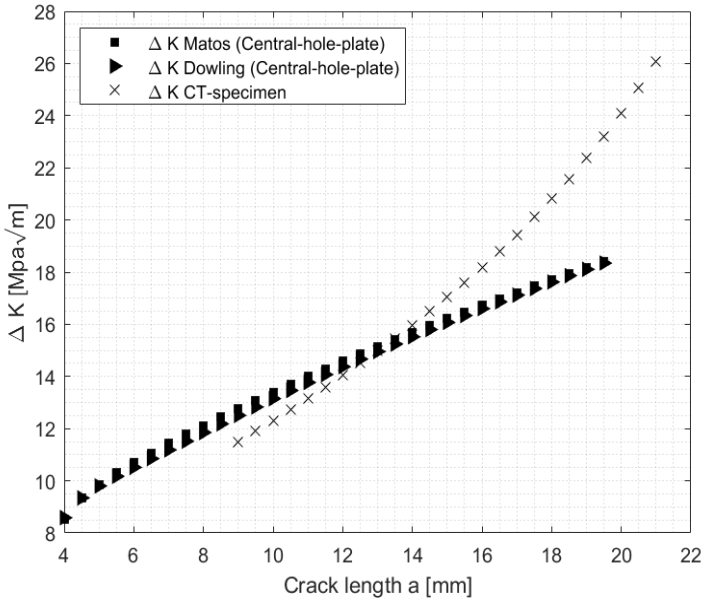

Figure 50. Δ*K*-values for central-hole-plate specimen and CT-specimen through closed-form solutions

As it can be appreciated on Figure 38, the ΔK-values computed for the central-hole-plate specimen are practically the same, despite they were computed by two different closed-form solutions. Regarding the severity for the fatigue crack growth (FCG), the CT-specimen exhibited larger ΔK-values, thus, the central-hole-plate presents a superior resistance against the FCG. Besides, Figure 50 shows the standard behavior of the ΔK-values during the FCG process in a mechanical component.

4.2 LINEAR ELASTIC COMPUTATIONAL BASE MODELS

4.2.1 Central-hole-plate base model

For the linear-elastic central-hole-plate model (Figure 28) the stress intensity factors K were estimated by two methods, the displacement correlation method and the J-contour integral. Moreover, the numerical results were compared against analytical values from the closed-form solution presented by Matos *et al.* [17] .

A 2D analysis were performed prior to the 3D analysis. The 2D models were developed to define meshing strategies and determine adequate element sizes for the problem. A convergence analysis was carried out for the 2D models with different crack lengths and loads.

For the first convergence analysis, a load such that induced the 60% of the nominal yield strength of the Al 6061-T6 were imposed to the far end 2D center-hole-plate model. The first convergence analysis was done for a 7 mm through-thickness crack. The convergence analysis were applied to 2D models with 4-node bilinear plane stress elements, and 3D models with 8-node linear brick elements. The element sizes used were 1.058, 0.635, 0.3175, 0.1587- and 0.079-mm. Figure 51(a)-(d) shows the results for the convergence analysis.

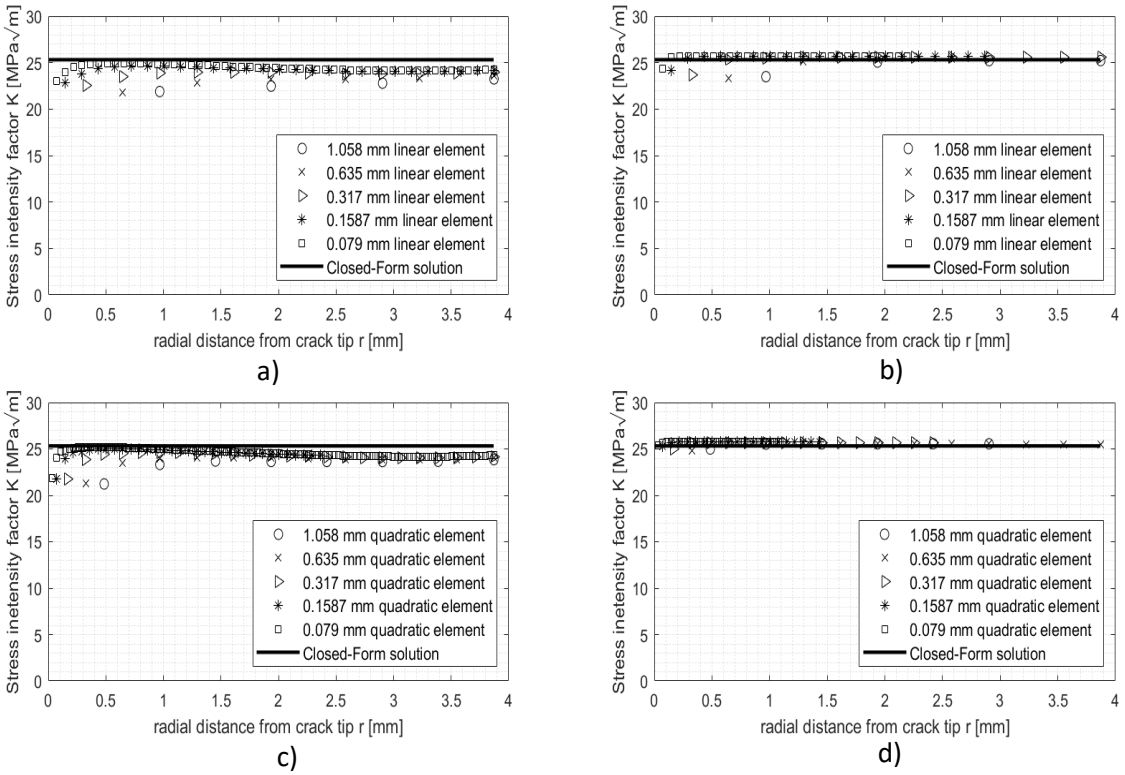

Figure 51. Convergence study results for a 7 mm cracked center-hole-plate model a) *K*-values calculated by the displacement correlation method and linear elements, b) *K*-values calculated by the contour integral and linear elements, c) *K*-values calculated by the displacements correlation method and quadratic elements and d) *K*-values calculated by the contour integral and quadratic elements

Figure 51(a) and (c) shows the *K*-results for the linear and quadratic elements respectively determined by the displacement correlation method. On the contrary to the information reported on the literature (see section 1.3.1 and Figure 8), the numerical results shown on Figure 51 (a) and (c) for the displacement correlation exhibit a non-linear behavior, i.e. after discarding the nodal values near the crack tip not only one slope has been found. Therefore, the extrapolation of the characteristic K-value for the crack tip is not defined. When plotting the *K*-factor with the scale in the independent axis from 0 to 30 $MPa\sqrt{m}$ the non-linear behavior may not be appreciated easily, but when applying a zoom-in to the plots of Figure 51 such behavior turns evident. Figure 52 shows the zoom-in to the corresponding plots of Figure 51. Information about such non-linear behavior has not been found within the literature. This non-linear behavior was further analyzed by a comparison with the CT specimen and the results are presented in the following section.

On the other hand, Figure 51 (b) and (d) shows the results for the *K*-values calculated from the contour integral method with linear and quadratic elements with the independent axis scale also set to 0 to 30

$MPa\sqrt{m}$. As it can be appreciated on Figure 51 (b) and (d), the *K*-values varied slightly between the element sizes of 0.3175, 0.1587 and 0.079 mm regardless the use of linear or quadratic elements. On the contrary the computation time for the quadratic elements was higher than for the linear elements. The zoom-in were also applied to the plots of Figure 51(b)-(d), such close-up can be appreciated on Figure 52. Despite de zoom-in, the non-linear behavior was not found and the difference between the *K*-values estimated by the 0.3175, 0.1587- and 0.079-mm element sizes is less than 1%. Therefore, it can be said that the *K*-values converged at an element size of 0.317 mm. The convergence value has approximately 1.1% of difference regarding the closed-form solution.

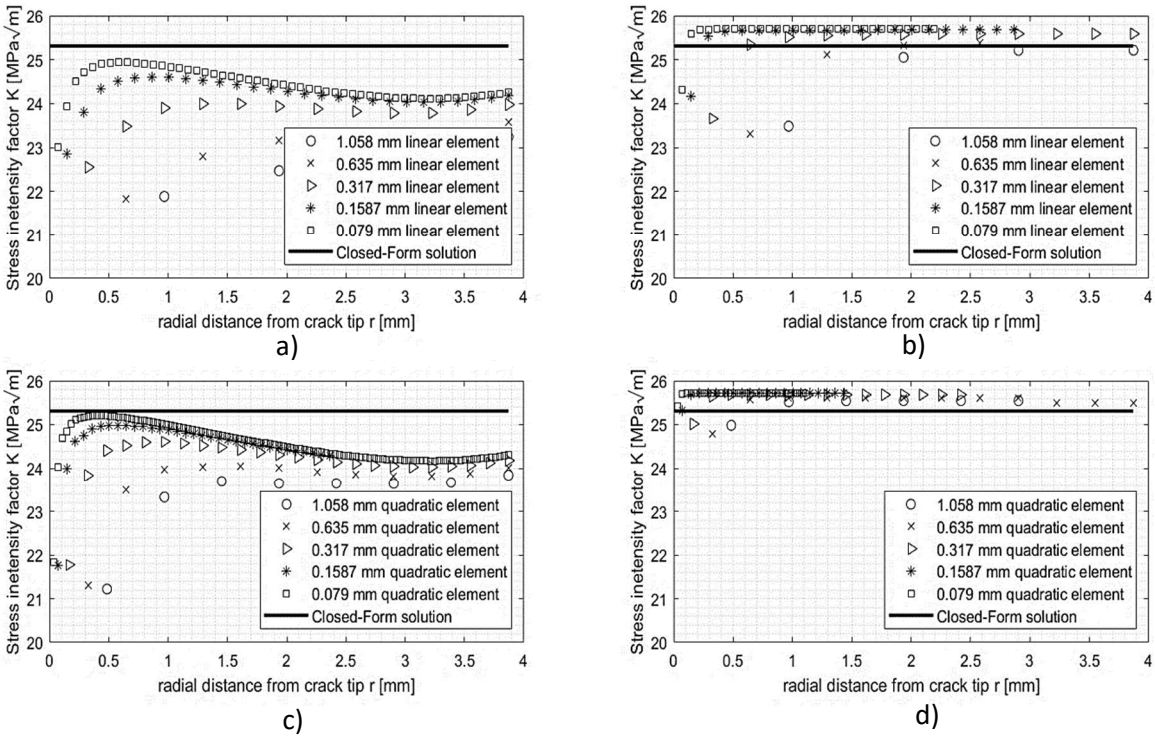

Figure 52. Zoom-in to the convergence study results for a 7 mm cracked center-hole-plate model a) *K*-values calculated by the displacement correlation method and linear elements, b) *K*-values calculated by the contour integral and linear elements, c) *K*-values calculated by the displacements correlation method and quadratic elements and d) *K*-values calculated by the contour integral and quadratic elements

For the second convergence analysis a load such that induced the 30% of the yield strength of the Al 6061-T6 were imposed to the far end of the 2D and 3D models of the center-hole-plate model. The second convergence analysis was done for a 4 mm through-thickness crack and the study evaluated the results of *K*-values calculated by two methods, the displacement correlation method and the contour integral method, the numerical results were also compared against the analytical value from

the closed-form solution presented by Matos et al. [17]. The second convergence analysis were applied to 2D models with 4-node bilinear plane stress elements, and 3D models with 8-node linear brick elements. The element sizes used were 1.058, 0.635, 0.3175- and 0.1587-mm. Figure 69(a)-(d) shows the results for the convergence analysis.

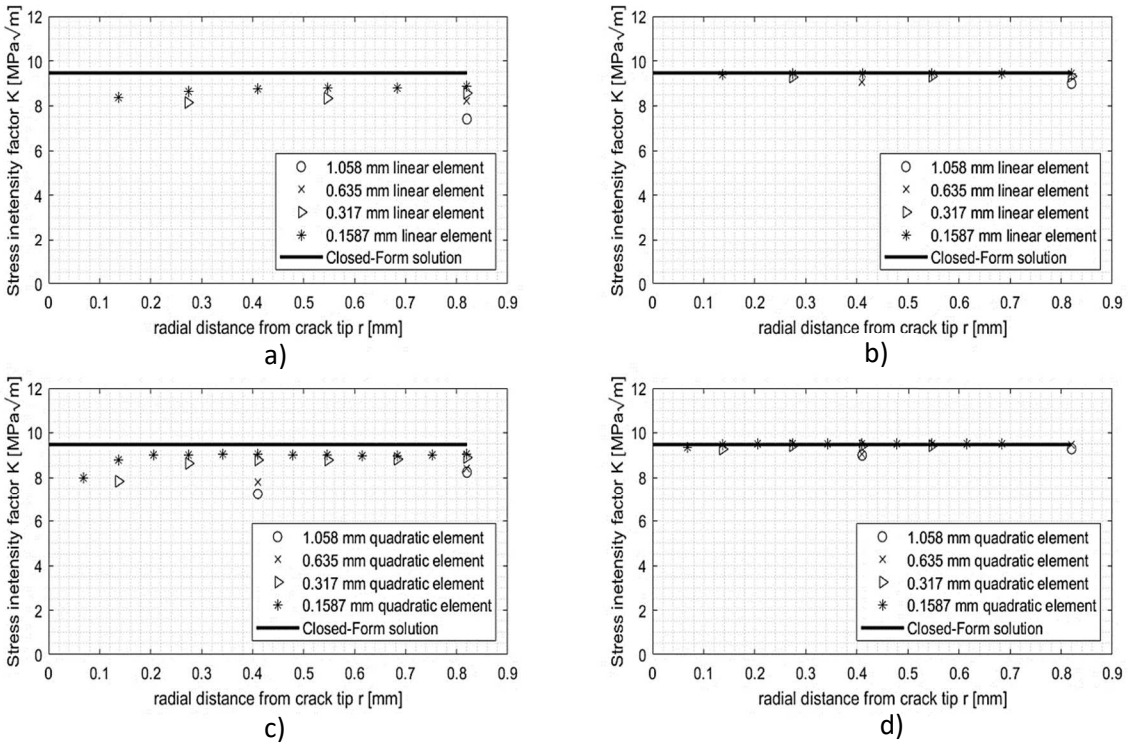

Figure 53. Convergence study results for a 4 mm cracked center-hole-plate model a) *K*-values calculated by the displacement correlation method and linear elements, b) *K*-values calculated by the contour integral and linear elements, c) *K*-values calculated by the displacements correlation method and quadratic elements and d) *K*-values calculated by the contour integral and quadratic elements

Figure 69 (a) and (c) shows the results for the *K*-values for linear and quadratic elements respectively for the displacement correlation method. As in the 7 mm cracked specimen study, the displacement correlation exhibits a non-linear behavior. As in the analysis of the 7 mm cracked specimen, a zoom-in was applied to the plots of Figure 69 to have a better perspective of the non-linear behavior. The zoom in can be appreciated on Figure 54. However, the non-linearity is less evident in this second convergence analysis than in the previous analysis performed to the 7 mm cracked specimen. The non-linear behavior turned out to be less evident in the second convergence analysis since the crack length was smaller and therefore, the finite elements considered for the displacement correlation method were limited, i.e. The finite elements between the crack tip and the model boundary (central

hole) were less, compared with those considered in the 7 mm cracked specimen. The non-linear behavior can be overlooked on the results from the 4-node linear elements (Figure 54a), however the non-linearity turns notorious at the 0.1587 mm element size. On the other hand, the non-linear behavior on the results from the 8-node quadratic elements (Figure 54c), can be appreciated since the 0.3175 mm element size.

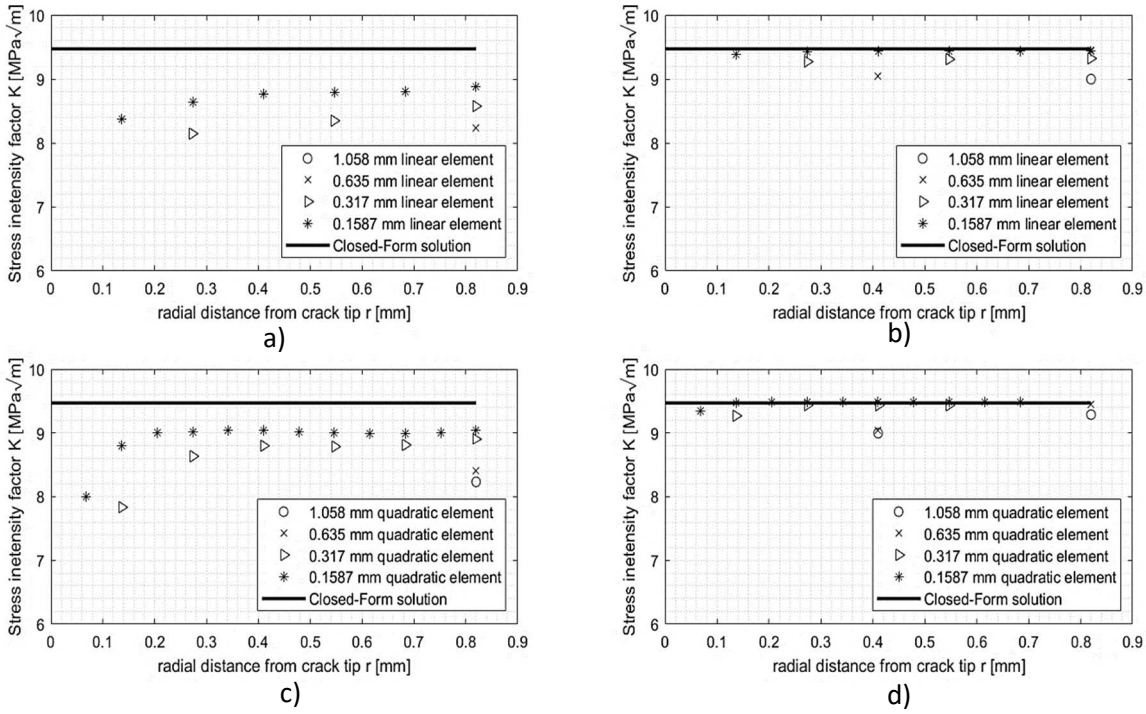

Figure 54. Zoom-in to the convergence study results for a 4 mm cracked center-hole-plate model a) *K*-values calculated by the displacement correlation method and linear elements, b) *K*-values calculated by the contour integral and linear elements, c) *K*-values calculated by the displacements correlation method and quadratic elements and d) *K*-values calculated by the contour integral and quadratic elements

Figure 52 (b) and (d) as well as Figure 54(a) and (d), shows the results for the *K*-values calculated from the contour integral with linear and quadratic elements. Like in the 7 mm cracked specimen convergence study, the *K*-values converged at an approximate element size of 0.3175 mm. The differences between the *K*-values estimated by the 0.3175- and 0.1587-mm element sizes is less than 1.2%. Therefore, it can be said that the *K*-values converged at an element size of 0.317 mm. The convergence values difference regarding the closed-form solution values are approximately 1.6% and 0.4% for the linear and quadratic elements respectively. The convergence analysis in both crack lengths within the central-hole-plate specimen proved that the 0.3175 mm linear finite element is enough for mesh independent results.

From the 2D study, the usage of 0.3175 mm 4-node bilinear plane stress quadrilateral elements with reduced integration were defined for the 3D FE center-hole-plate base model, however for the 3D FE model, the elements became 0.3175 mm 8-node linear brick elements. Moreover, the use of the displacement correlation method was discarded for the 3D FE model due to the non-linear behavior found within the convergence analyses.

Once that the finite element size was set to achieve mesh independent results, the analysis for the 3D case was performed, but on the contrary to the convergence analysis, the *K*-values at maximum and minimum load were calculated for several crack lengths, i.e. For the 3D case the analysis performed was not a convergence analysis but a fatigue crack growth (FCG) analysis. The *K*-values within the 3D central-hole-plate base model were calculated for crack lengths from 4 to 19.5 mm by the contour integral method, moreover, since the FE model is 3D, the *K*-values were studied at the surface of the 3D FE model as well as at the half of the thickness. As previously mentioned, the maximum crack length of 19.5 mm was defined as the critical crack length according to the plain fracture toughness for the Al 6061-T6.

Once the *K*-values at maximum and minimum loads were computed the ΔK-values were calculated and compared against the results from the closed-form solutions reported by Matos *et al*. *Figure 55* shows the behavior and comparison of the *K*-values at minimum and maximum loads from the contour integral, moreover Figure 74 shows the corresponding ΔK-values as function of the crack lengths.

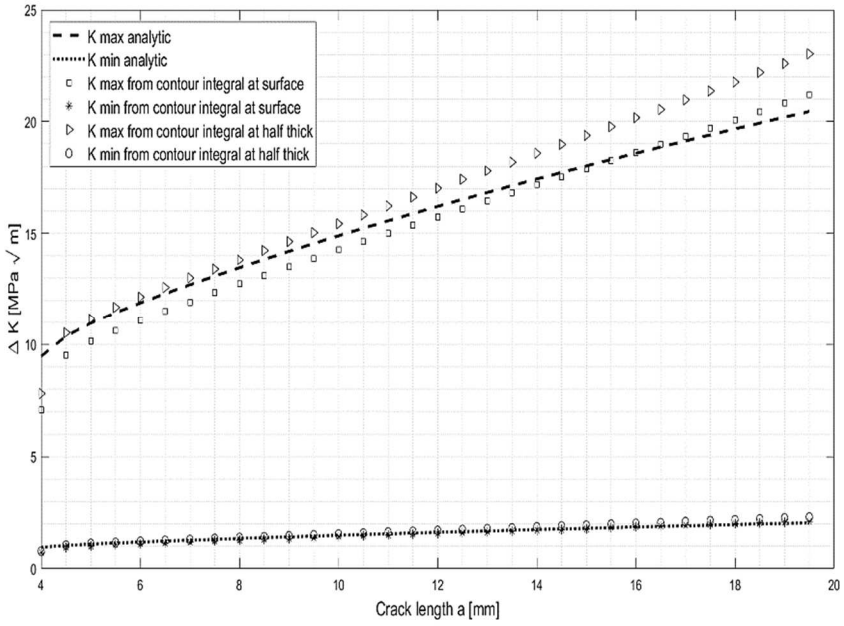

Figure 55. *K*- values at maximum and minimum loads as function of the crack length a for the center-hole-plate linear-elastic model. *K*- values calculated analytically and from the contour integral values.

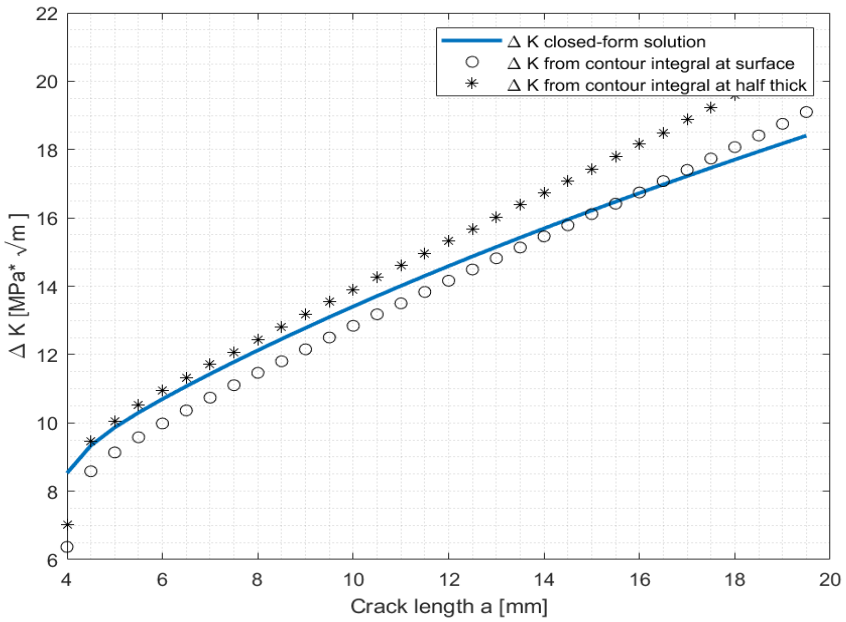

Figure 56. Δ*K*- values as function of the crack length a for the center-hole-plate linear-elastic model. Δ*K*- values calculated analytically and from the contour integral values.

The average discrepancy between the ΔK-values calculated by the FE base model and the results from the closed-form solution, are 3.7% and 5.4% for the results at the surface of the model and at the half of the thickness respectively.

The match of ΔK-values calculated through the 3D FE base model at the surface of the model exhibit a better match with the closed form solution for cracks larger than 14 mm. On the other hand, the results of the ΔK-values calculated at the half of the thickness shows a better match regarding the closed-form solution for cracks up to 10 mm. However, as previously mentioned, the average discrepancy is lightly higher for the results at the half of the thickness. The larger discrepancy within the numerical results at the half of the thickness is attributed to the fact that the closed form solution considered was proposed for plane stress condition and the finite elements at the surface of the 3D FE base model partially replicates the plane stress condition.

The comparison between the numerical (contour integral) and the analytical results also can be appreciated on the fatigue crack growth rates *da/dN* calculated from the FE modal and through the Paris-Erdogan empirical relation (Eq. 7). Figure 57 shows the *da/dN* values as function of the crack length *a* calculated by the contour integral method and by the closed-form solution. For the *da/dN*-values the material coefficients *C* and *m* used were those reported on the literature by Ambriz[40]. Like in the ΔK-values results, the match between *da/dN* numerical results at the surface of the FE base model is better than the *da/dN* numerical results for the half of the thickness regarding the closed-form solution results due to the plane stress condition.

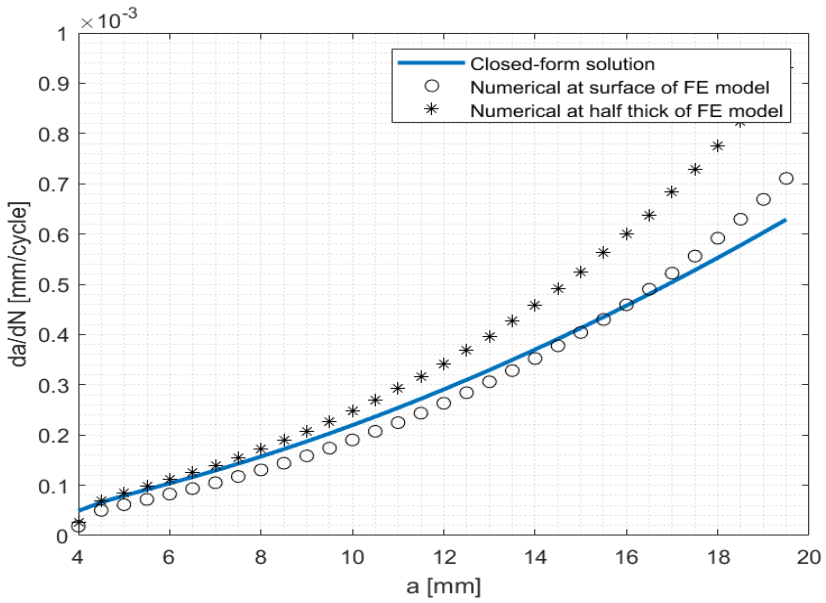

Figure 57. Fatigue crack growth rates *da/dN* as function of the crack length *a* for the center-hole-plate linear-elastic model

4.2.2 Compact tension specimen FE model

K-values from the displacement correlation and contour integral method have also been calculated for the CT-specimen FE model for both, the 2D and the 3D cases. The displacement correlation method as well as the contour integral were previously explained on section *1.3.1 Stress intensity factor evaluation (K-values evaluation)*.

Once *K*-values were calculated for maximum and minimum loads, the corresponding Δ*K*-values were determined. The numerical Δ*K*-values results from the CT-specimen FE model have been compared against a closed-form solution previously presented. Moreover, numerical fatigue life estimations have been compared against experimental results reported in the literature by Ambriz [40].

Like in the previous base model reported on section 4.2.1, a 2D analysis were performed prior the 3D analysis so an adequate finite element size and type could be determined for the 3D simulations.

For the convergence analysis, a load of 2.78 kN were imposed to the 2D CT-specimen FE model, besides, the loading conditions remained the same for study within the 3D CT-specimen FE model. The loads were prescribed on the upper half of the specimen hole, as shown on Figure 26 and Figure 29. The convergence analysis was done for a 10 mm through-thickness crack, according to the crack length measurement schematically shown on Figure 26. The convergence study evaluated the results of *K*-values calculated by the displacement correlation method and the contour integral method

against the analytical value from the closed-form solution. The convergence analysis was done for 1, 0.75, 0.5, 0.25, 0.2, 0.1- and 0.05-mm element sizes as well as for 4-node bilinear plane stress and 8-node quadratic elements. *Figure 58* shows the results for the convergence analysis.

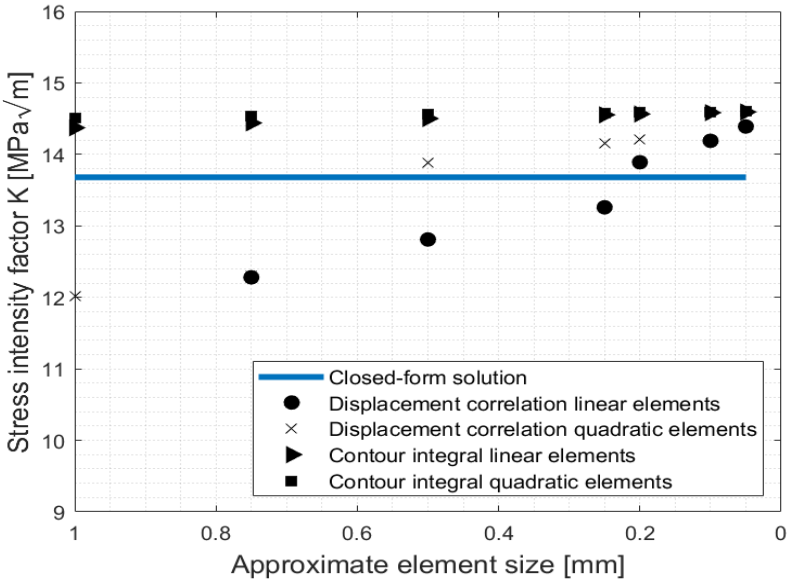

Figure 58. 2D convergence study for a CT-specimen linear-elastic FE model

The results from the contour integral presented on *Figure 58* shows that the *K*-values estimated by the coarsest element size varied slightly regarding the finest element size for both, linear and quadratic elements. In the case of linear elements, the variation between the use of a 1 mm or 0.05 mm element size was of less than 2%. In the case of the quadratic elements, the variation between the use of 1 mm and 0.05 mm element size was of less than 1%. The difference between the *K*-values calculated from the contour integral ($\approx 14.6\,MPa$) regarding to the closed form solution ($13.68\,MPa$) was approximately of 6% for both linear and quadratic elements.

On different circumstances, the *K*-values calculated through the displacement correlation method converged till the 0.1 mm element size. The *K*-values from the displacement correlation method converged at approximately the same value (14.6 MPa) than the *K*-values from the contour integral. By comparing the results shown on Figure 58, it was demonstrated that the use of the contour integral method to calculate the *K*-values provide accurate results with coarser FE meshes, than the use of the displacement correlation method. The results reported on Figure 58, about the advantages of the contour integral over the displacement correlation method, regarding the FE mesh, are in agreement with previously reported results reported on the literature by Courtin et at. [19].

From the 2D study, the usage of 0.1 mm 20-node quadratic brick elements were defined for the 3D CT-specimen FE model. The usage of such size and type of finite elements was defined because through them comparable results for both methods (contour integral and displacement correlation), can be dragged. As in the central-hole-plate model, once that the finite element size was set to achieve mesh independent results, the analysis for the 3D case was performed, but on the contrary to the convergence analysis, the *K*-values at maximum and minimum load were calculated for several crack lengths, i.e. For the 3D case the analysis performed was not a convergence analysis but a fatigue crack growth (FCG) analysis.

K-values at maximum and minimum load were calculated with the 3D CT-specimen FE model. *K*-values were calculated for crack lengths from 9 to 21 mm by the displacement correlation method and by the contour integral method. Moreover, since the FE model is 3D, the *K*-values were studied at the surface of the 3D CT-specimen FE model as well as at the half of the thickness. As previously mentioned, the maximum crack length of 21 mm was defined as the critical crack length according to the plain fracture toughness for the Al 6061-T6.

Once the *K*-values at maximum and minimum loads were computed the Δ*K*-values were calculated and compared against the results from the closed-form solutions previously reported in section 4.1. Figure 77 shows the Δ*K*-values as function of the crack length.

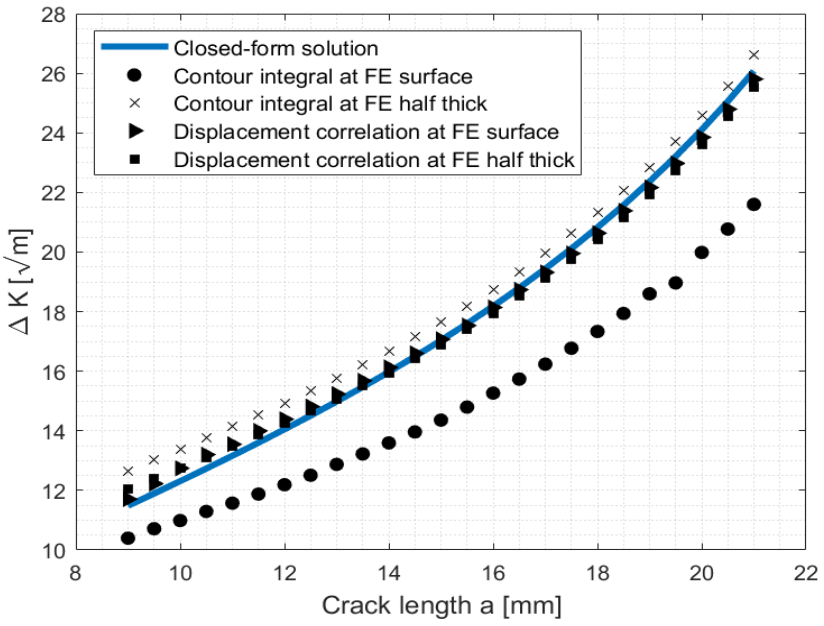

Figure 59. ΔK-*values as fu*nction of the crack length a. *K*-values calculated by various methods throughout a 3D CT-specimen FE model

Results from the displacement correlation:

The average difference between the *K*-values from the displacement correlation method and the *K*-values from the closed-form solution is less than 2% for both locations at the surface or at the half of the thickness of the 3D CT-specimen FE model. However, a slightly better match for the results at the surface of the 3D CT-specimen FE model was exhibited regarding the closed-form solution. The better match of the results at the surface of the 3D CT-specimen FE model is attributed to the fact that the closed-form solution was proposed for a plane stress condition and the finite elements at the surface of the model partially replicates the plane stress condition. Figure 78(a)-(c) shows the results for the vertical displacements at different crack lengths.

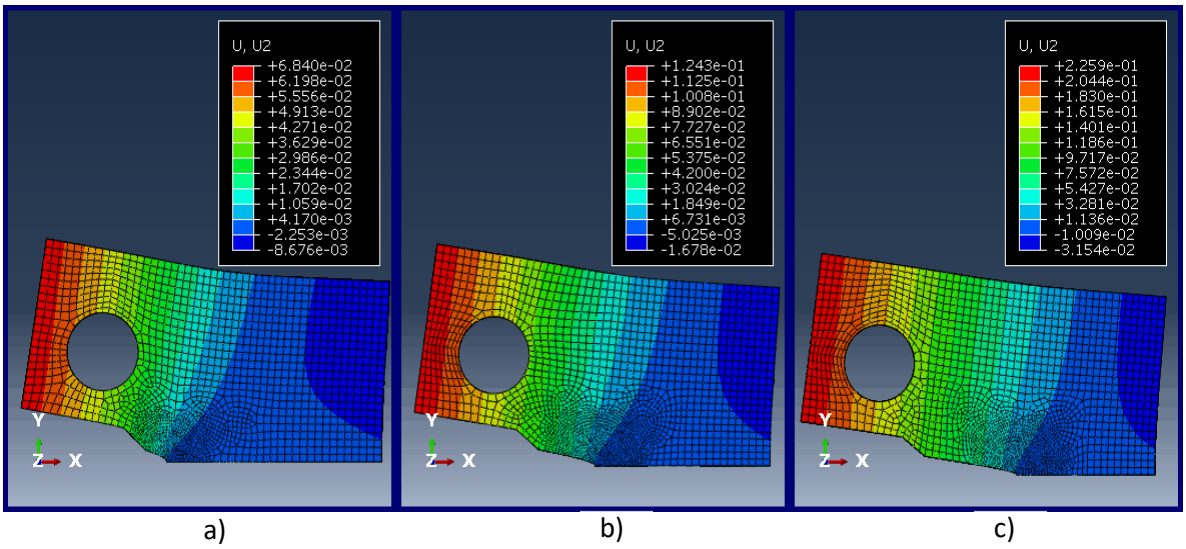

Figure 60. Vertical displacements at maximum load within a cracked CT-specimen FE model a) 11 mm crack b) 16 mm crack and c) 21 mm crack length

Figure 60(a)-(c) shows how the FE model was re meshed from one crack length simulation to another. The finest zone of the FE mesh moved along the X axis as the crack became bigger.

Results from the contour integral:

The average discrepancies between the *K*-values calculated by the contour integral and the *K*-values calculated from the closed-form solution, are 17.4% and 4.3% for the surface and half of the thickness respectively. Unlike the central-hole-plate specimen and the previous displacement correlation results for the 3D CT-specimen FE model, the calculus from the contour integral at the half of the thickness are closer to the closed-form solution than the contour integral results at the surface of the FE model, however the discrepancies are considerable.

The discrepancy among the ΔK-values calculated by various methods (Figure 77 shown above), i.e. closed-form solution, displacement correlation and contour integral, have an effect in the fatigue crack growth rates *da/dN* estimations, and therefore on the fatigue life estimations (Numbre of cycles *N* as function of the crack length *a*). Larger ΔK-values produces larger *da/dN* rates, while in the opposite case. Smaller ΔK-values produces as well smaller *da/dN* rates. Moreover, the higher the estimated *da/dN*-values, the shorter the fatigue life will be and vice versa.

For the *da/dN*-values estimation, the used material coefficients *C* and *m,* $3.97x10^{-8}$ and 3.32 respecitvely, were those reported on the literature by Ambriz [40]. The *da/dN*-values estimated by the CT-specimen FE model and by the closed-form solution were compared against experimental data reported on the literature by Ambriz [40]. Figure 81 shows a comparision among different of *da/dN*-values.

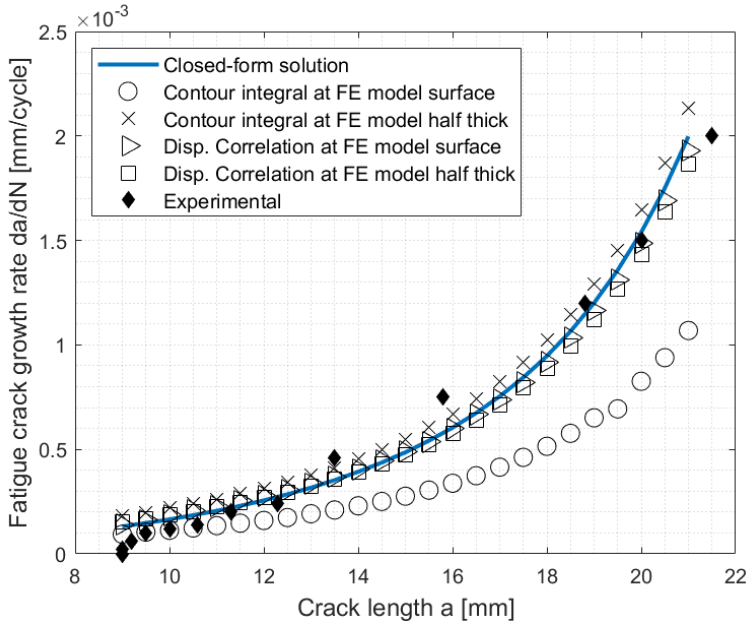

Figure 61. Fatigue crack growth rates *da/dN* as function of crack length *a* calculated by various methods for a CT-Specimen

As it can be appreciated on Figure 81, there are slight differences between the numerical predictions and the experimental results, except for the results estimated at the surface of the 3D CT-specimen FE model through the contour integral method (lowest values).

For crack lengths below 13 mm, the *da/dN* numerical predictions overestimated the experimental values. For intermediate crack lengths (13 to 19 mm) the numerical predictions underestimated the

experimental *da/dN*-values and finally, for cracks between 19 and 21 mm the numerical results approximately match with the experimental *da/dN*-values. Significant discrepancies between the numerical and experimental *da/dN*-values as function of the crack length, have severe repercussions on the fatigue life estimations.

Figure 62 shows a comparison of fatigue life estimated by the different methods used in this research, and as well by the experimental fatigue test reported in the literature.

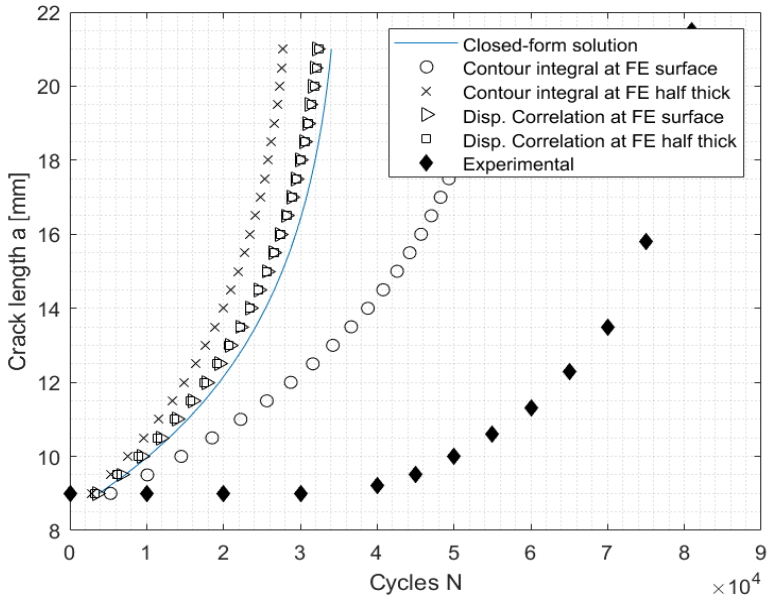

Figure 62. Number of cycles N as function of the crack length *a* for a CT-Specimen.

Figure 62 revealed a notorious underestimation of the fatigue life by the predictions of the finite element simulations and the closed-form solution, regarding the experimental data. The predictions underestimated the fatigue life by an approximate factor of 2.5 except for the results from the contour integral at the surface of the FE model that exhibited the worst correlation with the experimental *da/dN* values. In general, the numerical and closed-form results predicted that fatigue crack length reached 21 mm in the CT-specimen at approximately 31500 cycles, while the same crack length was reached, experimentally, by 81000 cycles.

To discuss the discrepancies among the difference between the experimental and numerical fatigue life estimations, the experimental data reported on the literature by Ambriz [40] were analyzed. In the study performed by Ambriz [40] a pre crack of 1 mm was introduced to the specimens, moreover it

was detected that for the first 3 experimental measurements the crack length *a* remained constant while the number of cycles elapsed was already 20000, i.e. Experimentally, 20000 cycles were required before any fatigue crack growth rate *da/dN* could be detected. In the case of the CT-specimen FE model no pre-cracking cycles were considered. Moreover, to improve the accuracy of the fatigue life estimations an adjustment of the *da/dN*-values was done according to the experimental data based on the material coefficients C and m.

The original *C* and *m* material coefficients, $3.97x10^{-8}$ and 3.32, were coefficeints reported for the whole range of the ΔK-*da/dN* curve as can be appreciated on Figure 63 reported by Ambriz. But considering a single pair of coefficients for the whole range can lead to underestimate or overestimate the fatigue crack growth rates, specially for those values that are farther from the trend line. Sligth variations in the *da/dN*-values can affect severly the fatigue life estimations.

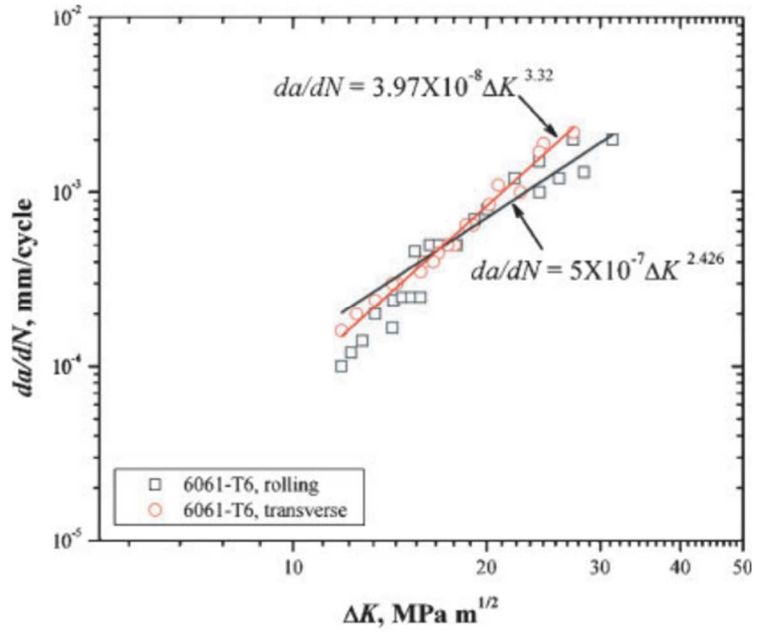

Figure 63. Paris coefficients adjustment reported experimentally by Ambriz [40]

By considering the original *C* and *m* coefficients reported by Ambriz the numerical and analytical fatigue life estimations were very conservative since the numerical and analytical life estimations predicted approximately 30000 cycles to reach the critical crack length of 21 mm while experimentally 81000 cycles were necessary to reach the same crack length. Because of the extremely conservative fatigue life estimations due to the consideration of the original *C* and *m* coefficients. The *da/dN*-values were adjusted.

The methodology to do the *da/dN*-values adjustment is known as a table look-up scheme. The table look-up scheme consists on the usage of experimental FCG data to describe the *da/dN*-values as function of the ΔK-values or vice versa. Contrary to the classical adjustment for the Paris coefficients, such as the reported in Figure 63, where the adjustment is done for the whole range, in the table look-up scheme the adjustment is performed point-to-point. Figure 64(a)-(b) shows the *da/dN*-values values adjusted by the table look-up scheme as function of the crack length and their corresponding adjusted fatigue life estimation.

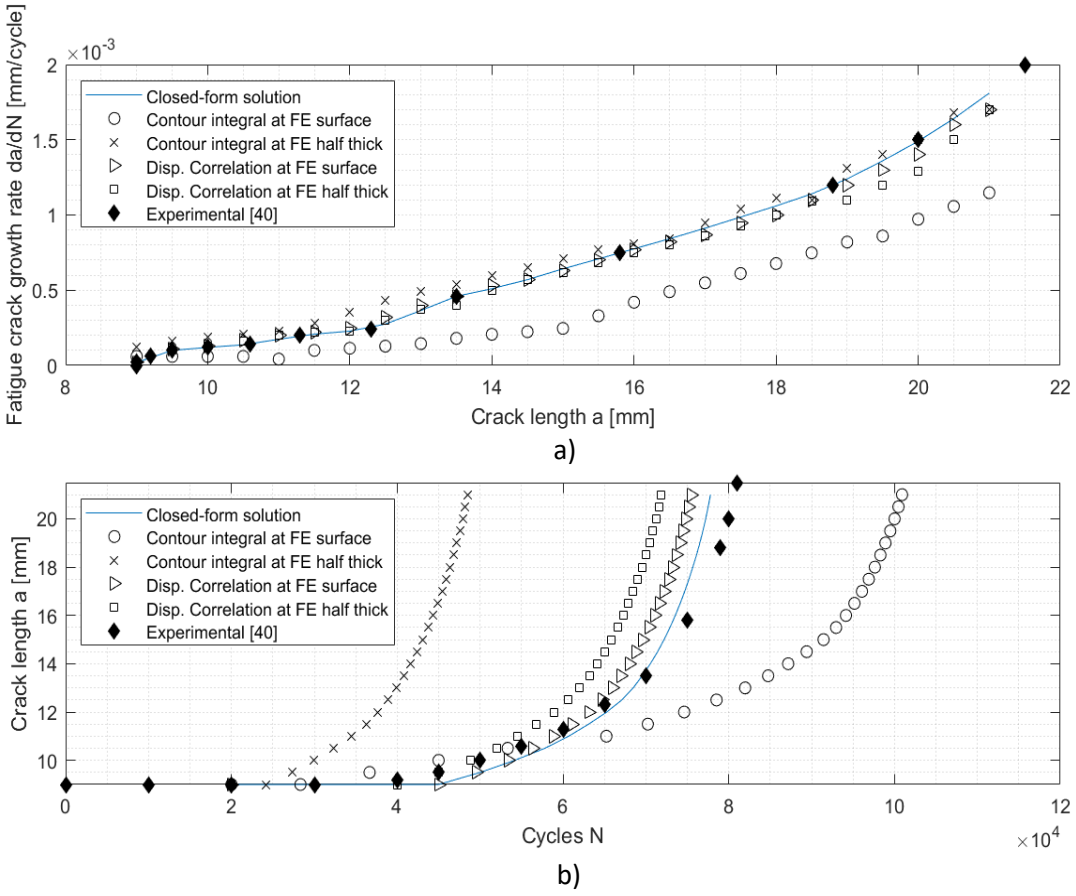

Figure 64. Results from table *da/dN* table look-up scheme for a CT-specimen a) Fatigue crack growth *da/dN* as function of the crack length *a*. b) Fatigue life curves.

Figure 64(a) shows the results from the table look-up scheme for the *da/dN*-values. The results calculated by the contour integral at the surface of the CT-specimen FE model remained at the lowest *da/dN* rates since the less severe ΔK-values (see Figure 59) corresponded to such estimation (surface of the CT-specimen FE model). Contrary, the results calculated by the contour integral at the half of the thickness, remained as the highest rates. On the other hand, the *da/dN* results obtained from the

closed-form solution and the displacement correlation method, for both surface and half thickness, have a maximum average discrepancy of 9% regarding the experimental measurements.

Figure 64(b) shows the fatigue life estimations based on the table look-up scheme *da/dN*-values, Figure 64(a). The less conservative fatigue life prediction was done by the results from the contour integral at the surface of the CT-specimen FE model. The estimation of the contour integral at the surface predicted approximately 100900 cycles to reach the 21 mm crack length while the experimental cycles to reach the same length were 81000 cycles. All the analytical and numerical results for the fatigue life estimations were compared against the experimental fatigue life, i.e. The 81000 cycles elapsed to reach the 21 mm critical fatigue crack length.

On different circumstances, the most conservative estimation was done by the results from the contour integral at the half of the thickness, which predicted an approximate of 49000 cycles to reach the 21 mm critical fatigue crack length.

Differently, the fatigue life estimation from the closed-form results and from the displacement correlation at the surface and half of the thickness of the CT-specimen FE model shows a much better match against the experimental measurements.

The fatigue life estimation from the results of the displacement correlation method at the surface of the CT-specimen FE model, predicted a total of 75450 cycles to reach the 21 mm crack length, while the results at half of the thickness, predicted 71860 cycles to reach the same 21 mm crack length. In other words, through the 3D CT-specimen FE model along with the use of the displacement correlation method fatigue life predictions of approximately 91% of accuracy regarding experimental data were achieved. Moreover, 96% accurate fatigue life estimation was achieved from the closed-form results, which is equivalent to predict 77800 cycles to reach the 21 mm crack length.

Finally, the results from the linear-elastic CT-specimen FE model, can be summarized as follows:

- The displacement correlation method was sensitive to the hole's edge effect as a nonlinear variation of K as function of the fatigue crack length was observed. Thus, larger discrepancies were reported in the K-values for the center-hole-plate base model (hole boundary condition) regarding the closed-form solution, while results in agreement with the closed-form solution were reported for the CT-specimen FE model.
- The ΔK-values obtained by the 3D CT-Specimen FE model with the displacement correlation method exhibited less than a 2% of discrepancy regarding the closed-form solution.

- The ΔK-values obtained through the 3D CT-Specimen FE model along with the contour integral method exhibited a value of approximately 17.3% of underestimation and 4% of overestimation regarding the closed-form solution for the surface and half of the thickness of the 3D CT-specimen FE model (Figure 59).
- The Paris-Erdogan empirical relation was used to obtain the fatigue crack growth rates *da/dN* associated with the different ΔK-values (Displacement correlation, contour integral and closed form solution). The results of the *da/dN*-values were compared against experimental results reported on the literature by Ambriz [40] (Figure 61).
- Despite slight variations were found between the predicted and the experimental *da/dN* data were found (Figure 61), the fatigue life estimations turned out to be very conservatives regarding the experimental results. To improve the linear-elastic 3D CT-specimen FE model and its fatigue life predictions, the *da/dN* values estimation was adjusted based on experimental results reported on the literature by Ambriz [40]. The adjustment was done by the table look-up scheme, such adjustment consists on modifying the *da/dN*-values as function of the ΔK-values reported on the experimental study reported by Ambriz [40]. That is to say, as the ΔK-values were known from the experimental study and therefore their corresponding experimental *da/dN*-values, an adjustment of the numerical *da/dN*-values were done as function of those experimental ΔK-values.
- An enhancement of the *da/dN*-values calculated by the displacement correlation, contour integral and closed-form solution was achieved by the table look-up scheme (Figure 64) and therefore, an enhancement for the fatigue life estimations.
- An approximate 96% accurate fatigue life estimation was achieved by the usage of the results from the closed-form solution and the table look-up scheme.
- An approximately 91% accurate fatigue life estimation was achieved by the 3D CT-specimen FE model along with de displacement correlation method and the table look-up scheme (Figure 64).
- Nevertheless, regarding the experimental data, the fatigue life estimations from the contour integral results within the 3D CT-specimen FE model, overestimated the fatigue life by 24% for the surface of the FE model, and underestimated the fatigue life by 39%, for the contour integral at the half of the thickness of the 3D CT-specimen FE model respectively. Such significant differences between the fatigue life estimations and the experimental fatigue life, are attributed to the ΔK-values discrepancies previously shown on Figure 59.

4.2.3 Displacement correlation method study

The *K*-values calculated through the center-hole-plate base model and the displacements correlation method, exhibited a non-linear behavior, which can be appreciated on Figure 52 and Figure 54(a) and (c). To show the displacement correlation method sensibility to the boundary conditions and geometry presented on the central-hole-plate base model a comparison of the displacement correlation method behavior between the central-hole-plate model and the CT-specimen FE model was conducted. The computational FE model for a standard Compact Tension (CT-specimen) were conducted to further analyze the effectiveness of the displacement correlation method for the calculation of the *K* values. The literature revision about the usage of the displacement correlation method to calculate *K* indicated that the non-linear behavior observed for the *K* results in Figure 52 and Figure 54 has not been previously reported.

A 10 mm cracked CT-specimen 2D FE model was analyzed to study the *K*-values behavior from the displacement correlation method. The *K*-values from the displacement correlation method were studied at different mesh refinement levels, the coarsest element size was 1 mm and the finest element size was 0.05 mm. Moreover, the behavior of the *K*-values was studied with 4-node bilinear plane stress and 8-node quadratic elements. Figure 65(a)-(b) shows the results of the displacements correlation method for the finest element size (0.05 mm) and for linear and quadratic elements. Additionally, the non-linear results for the finest element size (0.079 mm) from the center-hole-plate base model are shown to compare the *K*-values behavior.

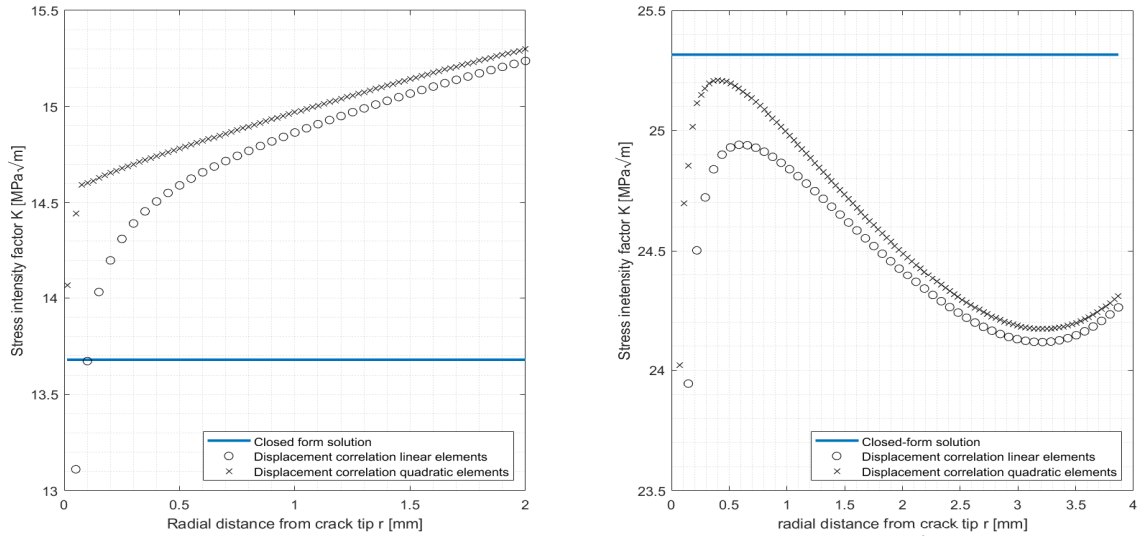

Figure 65. *K*-values numerical results from the displacement correlation method for a) 10 mm cracked CT-specimen linear-elastic FE model and b) 7 mm cracked center-hole-plate linear elastic FE model.

Contrarily to the non-linear behavior exhibited for the center-hole-plate model (Figure 65b), for the CT-specimen FE model, the *K*-values as function of the radial distance from the crack tip *r* (Figure 65a), agree with the information reported on the literature (see Figure 8), i.e. after discarding nodal *K*-values near the crack tip, only one slope is exhibited by the *K*-values results, therefore the extrapolation to the characteristic *K*-value at the crack tip ($r = 0$) is defined.

By comparing the results shown on Figure 65(a)-(b), can be determined that the displacement correlation method is sensible to the hole boundary condition. Inaccurate results were reported for the center-hole-plate base model, while acceptable results were reported for the CT-specimen FE model. Thus, unlike for the center-hole-plate base model, the use of the displacement correlation method along with the contour integral turned out to be suitable for the *K*-values calculation within the CT-specimen FE model.

4.3 CENTRAL-HOLE-PLATE MODEL PARAMETRIZATION

According to the previous discussion within the Chapter 1, cracks act as stress raisers within the mechanical components, therefore plastic deformations occurs at the vicinity of the crack tip. The generated plasticity zone near the crack tip is known as the plasticity zone. An analytical expression to estimate the plasticity radius were developed by G.R. Irwin. The Irwin approach to calculate the plasticity radius were presented on section 1.2 *Fatigue*.

To proceed with the parametrization of the center-hole-plate model the plastic material behavior simulation was essential. The simulation of the elastic-plastic material behavior was done according to the methodology presented on section *2.4.1 Implementation of elastic-plastic material behavior*.

Prior activating the plasticity behavior within the FE software, ABAQUS®, the plastic properties were defined for the commercial aluminum alloy 6061-T6. Figure 31 shows the experimental stress-strain curved used, such curve were reported on the literature by Torabi *et al.* [39]. Table 4 shows the coordinate pairs (stress-strain) extracted from the experimental stress-strain curve that were used within the FE model for the isotropic and combined hardening models. Moreover, Table 5 shows the coordinate stress-strain pairs used within the FE model to implement plasticity along with the kinematic model.

Once the plastic properties for the aluminum alloy 6061-T6 were defined, a convergence analysis was performed to determine the approximate finite element size that best captures the plasticity near the crack tip of the cracked center-hole-plate model.

The convergence analysis was performed by a one cycle loading simulation within a 5 mm cracked center-hole-plate 2D model. The simulations were performed for the isotropic, kinematic and combined hardening models. Figure 66 to Figure 68 Plastic zone results at the crack tip resolved by the combined hardening model at the maximum applied load for the central-hole-plate FE model. Element sizes: a) 0.079 mm b) 0.039 mm c) 0.019 mm and d) 0.01 mm approximate finite element size

shows the results for the convergence analysis for the three hardening models. The mesh used within the center-hole-plate model and the three hardening models were refined from an approximate element size of 0.079 mm till an approximate element size of 0.01 mm.

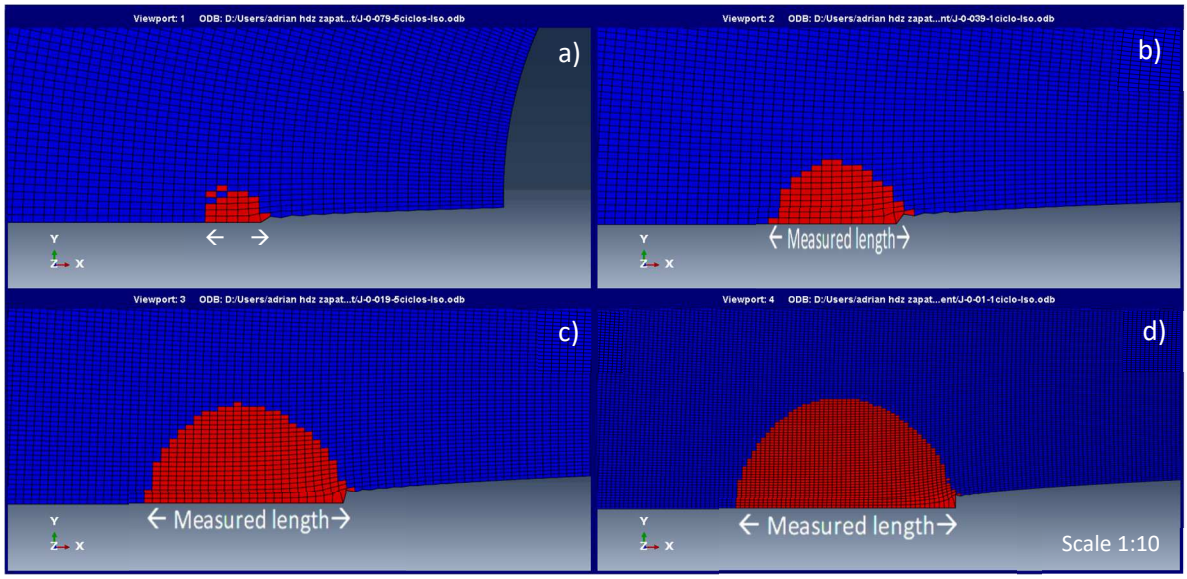

Figure 66. Plastic zone results at the crack tip resolved by the isotropic hardening model at the maximum applied load for the central-hole-plate FE model. Element sizes: a) 0.079 mm b) 0.039 mm c) 0.019 mm and d) 0.01 mm approximate finite element size

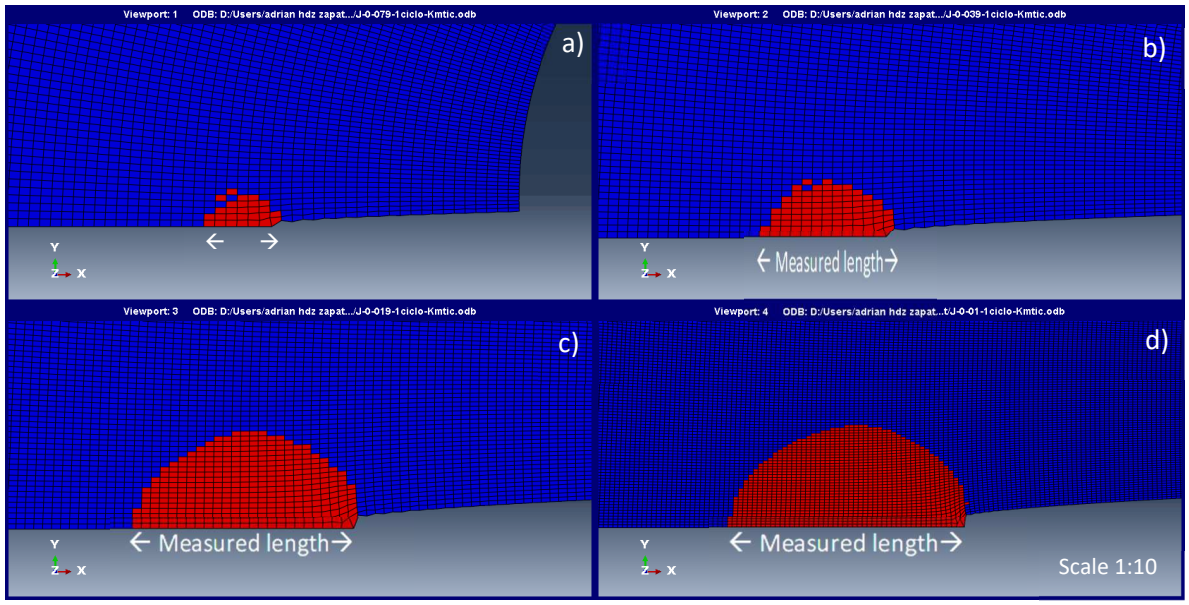

Figure 67.Plastic zone results at the crack tip resolved by the kinematic hardening model at the maximum applied load for the central-hole-plate FE model. Element sizes: a) 0.079 mm b) 0.039 mm c) 0.019 mm and d) 0.01 mm approximate finite element size

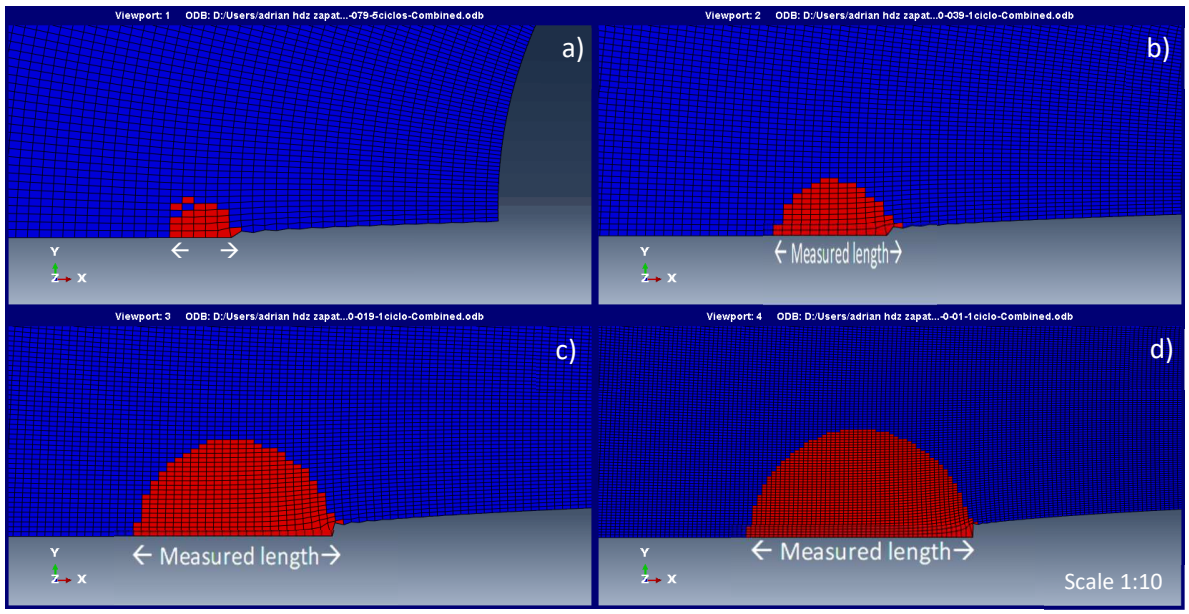

Figure 68. Plastic zone results at the crack tip resolved by the combined hardening model at the maximum applied load for the central-hole-plate FE model. Element sizes: a) 0.079 mm b) 0.039 mm c) 0.019 mm and d) 0.01 mm approximate finite element size

A half circular shape, which represents the plasticity zone, was generated near the crack tip. The diameter of the plasticity zone was measured along the X axis according to the legend shown on Figure 66 to Figure 68, "*Measured length*". The diameters of the numerically determined plasticity zone, were compared against the analytical value from the Irwin approach (Eq. 4) for a 5 mm cracked center-hole-plate model. The analytical value for the diameter of the plasticity zone, according to the Irwin approach, is 0.502 mm. Table 7 shows the approximate element sizes and their corresponding measured length as function of the three different hardening models.

Table 7. Plasticity radius captured by different finite element sizes

Hardening model	Isotropic	Kinematic	Combined
Element size [mm]	Plasticity radius [mm]	Plasticity radius [mm]	Plasticity radius [mm]
0.079	0.4792	0.5574	0.4779
0.039	0.5576	0.5178	0.5576
0.019	0.518	0.4981	0.518
0.01	0.4915	0.4915	0.5015

For the numerical simulations, the element size that exhibited the better results for the plasticity zone, regarding the analytical value from the Irwin approach, was the 0.019 mm FE size. Table 8 shows the results for the 0.019 mm approximate element size and the three hardening models.

Table 8. Results for the plasticity diameter of a 5 mm cracked center-hole-plate model

Approximate element size [mm]	Hardening model	Diameter of the plasticity zone [mm]
0.019	Isotropic	0.5180
0.019	Kinematic	0.4981
0.019	Combined	0.4979

Additional to the convergence analysis regarding the plastic zone, simulations for 1, 5 and 10 loading cycles (R=0.1) were performed. The cyclic loading simulations were conducted to obtain the cyclic stress-strain curves corresponding to each hardening model. The FE parameters remained the same for the 1 cycle as well as for 5 and 10 cycles loading simulations, i.e. the crack propagation simulation was not performed. Figure 69 shows the hysteresis curves corresponding to the three hardening models.

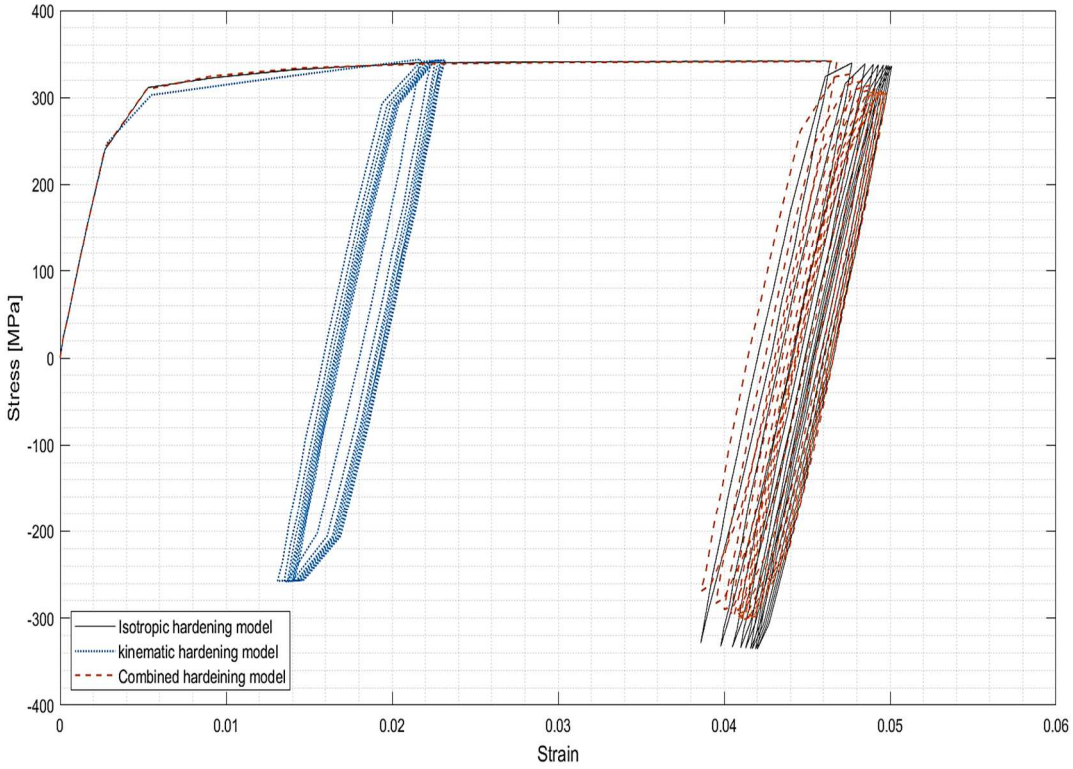

Figure 69. 10 cycles hysteresis curves for different hardening models

To generate the hysteresis curves shown on Figure 69, 10 loading cyclic simulations were performed. As can be appreciated on Figure 69, the cyclic stress-strain cyclic curves for the isotropic and combined models are very similar but differ from the kinematic. The differences among the three hardening models were studied by analyzing the behavior of the plasticity area generated near the crack tip, i.e. By studying the differences between the cyclic loading simulations performed for the results considering the isotropic, kinematic and combined hardening models.

The evolution of the plasticity active area near the crack tip was studied within the 10 loading cycles simulation. The plasticity area generated near the crack tip were measured at specific intervals during the 10 loading cycles simulation. The plasticity active area was measured at the maximum and minimum load of the 1st, 3rd, 7th and 10th cycle. Table 9 shows the results of the area measurements for the three hardening models, moreover Figure 70 shows the behavior of the plasticity area at the maximum and minimum loads as function of the cycle at which it was measured.

Table 9. Plasticity area evolution during a 10-loading cycle simulation. Plasticity area at the crack tip of a 5 mm cracked center-hole-plate model. Maximum load such that induced 30% of the yield strength for the Al 6061-T6 and load ratio R of 0.1

Cycle	Plasticity area from isotropic hardening model $[mm^2]$		Plasticity area from kinematic hardening model $[mm^2]$		Plasticity area from combined hardening model $[mm^2]$	
	Maximum load	Minimum load	Maximum load	Minimum load	Maximum load	Minimum load
1	0.0869	0.00326	0.0784	0.00478	0.0865	0.00413
3	0.0619	0.00239	0.068	0.00326	0.0672	0.00457
7	0.0587	0.00239	0.0328	0.00326	0.0644	0.00457
10	0.0504	0.0022	0.023	0.00348	0.0635	0.00457

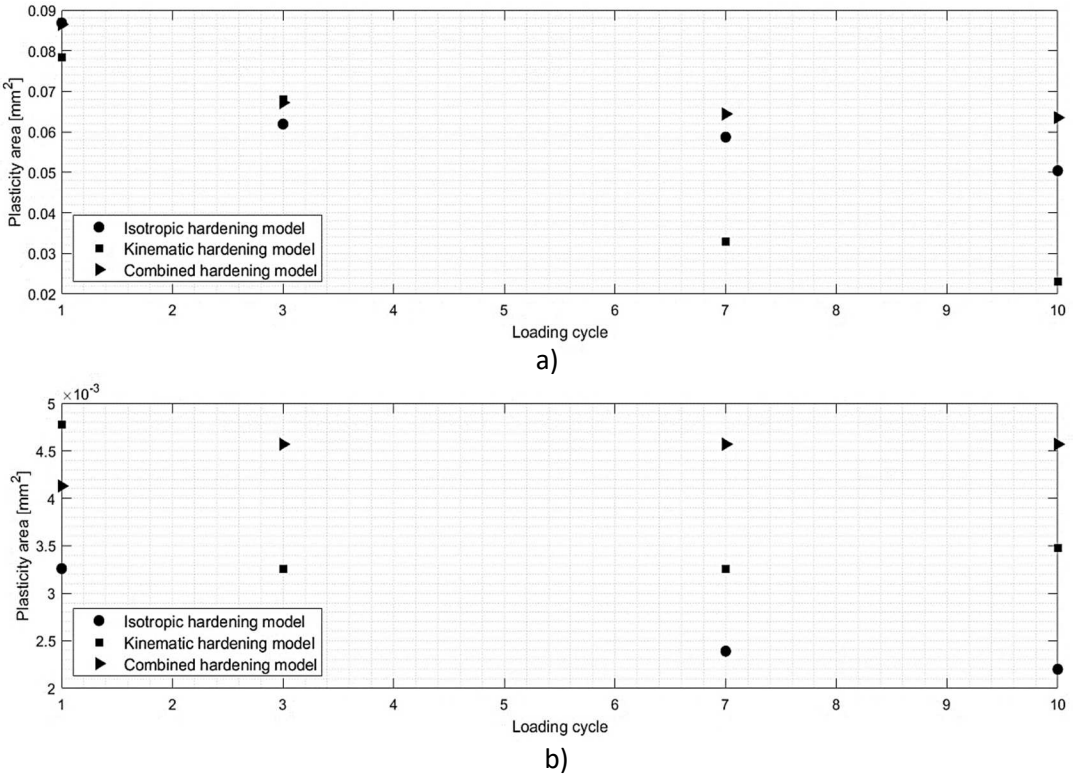

Figure 70. Plasticity active area behavior within a 10-loading cycle simulation. FE approximate size 0.019 mm.

As it can be noted on Table 9, for the isotropic hardening model the plasticity active area at maximum load reduces significantly from the 1st to the 3rd cycle (28% plasticity active area reduction), and then

varies only slightly from the 3rd to the 7th and 10th cycle. On the other hand, for the plasticity active area at minimum load the behavior is similar. The plasticity active area reduces 26% from the 1st to the 3rd cycle, and then varies only slightly.

For the kinematic hardening model, the plasticity active area at maximum load is reduced in 13% from the 1st cycle to the 3rd cycle, 51% from the 3rd to the 7th cycle and 30% from the 7th to the 10th cycle, i.e. The plasticity active area keeps decreasing as the loading cycles go by. For the plasticity active area at minimum load there are a 31% area reduction from the 1st to the 3rd cycle and then there are only slight changes.

Finally, the evolution of the plasticity active area within the combined hardening model exhibits a similar behavior to the plasticity area evolution within the isotropic hardening model. The plasticity area at maximum load with the usage of the combined hardening model reduces 22% from the 1st to the 3rd cycle, and then varies only slightly. While the plasticity area at minimum load increases 10% from the 1st to the 3rd cycle and then remains stable.

The results of the plasticity area evolution at maximum load during a 10 loading cycles simulation that were presented within Table 9, also can be appreciated on Figure 71. Figure 71 shows the results for the isotropic, kinematic and combined hardening model in columns a, b and c respectively, moreover Figure 71 shows the plasticity area at the 1st, 3rd, 7th and 10th cycle in the rows 1, 2, 3 and 4 respectively.

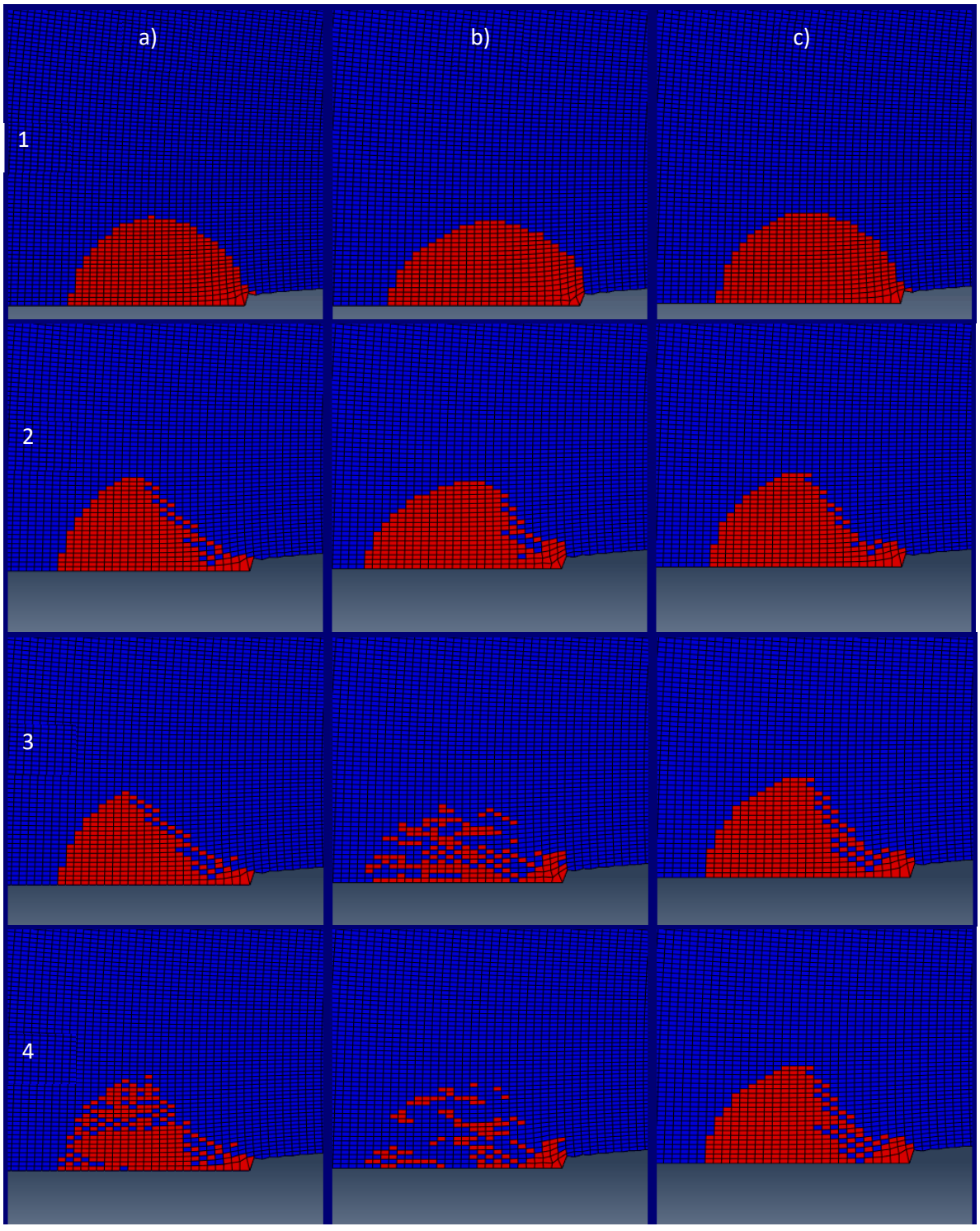

Figure 71. Plasticity area evolution on a 10-loading cycle simulation within a 5 mm cracked center-hole-plate model row 1 represents the 1st loading cycle, row 2 represents the 3rd loading cycle, row 3 represents the 7th loading cycle and row 4 represents the 10th loading cycle. Columns show the results as follows: a) Isotropic hardening model b) Kinematic hardening model c) combined hardening model

According to the results shown on Table 9, Figure 70 and Figure 71 the evolution of the plasticity active area near the crack tip is affected by the cyclic loading. The general trend shows that the plasticity active area at maximum load decreases as the loading cycles goes by while the plasticity active area remains stable at minimum load. However, there are clear differences between the three hardening models used.

The isotropic and kinematic hardening models shows higher and more abrupt changes regarding the plasticity active area captured during the 10 loading cycle simulations. On the other hand, the combined hardening model behaves more stable regarding the evolution of the plasticity active area during the cyclic loading simulations, i.e. the plasticity area reductions are smooth during the 10 loading cycles.

Once the elastic-plastic properties for the aluminum alloy 6061-T6 were defined and through the conjunct results from the central-hole-plate 2D FE model, which are: The finite element size analysis (Table 7), the stress-strain cyclic curves comparative and the plasticity area evolution on the cyclic loading simulations for the three hardening models, it was defined the use of an approximate finite element size of 0.019 mm along with combined hardening model for further simulations. Besides, once the combined hardening model was defined, a study within a 10-loading cycle simulation was conducted to observe the equivalent plastic strain evolution in the vicinity of the crack tip. Figure 72 shows equivalent plastic strain (PEEQ) as function of the steps in the simulation. Step one represents the first maximum load, then step two represents the first minimum load so two steps are one cycle. The X axis of Figure 72 shows the 20 steps of the simulation which corresponds to the 10 loading cycles. As it can be appreciated on Figure 72, the PEEQ for the FE that were located near the crack tip (2^{nd}) increases every cycle due to the stress concentration. On the other hand, once a value of PEEQ is reached within the FE located farther from the crack tip (8^{th}), the PEEQ is maintained through the cycles.

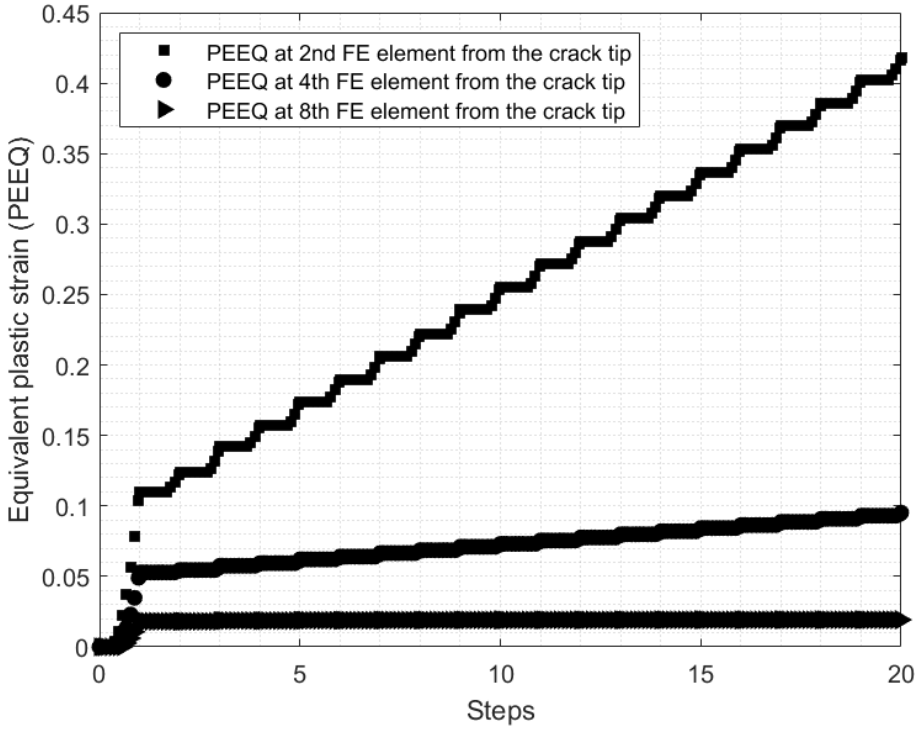

Figure 72. Equivalent plastic strain behavior for a 8 mm cracked central-plate-hole FE model during a 10-loading simulation. Two steps are equivalent with one loading cycle.

Though, once the hardening model and the element size to be used for the elastic-plastic material behavior were defined, the ΔK-values as function of the crack length a were computed for the 1 and 5 loading cycles simulations so the plasticity history was included on the ΔK-values calculus within the central-hole-plate 2D FE model. Figure 73 shows the comparison between the ΔK-values calculated at the 1st and 5th cycle as well as the ΔK-values calculated for the pure elastic center-hole-plate model as reference.

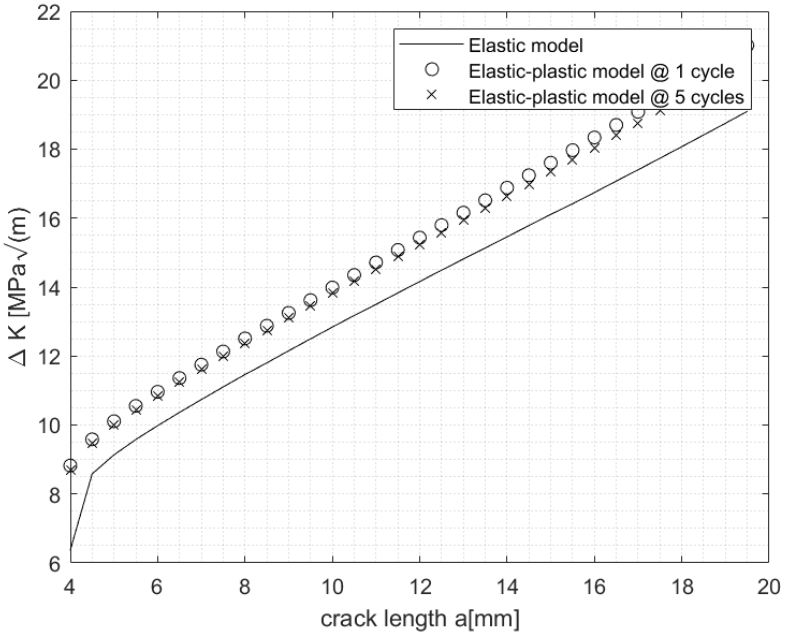

Figure 73. Δ*K*-values calculated for cyclic loading simulations within a cracked center-hole-plate model. Δ*K*-values for pure elastic and elastic-plastic center-hole-plate models

According with the results shown on Figure 73, despite the plasticity active area reduction previously shown on Figure 71, resembling Δ*K*-values are obtained on the computational model whether if they are calculated at the first cycle or at subsequent cycles, therefore for simplicity and computational resources optimization the Δ*K*-values were calculated with only one loading cycle in further simulations.

4.4 COLD HOLE EXPANSION (RESIDUAL STRESS CONDITION)

4.4.1 Mandrel geometry effects in the residual stresses

The results of the direct mandrel cold hole expansion simulations for the center-hole-plate model will be presented as follows: first, the reaction force produced on the mandrel during the hole expansion as a function of its displacement through the central-hole-plate model and second, the residual stress prediction within the three-level sub modelling technique.

As previously mentioned on section *3.1 Mandrel FE model*, for the present work two mandrel geometries have been modelled. A completely cylindrical mandrel and a conical mandrel, both with a maximum radius of 3.305 mm. The 3.305 mm radius generated a radial interference of 4%.

The reaction force was measured at the reference point of each mandrel FE model, the reference point (RP) can be appreciated on Figure 36. The reaction force was measured at every step of the

simulations, i.e. once by every prescribed displacement of the mandrel through the center-hole-plate model. The reaction force of the FE models was measured to observe the effect of the mandrel geometry on the reaction force and to compare such results against the experimental data reported on the literature by Cuevas [43]. Figure 74 shows the normal component (Y) of the reaction force on the mandrel as function of the displacement.

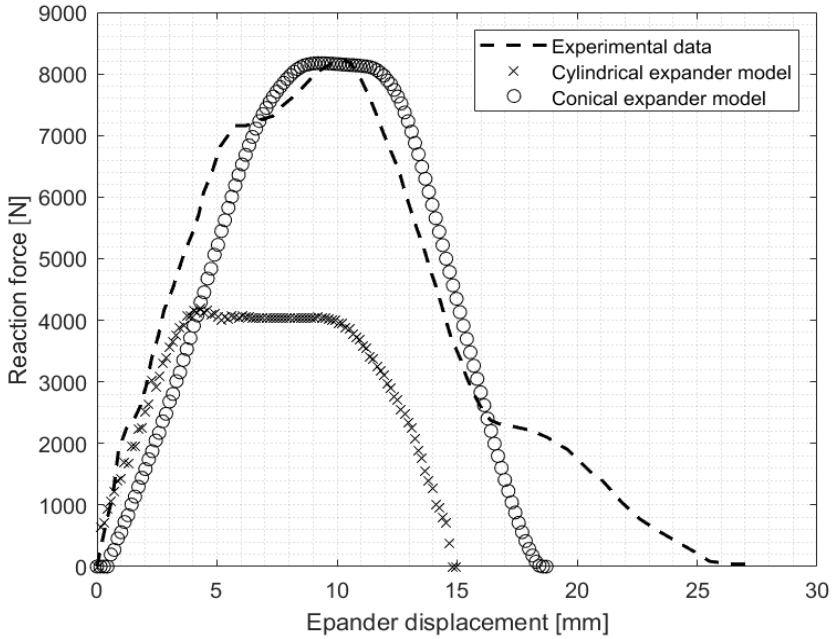

Figure 74. Reaction normal force component (Y) as function of the mandrel's displacement through the central-hole-plate model, numerical and experimental results comparative

As it can be appreciated on Figure 74, the behavior of both modelled expanders is similar, nevertheless the reaction force is sensible to the expander geometry despite both provoked a 4% of radial interference.

The maximum force reached by the cylindrical mandrel was around 4 kN, then such force is maintained as the expander go through the center-hole-plate model and starts to decrease as the mandrel leaves the center-hole-plate model. For the conical mandrel the maximum force reached was around 8 kN and, like the cylindrical expander, the maximum force is maintained while the conical mandrel goes through the central-hole-plate model and then decreases as the conical mandrel leaves the central-hole-plate model.

The numerical results for the normal component of the reaction force within the mandrels are compared against the experimental data reported by Cuevas [43]. The reaction force on the cylindrical expander resembles to the experimental force approximately within the first 4 mm of the mandrel

displacement, however, the maximum force reached by the simulation with cylindrical expander was approximately the half of the experimental reaction force.

On the other hand, the reaction force captured during the simulation with the conical mandrel resembles to the experimental reaction force along the whole mandrel travel through the center-hole-plate model, furthermore the maximum force reached by the simulation with conical mandrel and experimentally are both around 8 kN.

The aim of the cold hole expansion process is the induction of a residual stress (RS) field around the expanded hole. A comparison between the predicted RS field generated by the simulation with cylindrical and conical expander is shown in the following Figure 75, moreover a comparison between the RS field captured by the different FE densities presented on the three-level sub modelling technique is also presented. The RS predictions are focused on the normal component (Y) of the RS, since it is the most relevant component due to the loading mode within the fatigue simulations was the mode I (see Figure 2).

Figure 75(a)-(b) shows a comparison between the normal component in the *Y*-axis of the RS generated by cold hole expansion with cylindrical and conical mandrel. The 1D RS distribution shown on

Figure 75(a)-(b) was captured by the intermediate sub model (I-SM). Moreover, the RS normal component has been measured radially from the hole edge and through the thickness of the center-hole-plate model (Entrance face, mid-plane and exit face).

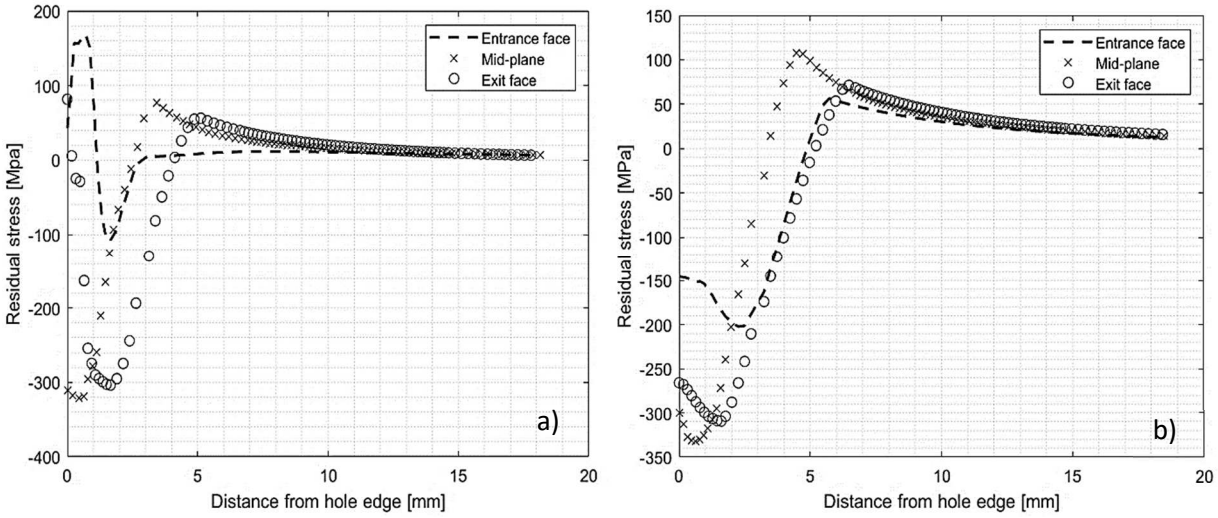

Figure 75. Normal component (Y) of the residual stress field within a center-hole-plate model expanded by a) Cylindrical mandrel and b) Conical mandrel

Figure 75(a) presents the RS distribution for the entrance face, mid-plane and exit face in the central-hole-plate obtained from the FE simulation with the cylindrical mandrel. The entrance face presented a region of increasing-decreasing tensile RS from the hole's edge up to approximately 1 mm, follow by a region of decreasing-increasing compressive RS from 1 mm up to 3 mm. Afterwards, the RS remained at almost a cero value. The mid-plane presented the larger compressive RS at the hole's edge, with a value of approximately 300 MPa. The compressive RS decreased from the 300 MPa value at 1 mm from the hole's edge up to a cero value at 2.5 mm, where the RS change to an increasing tensile condition. The larger positive RS value was of approximately 80 MPa at 3.5 mm, afterwards the RS decreased to a cero value at 10 mm-distance. The exit face presented a positive RS value of approximately 90 MPa at the hole's edge. The RS distribution decreased to a value of negative 300 MPa as a function of the distance from the hole's edge at 2 mm, where the RS distribution increased up to a value of positive 60 MPa at 5 mm. Afterwards, the RS distribution decreased to a cero value at approximately 10 mm and remained at the cero value.

Figure 75(b) shows the results for the RS distribution obtained from the FE simulation with the conical mandrel. The entrance face presented a region of increasing compressive RS from the hole's edge up to approximately 2.5 mm, followed by a region of decreasing compressive RS up to 5 mm where the RS changed to an increasing tensile condition up to 6 mm, afterwards the RS decreased to a cero value at an approximate distance of 10 mm. The maximum compressive RS for the entrance face was at 2.5 mm and it was 200 MPa. The mid-plane presented an increasing RD from the hole edge up to 0.5 mm, followed by a decreasing compressive RS up to 3.5 mm where the RS changed to an increasing tensile condition up to 4.5 mm, afterwards the RS decreased to an approximate cero value at 10 mm. The mid-plane presented the most compressive and tensile RS, the most compressive RS was reached at 0.5 with a magnitude of 340 MPa while the most tensile RS was reached at 4.5 mm with a magnitude of 110 MPa. The behavior of the RS at the exit face was similar to the RS on the entrance face, an increasing compressive RS is presented from the hole edge up to 1.5 mm, followed by a decreasing compressive RS up to 5 mm where the RS changed to an increasing tensile condition up to 6.5 mm, finally, the RS decreased to an approximate cero value at 10 mm. The maximum compressive RS for the exit face was at 1.5 mm with a magnitude of 310 MPa.

The results indicated that the effect of the cold hole expansion, either with the cylindrical or conical mandrel, are present radially from the hole's edge up to approximately 10 mm. For larger than a 10 mm-distance from the hole's edge, the effect of the cold hole expansion is negligible. However, by comparing Figure 75(a)-(b) it has been exposed that, as the reaction force, the RS field is sensible to the mandrel geometry. The RS at the hole edge generated by the cylindrical mandrel, are on a tensile

condition for the entrance and exit faces and compressive for the mid-plane. The tensile RS within the entrance and exit faces is associated with the material drag out-of-plane on the hole edge due to the contact interaction between the mandrel and the center-hole-plate model. The RS are superimposed with the external applied loads, thus, the regions with tensile RS results in critically stressed regions. The nucleation and growth process of fatigue cracks are more favorable in these critically stressed regions.

Contrary, the RS at the hole edge generated by the cold hole expansion with conical mandrel, are on a compressive condition for the three planes studied (entrance face, mid-plane and exit face). The radial interference between the maximum radius of the conical mandrel, and the center-hole-plate model is reached gradually, and no material drag out-of-plane is presented for the cold hole expansion with the conical mandrel. Figure 76(a)-(d) shows the comparative of the results for the displacements within the center-hole-plate model due to the cold hole expansion with the cylindrical and conical mandrels.

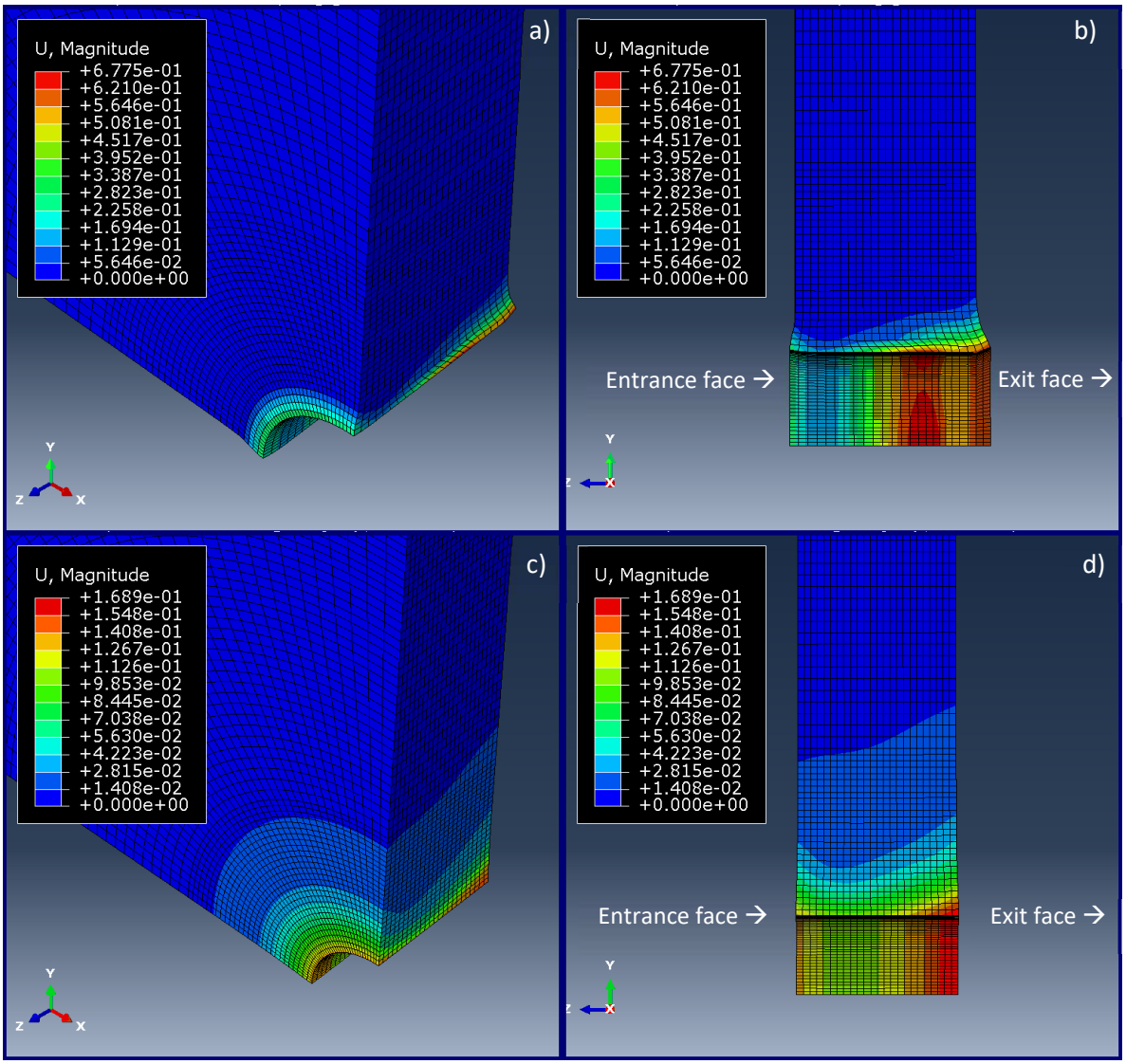

Figure 76. Displacements within the center-hole-plate model due to cold hole expansion a) Expansion with cylindrical mandrel isometric view b) Expansion with cylindrical mandrel cross section c) Expansion with conical mandrel isometric view b) Expansion with conical mandrel cross section

Figure 76(a)-(b) shows the displacements results for the cold hole expansion with the cylindrical mandrel. The material drag out-of-plane can be appreciated on Figure 76(b) at the entrance and exit faces of the central-hole-plate model. Figure 76(c)-(d) shows the displacements results for the cold hole expansion with the conical mandrel, but contrary to the cold hole expansion with the cylindrical mandrel, minimal material drag out-of-plane is present, as shown on the isometric and cross section views.

As mentioned on section *Residual stress considerations on fatigue design*, the tensile RS damage the mechanical components accelerating the fatigue crack growth while the compressive RS delay the

crack initiation and propagation. Considering that the RS predicted by the cold hole expansion with the cylindrical mandrel, which are shown on Figure 75(a), are primary tensile due to the material drag out-of-plane, such as can be appreciated on Figure 76(b), the simulations of cold hole expansion with cylindrical mandrel and therefore their corresponding fatigue simulations were discarded for further analysis.

In different circumstances, since minimal material drag out-of-plane is present on the cold hole expansion with conical mandrel, the predicted RS shown on Figure 75 (b) are compressive within the whole center-hole-plate model, thus, according to the information reported on the literature [3], [4], it is expected an enhancement of the center-hole-plate fatigue life. Additionally the reaction force results from the conical mandrel model are in agreement with the experimental data reported by Cuevas [43], hence, only the cold hole expansion with conical mandrel and its corresponding fatigue simulations were considered for further analysis.

Despite the RS fields generated by the cold hole expansion with cylindrical and conical expander varies significantly from one another, the common characteristic of both expansions is that the entrance face remained as the region with less favorable RS condition. Therefore, the nucleation and growth process of fatigue cracks are more favorable in such critically regions and from here on the analysis will be focused on the entrance face.

4.4.2 Cold hole expansion sub models

Figure 77 shows the normal component of the RS generated at the entrance face by the cold hole expansion with conical mandrel. Moreover, Figure 77 shows the comparative between the RS field captured by the different FE mesh densities of the three-level sub modelling technique (Global Model GM, Intermediate Sub Model I-SM and Fine Sub Model F-SM).

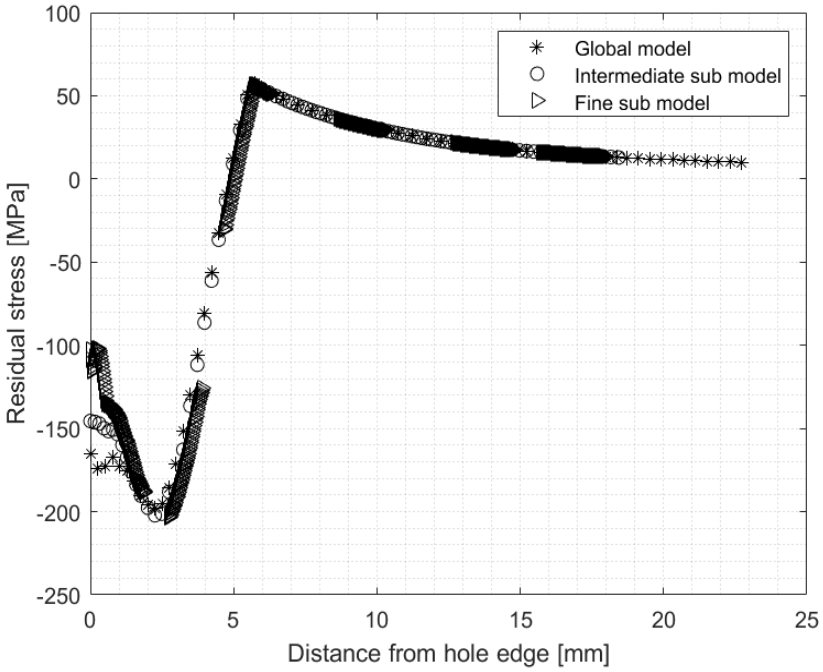

Figure 77. Normal component of the residual stress generated by the cold hole expansion with conical mandrel

Figure 77 shows that the RS captured at the hole edge by the GM, the I-SM and the F-SM, exhibits significant discrepancies within the first 3 mm, while for the other distance from the hole edge remained identical. The compressive RS captured at the hole edge (x=0) by the GM, I-SM and F-SM are 165, 145 and 100 MPa. The three-level FE models shows an increasing compressive RS region from the hole edge up to 2.5 mm, followed by a decreasing compressive RS up to 5 mm where the RS changed to an increasing tensile condition up to 6 mm, afterwards the RS decreased to a negligible value after approximately 10 mm. The maximum compressive RS value for the three-level sub models was around 205 MPa at 2.5 mm while the maximum tensile RS for the three-level sub models was approximately 60 MPa at 6 mm. The differences between the RS captured by the three-level sub models are located within the first 5 mm radially measured from the hole edge, afterwards the RS fields captured by the three-level sub models are superimposed i.e. the transition between the three-level sub modelling technique is adequate, however the most affected zone by the cold hole expansion is the region within the first 5 mm.

As it can be appreciated on Figure 77, the results captured by the F-SM are not continuous along the whole distance from the hole edge as the F-SM were used only at the specific lengths. The model geometry for the F-SM spans over a small region from the hole edge. This region corresponded to a

distance from the hole's edge to ~2 mm. The FCG simulation was conducted for larger fatigue cracks (up to ~19 mm), thus, several F-SM for different fatigue crack lengths were developed. Figure 78 shows an overlay plot of the normal component of the RS captured by the three-level sub modelling technique.

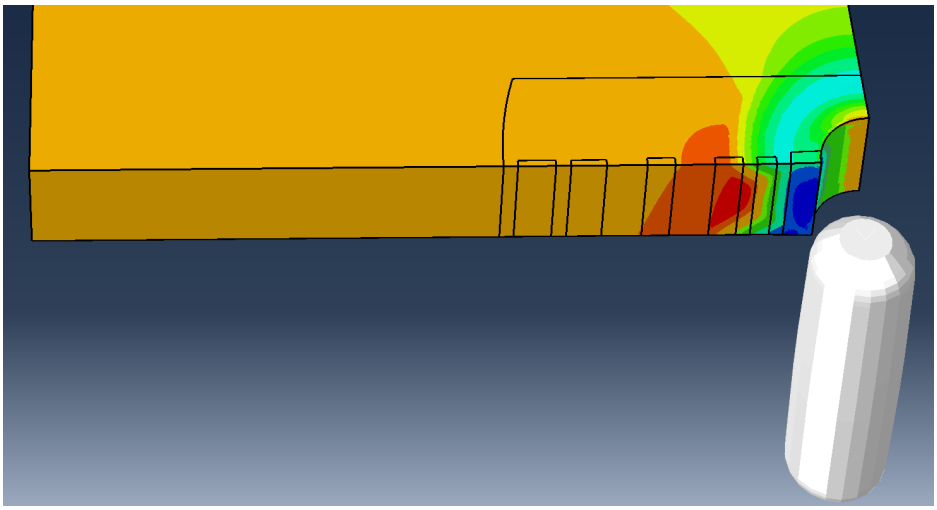

Figure 78. Three-level sub modelling technique overlay plot for the normal component of the residual stress generated within the center-hole-plate model due to the cold hole expansion with conical mandrel

The RS differences for the first ~2.5 mm between the GM, the I-SM and the F-SM are very significant as the *K*-values, and therefore the fatigue life predictions, are very sensible to slight changes on the predicted RS field. Table 10 shows the differences of calculating the ΔK-values on a 4 mm cracked center-hole-plate model for the three-level different models. Moreover, Table 10 shows the corresponding fatigue crack growth rates *da/dN* for the ΔK-values and the number of cycles required for a crack length increment of 0.5 mm. The corresponding *da/dN*-values were estimated through the Paris-Erdogan empirical relation (Eq. 7).

Table 10. Three-level sub modelling technique results comparative for a 4 mm cracked center-hole-plate model

FE model	$\Delta K\ [MPa\sqrt{m}]$	$\frac{da}{dN}\ [\frac{mm}{cycle}]$	Cycles (for a 0.5 mm crack increment)
Global model (GM)	10.956	1.1231e-04	4452
Intermediate sub model (I-SM)	5.6519	1.2476e-05	40077
Fine sub model (F-SM)	3.1457	1.7832e-06	280395

According to the information presented on Table 10, the *da/dN*-values differ from one another, depending on the FE model level, by a magnitude order. The most conservative *da/dN*-value was estimated by the GM, as it was the fastest fatigue crack growth rate. The GM estimated the smaller amount of cycles needed for a 0.5 mm crack length increment (4452). Contrary, the less conservative *da/dN*-value was predicted by the F-SM, as it was the slowest fatigue crack growth rate estimated. The F-SM estimated the higher amount of cycles needed for a 0.5 mm crack length increment (280395). The GM resulted in a number of cycles which is lower by 63 times regarding the F-SM, while the I-SM is lower by 7 times.

Within a full fatigue crack growth study, i.e. an analysis from the crack initiation up to the fracture, the GM underestimation would be accumulated at every crack length increment and therefore a very conservative fatigue life prediction would be given. The extremely conservative fatigue life estimations can lead to inefficiency and/or unnecessary costs when used for mechanical components within a system.

4.4.3 Fatigue crack growth simulations

With the elastic-plastic material behavior implementation, the cyclic loading simulations study and the cold hole expansion simulations (initial RS condition), the center-hole-plate model is considered parametrized for the fatigue simulations. As shown on Figure 47, once the center-hole-plate model was parametrized, the fatigue simulations were performed following the order of the three-level sub modelling technique (GM, I-SM and F-SM) and then, the *K*-values were computed within the F-SM.

At the beginning of chapter 4, two methods to compute the *K*-values within the linear-elastic models were studied, the contour integral method and the displacement correlation method. The results if such study resulted in discarding contour integral method and the displacement correlation method

was defined for the rest of the present work, however in the case of the elastic-plastic material model, it was necessary to define whether the previously method (displacement correlation) can be used or if it was required to make other considerations so, prior the fatigue simulations, a study to define the most convenient method to compute the *K*-values was necessary. The evaluated methods to compute the *K*-values were the contour integral, the displacements correlation and the stress correlation methods.

Regarding the contour integral method, it is mostly used within linear-elastic material behavior due to the integral's values within linear-elastic analysis are path-independent. The use of the contour integral on elastic-plastic analyses is possible, nevertheless the contour integral values become path-dependent. To avoid the path-dependence, the domain of the contour integral must be large enough to surround the plasticity zone though, the plasticity generated by the cold hole expansion in the present work embraces the whole F-SM's and therefore the use of the contour integral method was not possible to compute the *K*-values. A 2D central-hole-plate model was developed to conduct a study about the path dependence of the contour integral values. The loading mode I was simulated within the 2D central-hole-plate model by prescribing a 165 MPa stress on the far end of the plate. Moreover, a 10.5 mm crack was simulated on the 2D model. The contour integral values were calculated following two different alternatives, first by defining a total of 30 contours for the domain of the contour integral method, and second by defining a total of 120 contours for the domain of the method. Figure 79(a)-(b)shows the results for the values of the contour integrals (J-integral) as function of the contour number in both cases, with the 35 contours and the 120 contours domain.

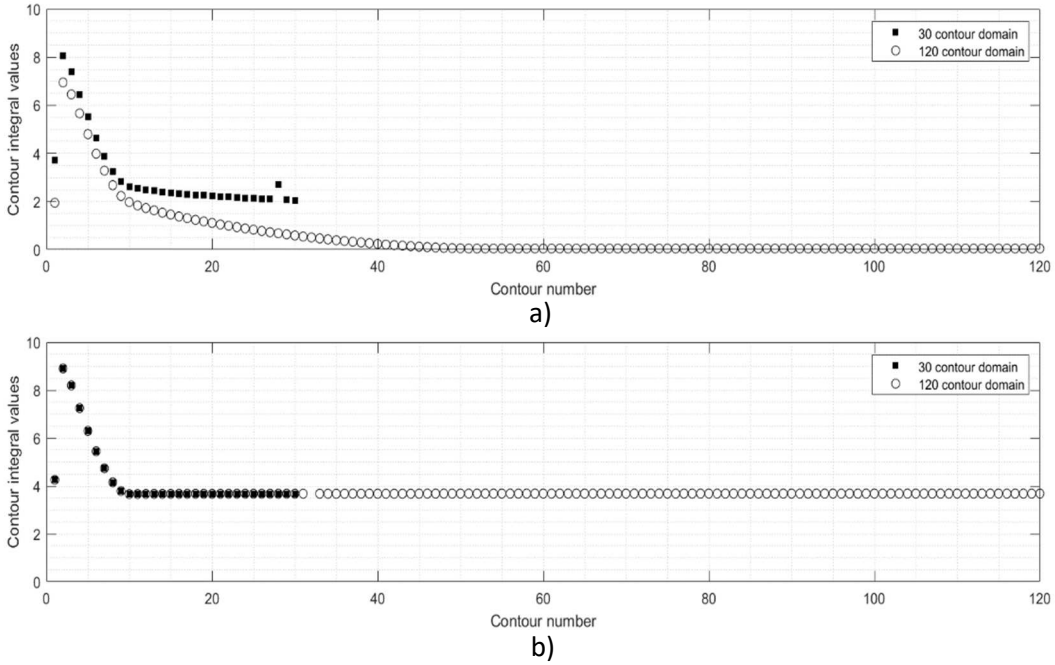

Figure 79. Contour integral values for minimum and maximum load within a 10.5 mm cracked central-hole-plate model as function of the contour number (domain)

As it can be appreciated on Figure 79(a), when the minimum load is prescribed to the model and only 30 contours are defined, the contour integral values as function of the contour number behaves stable but different from the case when 120 contours were defined. On the other hand, when the maximum load is prescribed to the model, the contour integral values behave in the same way for both domains definition (30 and 120 contours). The differences between the behavior of the contour integral values at the minimum a maximum load are likely attributed to the crack closer phenomenon, though such phenomenon has not been part of the scope of the present work. Besides, the variation of the contour integral values at minimum load affects the K-values at minimum load and therefore the ΔK-values. The path dependence of the contour integral values showed on Figure 79(a)-(b) can also be appreciated on Figure 80(a)-(b).

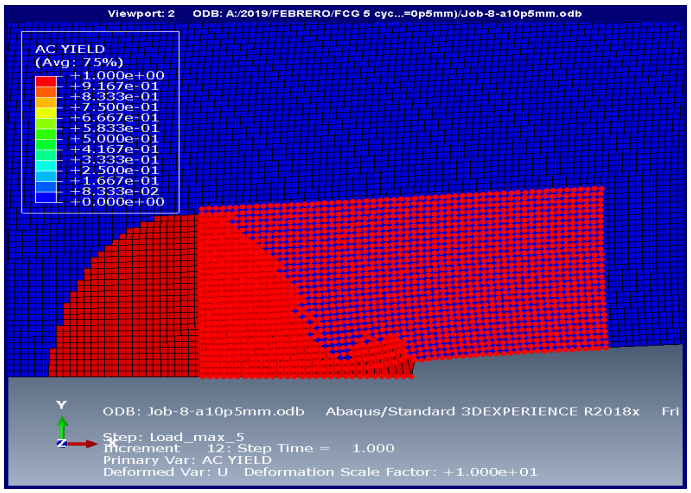

a)

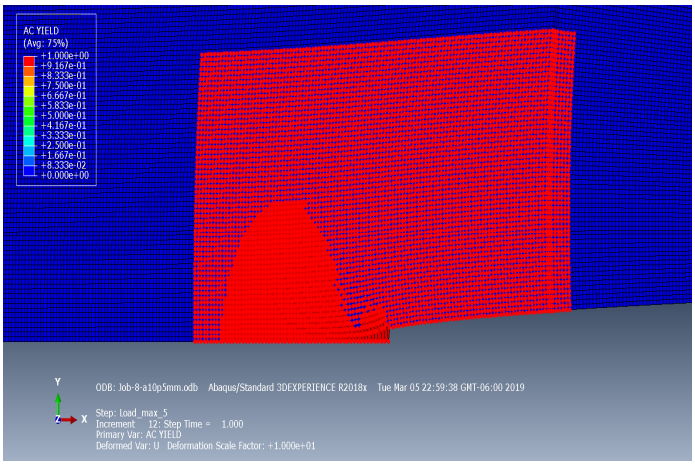

b)

Figure 80. Domain defined within a 10.5 mm cracked central-hole-plate FE model for the contour integral method with a) 30 contours and b) 120 contours

Figure 80(a) shows the domain (30 contours) for the 10.5 mm cracked central-hole-plate specimen, and as it can be appreciated the domain did not surrounded the plasticity region, thus the values of the contour integrals that differ from the wider domain (120 contours) shown on Figure 80(b) can be explained.

Regarding the displacement correlation method, the previously presented results on sections 4.2.1 and 4.4.1 showed that the displacement correlation method was not a valid method to compute the *K*-values within the center-hole-plate model due to an inadequate capturing of the hole boundary condition (non-linear behavior). To evaluate once more the displacements correlation method, and avoid the non-linear behavior, a new consideration has been done for the *K*-values extrapolation for

$r = 0$ (crack tip). The new consideration was done as follows: The *K*-values that exhibited the non-linear behavior were located far from the crack tip, therefore all the *K*-values farther than the half of the crack length were discarded (due to the hole boundary condition proximity) and the *K*-values near the crack tip, as usual, were also discarded. By doing the new consideration to the displacement correlation method, only the values of the central part of the *r-K* curve were extrapolated to find the most approximate solution for *K* at the crack tip ($r = 0$).

Moreover, the displacement correlation method, with the alternative method for the *K*-values extrapolation, has been compared against the stress correlation method. The displacements and stress correlation methods are equivalent methods derived from the Hooke's law, therefore very similar *K*-values should be found by one or the other method. The displacements and stress correlation methods comparative has been done for a 4, 7- and 9.5-mm crack lengths in the center-hole-plate model remotely loaded by a load of 49 kN and with elastic-plastic material model for the aluminum alloy 6061-T6.

Figure 81(a)-(c) shows the *K(r)* graphs corresponding to the comparative between the displacements and stress correlation methods. As previously explained, the displacement correlation used nodal solutions from the back nodes to the crack tip, and the stress correlation method used nodal solutions from the front nodes to the crack tip. Also, the results from the comparative study between the displacement and correlation methods is presented on Table 11 below.

Table 11. Displacement and stress correlation methods comparative. *K*-values results for a center-hole-plate cracked model.

Center-hole-plate model crack length $[mm]$	Displacement correlation method $[MPa\sqrt{m}]$	Stress correlation method $[MPa\sqrt{m}]$
4	11.471	11.963
7	14.122	15.07
9.5	16.096	16.813

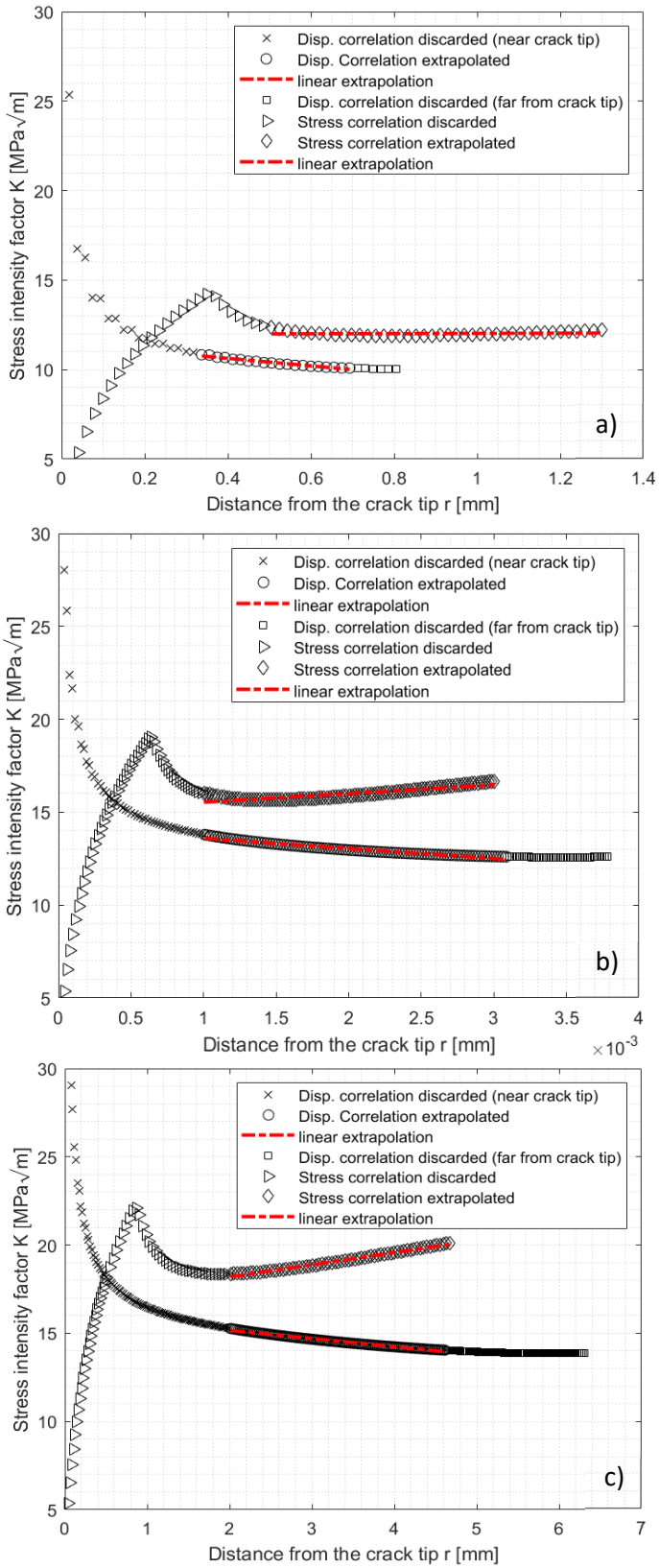

Figure 81. Displacement and stress correlation methods comparative within a center-hole-plate model cracked a) 4 mm b) 7 mm c) 9.5 mm

As shown on Figure 81(a)-(c), the consideration of only the central *K*-values within the *K(r)* curve obtained by the displacement correlation method, exhibited a linear behavior and therefore the extrapolation for $r=0$ was defined. On the other hand, when using the stress correlation method, and after discarding nodal results close to the crack tip, the rest of the *K*-values exhibited a linear behavior. The non-linearity was not present within the stress correlation method since the nodal stress measurements were done ahead the crack tip so, the hole boundary condition had no influence on the method.

According to the results shown on Table 11 and Figure 81(a)-(c) the differences between the extrapolated *K*-values by the displacement and stress correlation methods differ from one another by approximately 5%. To sum up, the displacement and stress correlation method equivalency was proved by three different crack lengths within a center-hole-plate model. Therefore, since the stress correlation method is not sensible to the hole boundary condition, the use of such method to compute the *K*-values was picked out for the fatigue simulations, which results will be shown on the following.

The approximate time required for the cold hole expansion simulation at the GM, the I-SM and F-SM, the crack generation and one loading cycle is approximately 54 hours plus the implementation user time. Moreover, the memory required to for a single cold hole expansion F-SM with its corresponding crack and loading cycle is around 6 Gb. The FE densities of the GM, I-SM and F-SM were previously reported in Table 6. In view of the afore mentioned conditions, only six crack lengths have been chosen for which the ΔK-values were computed. The crack lengths *a* selected were 4, 6, 8, 12, 16 and 19 mm, moreover the selection of such crack lengths is based on the plane fracture toughness for the aluminum alloy 6061-T6.

For the FE fatigue simulations, the experimental conditions reported on the literature by Cuevas [43] were replicated, i.e. a maximum force of 36 kN were imposed to the far end of the center-hole-plate specimen with a load ratio *R* of 0.1, Cuevas [43] reported an enhancement of the fatigue life of 1.5 to 3 times for the cold hole expanded center-hole-plate specimens regarding the specimens without an initial RS field.

The fatigue test experimental conditions were replicated so the computational model for fatigue crack growth could be validated against the experimental data. Within the FE center-hole-plate model and the fatigue simulations, the effective *K*-values at maximum and minimum load were computed for the above-mentioned crack lengths by the stress correlation method, and therefore the corresponding ΔK-values. The effective *K* values incorporated the plastic strain history, thus, original and redistributed residual stresses and strains produced by the cold hole expansion are incorporated into

the effective *K* calculation. Besides, the fatigue crack growth rates *da/dN* were also estimated through the Paris-Erdogan empirical relation and the material coefficients reported on the literature by Ambriz [40].

Figure 82 shows the *da/dN*-values determined by the computational model for fatigue crack growth, moreover, Figure 82 shows the experimental results for the *da/dN*-values measured on the left and right sides of the entrance face of the center-hole-plate specimen.

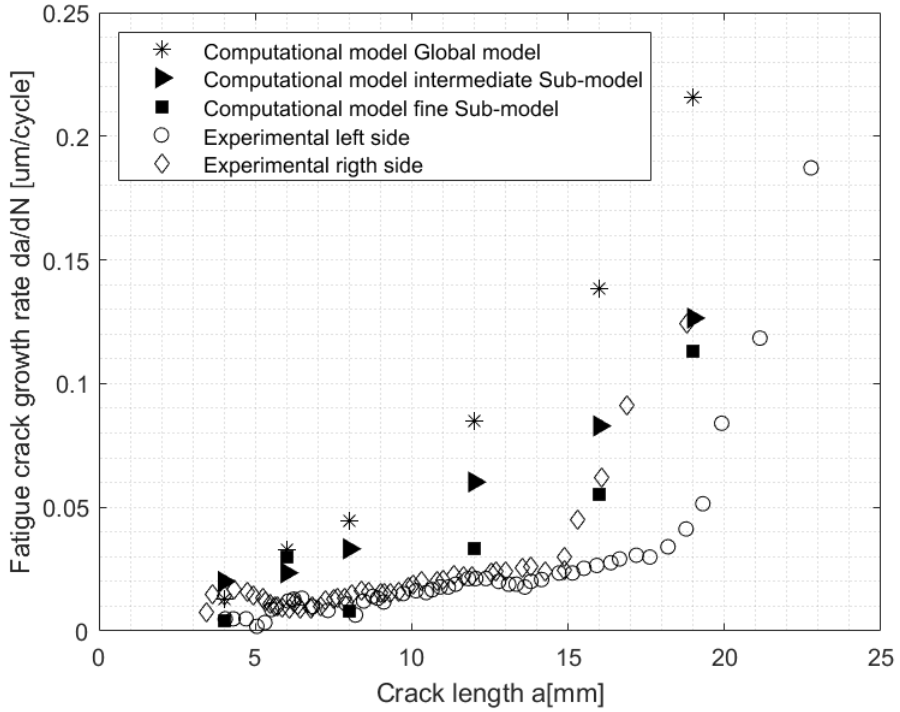

Figure 82. Fatigue crack growth rates *da/dN* as function of the crack lengths *a* for the entrance face of a cold hole expanded center-hole-plate specimen

Figure 82 shows that the experimental *da/dN*-values on the right side were slightly higher than the *da/dN*-values on the left side. The discrepancy between the experimental velocities captured in both sides of the center-hole-plate specimen can be attributed to the local variations near the hole, such as non-symmetric RS field, local material flaws or a combination of both [44].

The numerically determined *da/dN*-values, shown on Figure 82, follow the same trend than the experimental *da/dN*-values along the whole crack growth. Nevertheless, the *da/dN* numerical value for the 6 mm crack length turned out to be out of the general trend. The computational model

overestimated the 6 mm *da/dN*-value regarding the experimental results. Moreover, despite is within the general trend, the *da/dN*-value for the 10 mm crack was also overestimated by the computational model. Overestimation of the *da/dN*-values can lead to a conservative fatigue life estimation.

The overestimation of the numerical out-of-trend value at 6 mm, is attributed to the fact that within the region where the 6 mm crack is located, there are a particularity in the initial RS field for the fatigue simulation. As it can be appreciated on Figure 77, the normal component of the captured RS shows a change on the slope, i.e. Exhibits an increasing compressive trend, then reach the maximum compressive value and afterwards the trend change to a decreasing compressive RS condition.

The change on the RS field, generated by the cold hole expansion, cause the stress correlation method to turn unstable, that is to say, the *K*-values as function of the radial distance from the crack tip *r*, do not shows a linear behavior and therefore the extrapolation for the *K*-value at the crack tip ($r = 0$) is not clear.

Figure 83(a)-(b) shows the behavior of the stress on the FE central-hole-plate model within the region near to two different crack lengths, 4- and 6-mm. Figure 83(a)-(b) shows four different cases, the stress for the uncracked specimen (RS due to the cold hole expansion), the stress redistribution for the cracked specimen without load, the stress redistribution generated due to the minimum load and the stress redistribution generated due to the maximum load (Max load equal to 36 kN and $R = 0.1$).

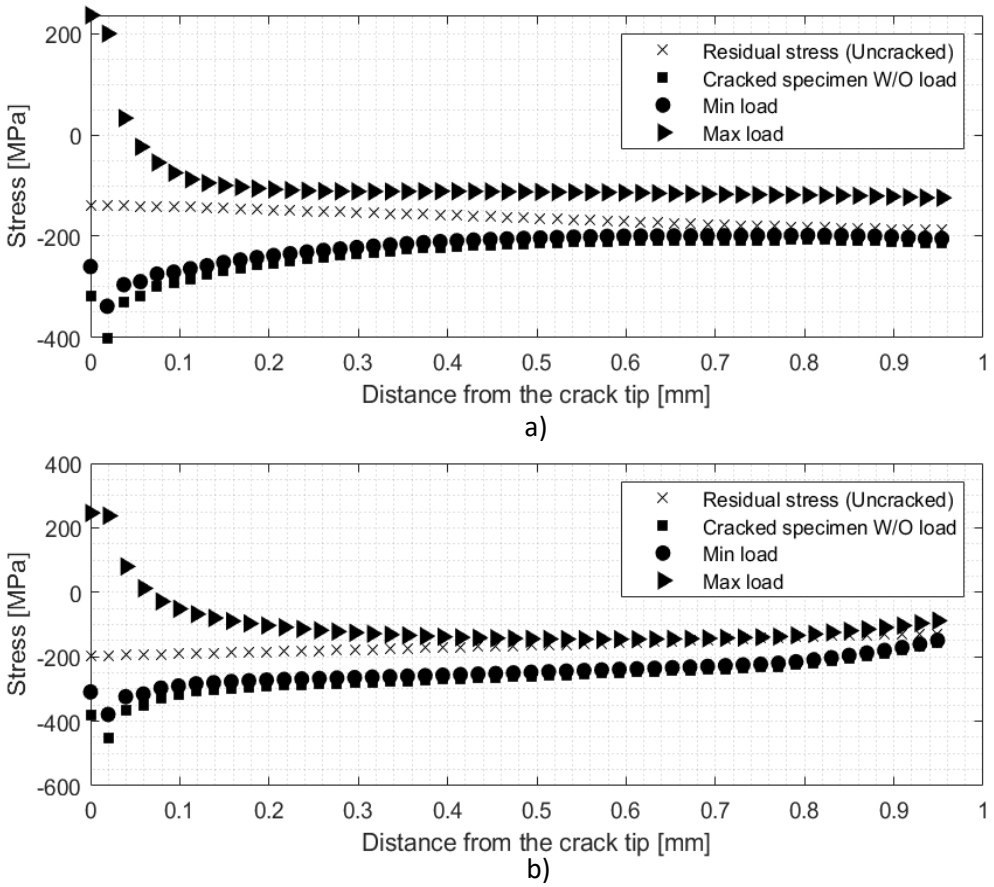

Figure 83. Stress captured by the F-SM near the crack tip for a) 4 mm cracked central-hole-plate FE model and b) 6 mm cracked central-hole-plate FE model.

The comparative between the stress behavior within the 4 mm and the 6 mm cracked F-SMs, can also be appreciated in Figure 84.

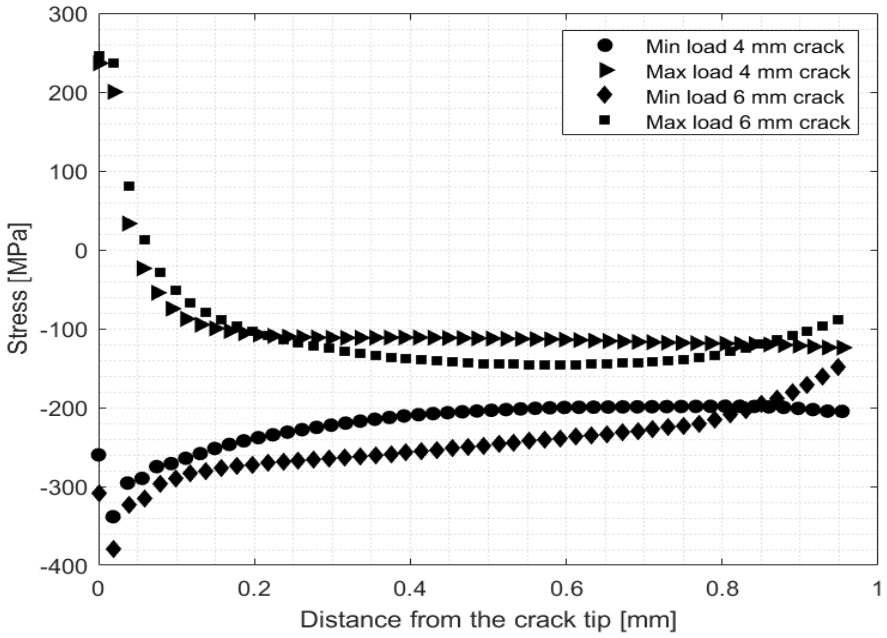

Figure 84. Stress redistribution for a cracked central-hole-plate F-SM.

Figure 85 shows the instability of the stress correlation method for maximum and minimum load for the 6 mm crack length due to the afore mentioned redistribution of the stress on the vicinity of the crack tip

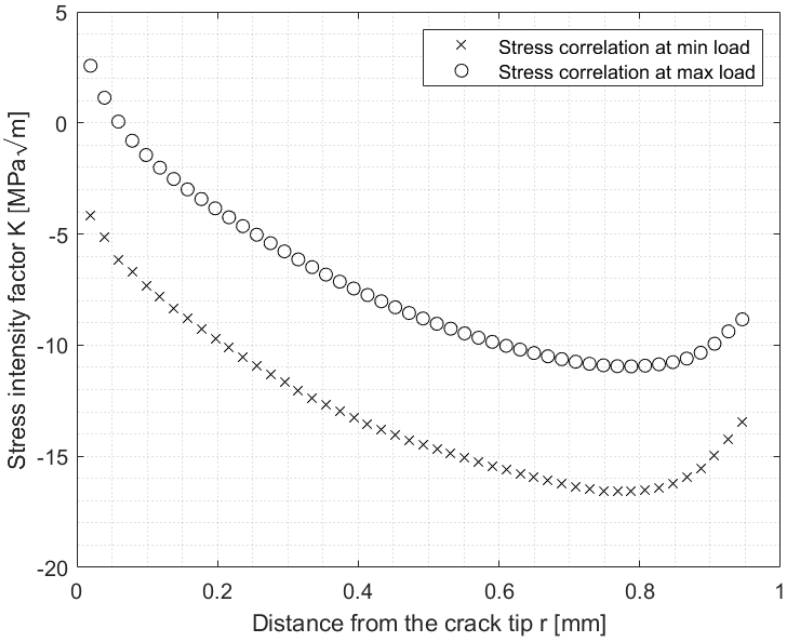

Figure 85. Stress intensity factor values as function of the radial distance from the crack tip for a 6 mm cracked center-hole-plate model subjected to a cold hole expansion process.

As it can be appreciated on Figure 85 the *K*-values either at maximum load or at minimum load, do not show a linear behavior and therefore deeper analysis to define the *K*-values for cracks of around 6 mm length should be done. However, for the present work only the stress correlation method has been used to compute the *K*-values, and the specific study of the influence of the increasing-decreasing compressive RS field behavior on the *K*-values will be part of the future work.

CONCLUSIONS

Within the present work different finite element models were proposed. Among them can be found the central-hole-plate 2D and 3D base models, for which only linear-elastic material behavior was studied. Also, parametrized central-hole-plate 2D and 3D models were proposed, for which elastic-plastic material behavior, cyclic loading and residual stress conditions were considered. Additional to the central-hole-plate models a compact tension specimen model (CT-specimen model) was developed for the 2D and 3D cases and linear-elastic material model. The finite element models were developed to estimate the stress intensity factors K within the different specimens and thus, perform the corresponding fatigue crack growth analyses.

For the linear-elastic central-hole-plate model the K-values were estimated by the displacement correlation method and by the contour integral method. The results were compared against the closed form solution reported in the literature. The displacement correlation method exhibited a non-linear behavior of K as function of r the distance behind the crack tip, which has not been reported in the literature. The non-linear behavior was attributed to the central-hole boundary condition; thus, the displacement correlation method is considered as not an appropriate method to estimate the K-values within the central-hole-plate FE model. On the other hand, the K-values calculation with the contour integral method exhibited only slight variations regarding the closed-form solution values (~3.4%). Ergo, the contour integral method performance exhibited accurate results with a relatively coarse FE mesh (~0.317 mm FE size), consequently it is considered an adequate method for the K-values estimation within the linear elastic central-hole-plate model.

A linear-elastic CT-specimen FE model was developed to further explore the non-linear behavior of the displacement correlation method that was presented in the linear-elastic central-hole-plate model. The performance to estimate the K-values by the displacement correlation method as well as the contour integral method were evaluated. Like in the central-hole-plate model, a convergence analysis demonstrated that the contour integral method provides accurate results with coarser FE mesh than the displacement correlation method. However, within the convergence analysis both methods converged at approximately the same value for specific crack lengths, which presented an approximate difference of 6% regarding the closed-form solution. Thus, according to the presented results both methods turned out to be appropriate for the K-values estimation within the linear-elastic CT-specimen model.

The ΔK-values were also computed for several fatigue crack lengths of the linear-elastic CT-specimen model, i.e. A fatigue crack growth analysis was performed. The Paris-Erdogan empirical relation was used to correlate the FCG rates da/dN with the ΔK-values. Material coefficients required by the Paris-Erdogan relationship for the Al6061-T6 reported in the literature were used. However, a notorious

sub estimation of the fatigue life was predicted by the computational model regarding experimental data reported in the literature, the numerical simulations predicted approximately one third of the experimental fatigue life. An alternative fatigue life estimation for the CT-specimen model was done by considering another adjustment to the material coefficients. The adjustment considered also the experimental ΔK-da/N curve reported in the literature, but a point-to-point adjustment known as table look-up scheme was used. By the application of the table look-up scheme, reliable fatigue life estimations can be achieved. The numerical fatigue life predictions for the linear-elastic CT-specimen FE model were of up to 91% of accuracy regarding the experimental fatigue life.

The study conducted for the linear-elastic CT-specimen FE model revealed that the non-linear behavior of the displacement correlation method can be attributed to the central-hole boundary condition.

For the parametrized FE central-hole-plate specimen, the elastic-plastic material model, cyclic loading and residual stress (RS) conditions were considered. Besides, the displacement correlation method, the contour integral method and the stress correlation method were studied. The parametrized central-hole-plate model was performed through a three-level FE sub modelling technique (Global model GM, Intermediate sub model I-SM and Fine sub model F-SM). Within the results of the predicted RS it has been found that the RS field is sensible to the expander geometry. A cylindrical tool generated tension residual stress at the entrance and exit faces of the specimen while the conical expander generated only compressive RS field within the expanded specimen. The predicted RS field that was captured for the F-SM differed from the RS field captured by the I-GM and GM within the first 5 mm from the hole edge. When performing effective K-values within the parametrized central-hole-plate model the contour integral, displacement and stress correlation methods were studied.

The usage of the contour integral method for the effective K-values calculation exhibited a path dependence behavior. The path dependence of the contour integral method could not be avoided due to the large plastic deformations presented in the F-SM. Thus, the utilization of such method is not recommended for the three-level sub modelling technique reported on the present work.

Regarding the usage of the displacement correlation method within the parametrized central-hole-plate model, the non-linear behavior previously reported for the linear-elastic central-hole-plate model was present again. Thus, it was confirmed that the method turned out to be sensible to the central-hole boundary condition regardless of the consideration of linear-elastic or elastic-plastic material model. Therefore, the usage of the displacement correlation method within the parametrized central-hole-plate model was not recommended.

On the other hand, the effective *K*-values estimated by the stress correlation method as function of the radial distance from the crack tip exhibited a linear behavior after discarding nodal points near to the crack tip. Thus, the extrapolation of the effective *K*-value for the crack tip was achieved successfully and such method has been considered as adequate for the effective *K*-values estimation within the three-level finite element sub modelling technique reported on the present work.

A fatigue crack growth (FCG) study within the three-level FE sub modelling technique was conducted and compared against experimental results reported on the literature. A notorious overestimation of the FCG rates *da/dN* predicted by the GM was observed while the most accurate *da/dN*-values estimation was achieved by the most FE dense model, which was the F-SM. However, the three level sub models exhibited overlapped results fin the RS field for regions farther than 10 mm from the hole edge, where the effect of the cold hole expansion was minimal.

REFERENCES

[1] N. E. Dowling, *Mechanical Behavior of Materials Engineering Methods for Deformation, Fracture, and Fatigue*, 4th Edition, Pearson 2013.

[2] S. . Findlay and N. Harrison, "Why aircraft fail," *Mater. Today*, vol. 5, no. 11, pp. 18–25, 2002.

[3] Z. Semari *et al.*, "Effect of residual stresses induced by cold expansion on the crack growth in 6082 aluminum alloy," *Eng. Fract. Mech.*, vol. 99, pp. 159–168, 2013.

[4] T. N. Chakherlou and J. Vogwell, "The effect of cold expansion on improving the fatigue life of fastener holes," *Eng. Fail. Anal.*, vol. 10, no. 1, pp. 13–24, 2003.

[5] Y. Lei, B. Yan, Y. Fu, W. Chen, and L. Hou, "Research on Finite Element Model Generating Method of General Gear Based on Parametric Modelling," *IOP Conf. Ser. Mater. Sci. Eng.*, vol. 207, no. 1, pp. 37–49, 2017.

[6] E. A. Starke and J. T. Staley, *Application of modern aluminium alloys to aircraft*. Woodhead Publishing Limited, 2010.

[7] W. Yan-li, Z. You-li, H. Shuai, S. Han-xiao, and Z. Yong, "Investigation on fatigue performance of cold expansion holes of 6061-T6 aluminum alloy," *Int. J. Fatigue*, vol. 95, pp. 216–228, 2017.

[8] F. Yucan, G. Ende, S. Honghua, X. Jiuhua, and L. Renzheng, "Cold expansion technology of connection holes in aircraft structures : A review and prospect," *Chinese J. Aeronaut.*, vol. 28, no. 4, pp. 961–973, 2015.

[9] D. Sun *et al.*, "Hole-making processes and their impacts on the microstructure and fatigue response of aircraft alloys," *Int. J. Adv. Manuf. Technol.*, vol. 94, no. 5–8, pp. 1719–1726, 2018.

[10] F. Latger, T. Harris, and S. Björklund, "Drilling cost model," *SAE Tech. Pap.*, no. 724, 2002.

[11] S. Kalpakjian, S. R. Schmid, "*Manufactura, ingeniería y tecnología",* Pearson Education, 2002 .

[12] J. S. Pérez (2015), "Comportamiento a la fatiga en uniones de aluminio 6061-T6 con tratamiento térmico posterior a la soldadura (Tesis doctoral)" Instituto Politécnico Nacional,

Ciudad de México.

[13] J. Berneder, R. Prillhofer, P. Shulz and C. Melzer, “CHARACTERIZATION OF PRE-AGED AA6061-T6 SHEET MATERIAL FOR AEROSPACE APPLICATIONS,” 13th International Conference on Aluminum Alloys (ICAA13), pp. 1797–1802, 2012.

[14] T. L. Anderson, "*Fracture mechanics*", 3rd Edition, Taylor & Francis Group, LLC *Fracture Mechanics*. 2016.

[15] U. Zerbst, M. Madia, M. Vormwald, and H. T. Beier, “FATIGUE STRENGTH AND FRACTURE MECHANICS; A GENERAL PERSPECTIVE,” *Eng. Fract. Mech.*, 2017.

[16] S. Chowdhury, M. Deeb, and V. Zabel, “Effects of parameter estimation techniques and uncertainty on the selection of fatigue crack growth model,” Structures, Volume 19, 2019, Pages 128-142.

[17] P. F. P. De Matos and D. Nowell, “Analytical and numerical modelling of plasticity-induced crack closure in cold-expanded holes,” *Fatigue Fract. Eng. Mater. Struct.*, vol. 31, no. 6, pp. 488–503, 2008.

[18] Nowell, (1998), "A boundary element model of plasticity-induced fatigue crack closure". Fatigue & Fracture of Engineering Materials & Structures, 21: 857-871

[19] S. Courtin, C. Gardin, G. Bézine, and H. B. H. Hamouda, “Advantages of the J-integral approach for calculating stress intensity factors when using the commercial finite element software ABAQUS,” *Eng. Fract. Mech.*, vol. 72, no. 14, pp. 2174–2185, 2005.

[20] G. Qian, V. F. González-Albuixech, M. Niffenegger, and E. Giner, “Comparison of KIcalculation methods,” *Eng. Fract. Mech.*, vol. 156, pp. 52–67, 2016.

[21] W.Brocks and I.Scheider, “Numerical Aspects of the Path-Dependenceof the J-Integral in Incremental Plasticity How to Calculate Reliable J-Values in FE Analyses” *Int. J. Fatigue*, no. , pp. 1–33, 2001.

[22] A. Friedman, H. U. Bei, and J. J. L. Velazquez, “The evolution of stress intensity factors in the propagation of two dimensional cracks,” *Eur. J. Appl. Math.*, vol. 11, no. 5, pp. 453–471, 2000.

[23] B. Cotterell, “On brittle fracture paths,” International Journal of Fracture Mechanics, 1965, Volume 1, Number 2, Page 96.

[24] C. B and R. J.R., “Slightly curved or kinked cracks,” *Int. J. Fract.*, vol. 16, no. 2, pp. 155–169, 1980.

[25] K. W. Jones and M. L. Dunn, “Predicting corner crack fatigue propagation from cold worked holes,” *Eng. Fract. Mech.*, vol. 76, no. 13, pp. 2074–2090, 2009.

[26] S. A. Fawaz and B. Andersson, “Accurate stress intensity factor solutions for corner cracks at a hole,” *Eng. Fract. Mech.*, vol. 71, no. 9–10, pp. 1235–1254, 2004.

[27] H. D. Gopalakrishna, H. N. N. Murthy, M. Krishna, M. S. Vinod, and A. V Suresh, “Cold expansion of holes and resulting fatigue life enhancement and residual stresses in Al 2024 T3 alloy – An experimental study,” *Eng. Fail. Anal.*, vol. 17, no. 2, pp. 361–368, 2010.

[28] J. Kang, W.S. Johnson and D.A. Clark, (March 26, 2002). "Three-Dimensional Finite Element Analysis of the Cold Expansion of Fastener Holes in Two Aluminum Alloys ." ASME. J. Eng. Mater. Technol. April 2002; 124(2): 140–145 .

[29] M. Priest, C. G. Poussard, M. J. Pavier, and D. J. Smith, “An Assessment of Residual-stress Measurements Around Cold-worked Holes”, Experimental Mechanics (1995), Volume 35, Number 4, 1995.

[30] P. Papanikos and S. A. Meguid, “Elasto-plastic Finite-element analysis of the cold expansion of adjacent fastener holes,” Journal of Materials Processing Technology, Volumes 92–93, 1999, Pages 424-428,vol. 93, pp. 424–428, 1999.

[31] P. F. P. De Matos, P. M. G. P. Moreira, P. P. Camanho, and P. M. S. T. De Castro, “Numerical simulation of cold working of rivet holes,” Finite Elements in Analysis and Design, Volume 41, Issues 9–10, 2005, Pages 989-1007 vol. 41, pp. 989–1007, 2005.

[32] N. C. M. Babu, T. Jagadish, K. Ramachandra, and S. N. Sridhara, “A simplified 3-D finite element simulation of cold expansion of a circular hole to capture through thickness variation of residual stresses,” Engineering Failure Analysis, Volume 15, Issue 4, 2008, Pages 339-348 vol. 15, 2008.

[33] J. T. Maximov, G. V Duncheva, N. Ganev, and T. N. Bakalova, “The benefit from an adequate finite element simulation of the cold hole expansion process,” *Eng. Fail. Anal.*, vol. 16, no. 1, pp. 503–511, 2009.

[34] L. Yongshou, S. Xiaojun, L. Jun, and Y. Zhufeng, “Finite element method and experimental investigation on the residual stress fields and fatigue performance of cold expansion hole,”

Mater. Des., vol. 31, no. 3, pp. 1208–1215, 2010.

[35] W. Shizhen, "Effect of Cold Expansion on High Cycle Fatigue of 7A85 Aluminum Alloy Straight Lugs," *Rare Met. Mater. Eng.*, vol. 44, no. 10, pp. 2358–2362, 2015.

[36] V. D. Lacarac, A. A. Garcia-Granada, D. J. Smith, and M. J. Pavier, "Prediction of the growth rate for fatigue cracks emanating from cold expanded holes," *Int. J. Fatigue*, vol. 26, no. 6, pp. 585–595, 2004.

[37] V. Lacarac, D. J. Smith, M. J. Pavier, and M. Priest, "Fatigue crack growth from plain and cold expanded holes in aluminum alloys," *Int. J. Fatigue*, vol. 22, no. 3, pp. 189–203, 2000.

[38] S. Hole and J. G. Bakuckas, "Comparison of Boundary Correction Factor Solutions for Two Symmetric Cracks in a a straight-shank hole", Engineering Fracture Mechanics, Volume 68, Issue 9, 2001, Pages 1095-1106, vol. 68, no. April, 1999.

[39] A. R. Torabi, F. Berto, A. Campagnolo, and J. Akbardoost, "Averaged strain energy density criterion to predict ductile failure of U-notched Al 6061-T6 plates under mixed mode loading," *Theor. Appl. Fract. Mech.*, vol. 91, pp. 86–93, 2017.

[40] R. R. Ambriz, A. Ruiz, and A. Abdelwaheb, "Fatigue crack growth under a constant amplitude loading of Al-6061-T6 welds obtained by modified indirect electric arc technique," Fatigue and Technology of Welding & Joining, vol. 15, August 2010, pp. 514-521.

[41] R. R. McCullough, J. B. Jordon, P. G. Allison, T. Rushing, and L. Garcia, "Fatigue crack nucleation and small crack growth in an extruded 6061 aluminum alloy," International Journal of Fatigue, Volume 119, 2019, Pages 52-61.

[42] R. SAFDARIAN, "Stress based forming limit diagram for formability characterization of 6061 aluminum," Transactions of Nonferrous Metals Society of China, Volume 26, Issue 9, 2016, Pages 2433-2441.

[43] J. L. Cuevas, "Morfología del crecimiento de grieta por fatiga en al6061-T6 (Tesis de maestría)", Instituto Tecnológico de Pachuca, 2017.

[44] V. . Lacarac, D. Smith, and M. . Pavier, "The effect of cold expansion on fatigue crack growth from open holes at room and high temperature," *Int. J. Fatigue*, vol. 23, pp. 161–170, 2001.

[45] Owen, D. R. J., & Fawkes, A. J. (1983). Engineering fracture mechanics: Numerical methods and applications. Swansea, U.K: Pineridge Press.